

DIPLOMARBEIT

Zur Erlangung des akademischen Grades Diplom-Physikerin

Analysis of Final States with π^0 and η Mesons produced in π^-p Interactions and Studies of the Electromagnetic Calorimeters at COMPASS (CERN)



Ludwig-Maximilians-Universität München
Fakultät für Physik

vorgelegt von: **Sabine Dinter**

Eingereicht am: 29. März 2010

Erstgutachter: Prof. Dr. Martin Faessler
Zweitgutachter: Prof. Dr. Otmar Biebel

Abstract

COMPASS (Common Muon and Proton Apparatus for Structure and Spectroscopy) is a fixed target experiment at the SPS (Super Proton Synchrotron) accelerator at CERN (The European Organization for Nuclear Research), which investigates the structure and spectrum of hadrons using muon and hadron beams.

The experimental part of the diploma thesis gives an overview of the setup, the operation mode and calibration methods of the two electromagnetic calorimeters (ECALs) of COMPASS. Special emphasis is put on test measurements for the implementation of a new laser calibration system for the calorimeter ECAL2. Therefore, the first part of the thesis is focussed on tests with ECAL2 calorimeter modules by using a laser system.

The main focus of the diploma thesis is the study of diffractively and centrally produced resonances. The reactions $\pi^-p \rightarrow \pi^-\pi^0p$, $\pi^-p \rightarrow \pi^-\eta p$, $\pi^-p \rightarrow \pi^-\pi^0\pi^0p$ and $\pi^-p \rightarrow \pi^-\eta\eta p$ with an incoming pion beam at 190 GeV are studied. The analysis is performed on 2008 data with a preliminary calibration of the electromagnetic calorimeters. An additional kinematic fitting routine and corrections of the cluster energy were implemented to improve the quality of the selected data.

The COMPASS data provides a proof for various known diffractively produced states, i.e. $\rho(770)$, $a_0(980)$, $a_2(1320)$, $\pi_2(1670)$ and $\rho_2(1700)$. A first evidence for the known $f_0(1500)$ is seen in the $\pi^-p \rightarrow \pi^-\eta\eta p$ channel at 1.5 GeV. This analysis confirms that COMPASS is able to study final states with neutral mesons. Additionally, the thesis presents an elementary analysis of the reaction $\pi^-p \rightarrow \pi^-\eta'p$.

Beyond that, the selected π^0 s are used for performance checks of the electromagnetic calorimeters on a run-by-run basis (and different module types).

Für meine Eltern.

Contents

1	Introduction	1
2	Theoretical Motivation	3
2.1	The World of Mesons	3
2.1.1	The Standard Model	3
2.1.2	Yukawa's Idea	5
2.1.3	Characteristics of Mesons	6
2.1.4	Resonances	8
2.1.5	Exotic States	8
2.2	Results from Previous Experiments for $\pi^- p \rightarrow \pi^- \eta' p$	9
2.3	Diffractional Dissociation and Central Production	10
2.3.1	Diffractional Dissociation of Mesons	10
2.3.2	Central Production of Mesons	11
3	The COMPASS Experiment	13
3.1	Physics Objectives	13
3.2	The M2 Beam Line	14
3.3	Experimental Setup	15
3.3.1	Design Overview	15
3.3.2	Target Region	15
3.3.3	Tracking Detectors	16
3.3.4	Detectors for Particle Identification	17
3.3.5	Trigger	19
4	The Electromagnetic Calorimeters at COMPASS	21
4.1	General Remarks on the Operating Mode of Electromagnetic Calorimeters	21
4.1.1	Interaction of Photons and Electrons with Matter	21
4.1.2	Radiation Length	22
4.1.3	Electromagnetic Shower	23
4.2	Detection of Photons in Lead Glass	24
4.3	Setup of the Electromagnetic Calorimeters at COMPASS	27
4.4	ECAL1 and ECAL2 Modules	28
4.5	Operation Mode of a Photomultiplier	31
4.6	Calibration Methods	32
5	The Laser Monitoring System for ECAL	35
5.1	Experimental Setup for ECAL1	36
5.2	Test Measurements for a new ECAL2 Monitoring System	38
5.2.1	Photomultiplier Test with LED	38
5.2.2	GAMS Modules	40
5.2.3	SHASHLIK Modules	44

5.2.4	Conclusion and Outlook	49
6	Data Reconstruction and Analysis at COMPASS	51
6.1	The COMPASS Data Reconstruction Programme CORAL	51
6.2	The Physics Analysis Software Tool PHAST	51
6.3	The Data Analysis Framework ROOT	51
7	Analysis of Final States with Neutral Mesons	53
7.1	Event Selection	53
7.2	Data Statistics and Invariant Mass Spectra	66
7.2.1	$\pi^- p \rightarrow \pi^- \gamma \gamma p$	66
7.2.2	$\pi^- p \rightarrow \pi^- \gamma \gamma \gamma p$	68
7.2.3	$\pi^- p \rightarrow \pi^- \pi^+ \pi^- \gamma \gamma p$	73
7.3	Summary of the Mesons seen in $\pi^- p \rightarrow \pi^- 2\gamma p$, $\pi^- p \rightarrow \pi^- 4\gamma p$ and $\pi^- p \rightarrow \pi^- \pi^+ \pi^- 2\gamma p$	77
8	Performance Checks of the Electromagnetic Calorimeters	79
9	Summary and Conclusion	83
A	ECAL2 Counters Map Type (Run 2008)	i
B	Data Sheet of the Minilite Laser I and II	iii
C	Data Sheets of the Integrating Spheres	v
D	ECAL1 High Voltages for GAMS Modules (2009 run)	vii
	References	ix
	List of Figures	xvi
	List of Tables	xvii
	Acknowledgement	xix

1 Introduction

*"Ein Experiment ist eine List, mit der man die Natur dazu bringt, verständlich zu reden. Danach muss man nur noch zuhören."*¹ (George Wald)²

One of the major questions is what matter is made of and what holding it together. In order to get an answer to this question everything has to start with an idea which flows into a theoretical prediction and results in an experimental verification. If the experiment confirms the theory we obtain new insights into the nature. Particle accelerators provide the necessary instrument for the implementation of such experiments. The experimental and theoretical advances in particle physics over the past century give us a remarkable insight into the structure of matter.

One of these very successful experiments is the fixed target experiment COMPASS (Common Muon and Proton Apparatus for Structure and Spectroscopy) at CERN³ in Geneva, Switzerland at the SPS (Super Proton Synchrotron), the pre-accelerator of the LHC (Large Hadron Collider). The COMPASS collaboration, consisting of more than 240 physicists from 26 institutions from all over the world has the aim to study hadron structure with polarized muon beams and hadron spectroscopy with hadron beams.

The focus of the diploma thesis is devoted to the hadron programme of COMPASS. The purpose to study hadron spectroscopy is the search for glueballs in the high mass region in exclusive diffractive pion proton scattering, the study of leptonic and semileptonic decays of charmed hadrons and the investigation of Primakoff scattering. In the years 2008 and 2009 the COMPASS experiment was focussed on hadron data taking.

The main concern of this diploma thesis is the analysis of final states with neutral mesons. On the one hand, the results are used to show that COMPASS is able to study final states with neutral mesons and on the other hand to establish a basis for further studies, like the search for exotics. Moreover the analysis gives the possibility to check the performance of the electromagnetic calorimeters of COMPASS. Perfectly calibrated calorimeters are indispensable for the reconstruction and analysis of data in high energy physics.

In addition to the performance studies with this analysis, test measurements with the hardware elements of the electromagnetic calorimeters were done, to provide a basis for a new laser monitoring system for the calorimeters.

¹"An experiment is an artifice with which it brings the nature to speak intelligibly. After that you need to listen only."

²American biochemist, who received the Nobel Prize in Physiology or Medicine (1967) together with Haldan Keffer Hartline and Ragnar Granit.

³Conseil Européen pour la Recherche Nucléaire (The European Organization for Nuclear Research)

This thesis starts with a review of the basic concepts of particle physics including meson spectroscopy and gives an overview of the experimental setup and measurements of COMPASS. In particular, the setting up, operation and calibration methods of the two electromagnetic calorimeters (ECALs) of COMPASS are addressed. Special emphasis is put on test measurements for a new laser monitoring system for ECAL2.

Furthermore the reactions $\pi^- p \rightarrow \pi^- \pi^0 p$, $\pi^- p \rightarrow \pi^- \eta p$, $\pi^- p \rightarrow \pi^- \pi^0 \pi^0 p$ and $\pi^- p \rightarrow \pi^- \eta \eta p$ with an incoming pion beam at 190 GeV are studied. The analysis is performed on 2008 data. Additional kinematic fitting routines and corrections of the cluster energy were implemented to improve the quality of the selected data. The COMPASS data provides a proof for various diffractively produced (well known) states, i.e. $\rho(770)$, $a_0(980)$, $a_2(1320)$, $\pi_2(1670)$ and $\rho_2(1700)$. A first evidence for the known $f_0(1500)$ is seen in $\pi^- p \rightarrow \pi^- \eta \eta p$ at an energy of 1.5 GeV.

Additionally, the present work presents an elementary analysis of the reaction $\pi^- p \rightarrow \pi^- \eta' p$. This analysis shows first hints for the existence of the exotic state $\pi_1(1600)$ in the $\pi^- \eta'$ final state.

The selected π^0 s are used for performance checks of the electromagnetic calorimeters on a run-by-run basis and different module types.

2 Theoretical Motivation

2.1 The World of Mesons

2.1.1 The Standard Model

Modern particle physics actually began with the discovery of mesons. According to our present understanding of particle physics mesons are subatomic particles composed of one quark and one antiquark, belonging to the hadron particle family. Hadrons are a group of particles build of quarks. Baryons consist of three quarks and form the second part of the hadron family. The Standard Model gives us the possibility to classify these quarks and to understand how they interact. It provides a general theory which is well consistent with the experimental results of particle physics. The main statement of this theory is that the known matter is made of twelve fundamental particles, kept together by four fundamental forces. The particles can be classified in two different typs: quarks and leptons (see figure 1).

Three Generations of Matter (Fermions)				
	I	II	III	
mass→	3 MeV	1.24 GeV	172.5 GeV	0
charge→	$\frac{2}{3}$	$\frac{2}{3}$	$\frac{2}{3}$	0
spin→	$\frac{1}{2}$	$\frac{1}{2}$	$\frac{1}{2}$	1
name→	u up	c charm	t top	γ photon
Quarks	6 MeV $-\frac{1}{3}$ $\frac{1}{2}$ d down	95 MeV $-\frac{1}{3}$ $\frac{1}{2}$ s strange	4.2 GeV $-\frac{1}{3}$ $\frac{1}{2}$ b bottom	0 0 1 g gluon
	<2 eV 0 $\frac{1}{2}$ ν_e electron neutrino	<0.19 MeV 0 $\frac{1}{2}$ ν_μ muon neutrino	<18.2 MeV 0 $\frac{1}{2}$ ν_τ tau neutrino	90.2 GeV 0 1 Z weak force
	0.511 MeV -1 $\frac{1}{2}$ e electron	106 MeV -1 $\frac{1}{2}$ μ muon	1.78 GeV -1 $\frac{1}{2}$ τ tau	80.4 GeV ± 1 1 W weak force
Leptons				Bosons (Forces)

Figure 1: The Standard Model of elementary particles including the gauge bosons in the right column [2].

The six quarks are matched in three generations: the "up quark" and the "down quark" in the first generation, followed by the "charm quark" and "strange quark" in the second generation and finally the "top quark" and "bottom quark" in the third generation. The six leptons are also set up in three generations: the "electron" and the "electron-neutrino" in the first generation, the "muon" and the "muon-neutrino" in the second and the "tau" and "tau-neutrino" in the third generation. The first generation consists of the lightest and most stable particles. The heavier and less stable particles belong to the second and third generation. Therefore all stable matter is made of particles from the first generation.

Three of the known forces are described by the Standard Model: the electromagnetic, strong and weak force. The gravitational force is not yet included. In the Standard Model the electromagnetic interaction as well as the weak and strong interaction are described by gauge theories. The force of a particle to another is mediated by particles, so called "gauge bosons". Every force has its carrier particle: the electromagnetic force is carried by photons, the strong force by gluons and the weak force is mediated by W^\pm and Z^0 bosons. The graviton could be the responsible carrier particle for the gravitational force, but it is not yet found. Figure 1 summarizes the contents of the Standard Model and the four forces.

An essential component of the Standard Model, which was not yet seen in an experiment, is the so called Higgs boson. With higher energies at the Large Hadron Collider physicists hope to find it soon.

The last 3 sections are based on the CERN article: [1].

The quarks have, besides the usual particle properties (charge, spin, isospin, etc.) a color charge (red, green and blue). This charge is responsible for strong interactions between quarks. Gluons themselves have color charges and can interact with each other. Quarks and gluons are not observed as free particles. As soon as a quark-antiquark pair is produced they bind together as colour neutral mesons or baryons. Quarks carry three types of colour charge; antiquarks carry three types of anticolour. The neutral colour is guaranteed by the formation of colour anticolour pairs (mesons) or by the creation of three colour states (baryons). These properties are described by the theory of Quantum Chromo Dynamics (QCD).

2.1.2 Yukawa's Idea

Historically, the discovery and classification of mesons started with the work of Yukawa. The explanations of the upcoming sections (2.1.2 - 2.1.5) are based on [3] and [4].

Hideki Yukawa, a Japanese physicist, published a theory in 1935, which gave a prediction of the existence of mesons. This theory explained the interaction between neutrons and protons. In 1949 he received the Nobel Prize for Physics on the theory of elementary particles. His results had a big impact on our understanding of the structural principle of particles.

Yukawa postulated a new particle (later termed the meson), the so called pion π , which must be exchanged between two nucleons in a "nuclear interaction". His idea based on the analogy in which a particle of light may be exchanged between two charged particles in the "electromagnetic interaction". The pion was predicted to be the "carrier particle" of the strong force which supply the "glue" for all particles making up the nucleus of the atom.

From the scattering experiments with α -particles Yukawa knew that the strong force must be in the range of 10^{-15} m. Therefore he expected a pion mass at approximately 150 MeV (300 times bigger than the mass of an electron).

To cover all possible interactions of nucleons a pion must exist in three charge variations. A proton for example can become a neutron by radiating a positive pion π^+ or absorbing a negative pion π^- . Due to the fact that a proton may also remain unchanged in a nuclear process a neutral pion π^0 must exist.

The charged pions: π^+ and π^- , were discovered by the collaboration of Cecil Powell, Cesar Lattes and Giuseppe Occialini at the University of Bristol in 1947. It appeared that the mass of the charged pion is about 273 times bigger than the mass of an electron ($m_{\pi^+, \pi^-} = 140$ MeV). They rapidly decay into a muon which decays into an electron by emitting an electron-neutrino and a muon-antineutrino, latter ensures the energy and momentum conservation. The following two figures show the π^+, π^- and π^0 decay:

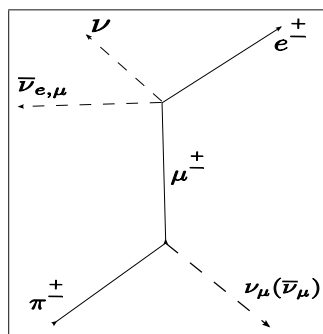


Figure 2: π^+, π^- decay [3].

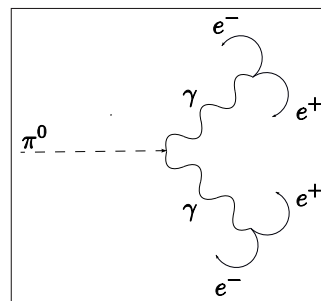


Figure 3: π^0 decay and pair production [3].

2.1.3 Characteristics of Mesons

In general mesons are classified by the following properties: Charge Q , Total Angular Momentum J , Spin S , Isospin I , the third component of the Isospin I_3 , Parity ($P = (-1)^{L+1}$), Strangeness S , Charmness C , Bottomness and Topness T . In particle physics we distinguish between C- and G-Parity. C-Parity is only defined for mesons that are their own antiparticle. G-Parity is a generalization of the C-parity.

Mesons are bound states of a quark (q) and an antiquark (\bar{q}) as described above. These states can be classified using the following parameters: total spin of both quarks and orbital angular momentum. Each of the two quarks has a spin of $s = \frac{1}{2}$ so overall the system can have a total spin of $S = 0$ or $S = 1$. The total spin and orbital angular momentum L define the total angular momentum J of the $q\bar{q}$ system. In addition to that one could get radial excitations supplement the ground state. Using the preceding characteristics, mesons are classified in the following way:

Type	J	P	S	L
Pseudoscalar Meson	0	-	0	0
Pseudovector Meson	1	+	0	1
Vector Meson	1	-	1	0
Scalar Meson	0	+	1	1

Table 1: Types of mesons and quantum numbers for the lowest lying states.

Flavourless mesons consist of a quark and an antiquark (same flavour), flavoured mesons are made of quarks and antiquarks of different flavours.

Pseudoscalar Mesons

Well known mesons with the classification $L=0$, $J=0$, $P=-1$ and radial quantum number $n=1$ are called pseudoscalar mesons. Figure 4 gives an overview of the existing pseudoscalar mesons with spin $S=0$.

The members of different nonets differ in the spin orientation of the constituent quarks and their relative orbital angular momentum. The members of the same group differ in their isospin and strangeness. The nonet is classified by their meson-spin, P- and C-parity. [20]

Each of these particles are build of a q and an \bar{q} or a combination of a $q\bar{q}$ system. The π^0 for example is made of an $u\bar{u}$ and a $d\bar{d}$ system. In total, 25 possible combinations can be formed from the 5 quark flavours.

Lightest mesons weakly decay into lepton pairs (like an electron positron pair or a muon anti-muon pair: π^+ and π^- decay already shown above) and electromagnetically decay into two photons ($\pi^0 \rightarrow \gamma\gamma$: most likely decay). They decay into hadrons by virtue of the strong interaction, if their mass is high enough.

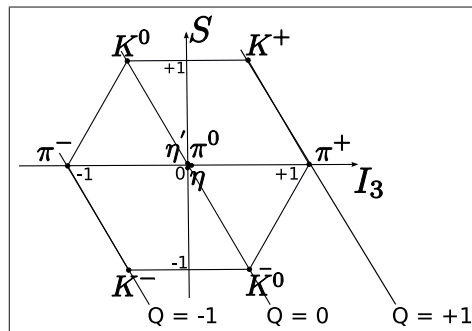


Figure 4: Meson nonet: Pseudoscalar mesons with spin $S=0$.

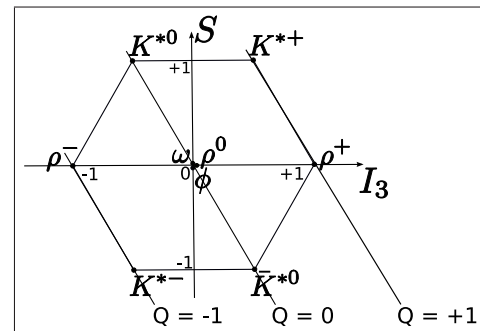


Figure 5: Meson nonet: Vector mesons with spin $S=1$.

The three pions π^+ , π^- , π^0 form a meson family with approximately the same mass. Experiments have shown that the spin of the pion is $S = 0$. [4]

A summary of the quark contents, the most likely decays and important properties of the pseudoscalar mesons, which are relevant for this diploma thesis (π^+ , π^- , π^0 , η and η') are shown in the following table:

	Quark content	Q	M [MeV]	Lifetime [s]	S	C	Decays
π^+	$u\bar{d}$	1	139.57	$2.6 \cdot 10^{-8}$	0	0	$\mu^+ \nu_\mu (>> 99\%)$
π^0	$(u\bar{u} - d\bar{d})/\sqrt{2}$	0	134.96	$0.8 \cdot 10^{-16}$	0	0	$\gamma\gamma (> 99\%)$
π^-	$d\bar{u}$	-1	139.57	$2.6 \cdot 10^{-8}$	0	0	$\mu^- \bar{\nu}_\mu (> 99\%)$
$\eta \approx$	$u\bar{u} + d\bar{d} - 2s\bar{s}/\sqrt{6} (= \eta_8)$	0	547.853	$2.5 \cdot 10^{-19}$	0	0	$\gamma\gamma (> 39\%)$
$\eta' \approx$	$d\bar{u} + d\bar{d} + s\bar{s}/\sqrt{3} (= \eta_1)$	0	957.66	$2.4 \cdot 10^{-21}$	0	0	$\pi^+ \pi^- \eta (> 44\%)$

Table 2: Pseudoscalar mesons from u/d- and s-quarks and their properties [4].

Vector Mesons

Mesons which have a spin $S=1$ (parallel quark spin) and the classification $L=0$, $J=1$, $P=-1$ are called vector mesons. A collection of vector mesons is shown in figure 5. They have a higher mass than the pseudoscalar mesons (in the lowest lying state). Vector mesons dominantly decay due to the electromagnetic interaction or strong interaction, with a short average lifetime.

2.1.4 Resonances

Particles with a long lifetime can easily be seen by track detectors or bubble chambers. Particles having a very short lifetime decay rapidly into different particles. It is not possible to detect them directly but to reconstruct them from their decay products. These decaying particles are called "resonances". Resonances can be produced in two different types of experiments:

- In a "resonance formation" two particles collide and generate a resonance as an intermediate state of the incoming and outgoing particle.
- At a "resonance production" we infer the presence of a resonance when the invariant energy of the two or more outgoing particles has a favoured value. It is difficult to find resonances in this manner because one needs to examine all combinations of outgoing particles and assign their energies (invariant masses) to see if there is an enhancement.

High-energy experiments allow to generate new particles and one can check whether they originate from resonances yet unknown. The mass of an absolutely stable particle is well defined. A less stable particle always has a blurred value of mass which can be explained by the uncertainty principle:

$$\Delta E \Delta t \geq \hbar. \quad (1)$$

2.1.5 Exotic States

Exotic states are strongly interacting systems (e.g. gg , ggg , $q\bar{q}g$). Mixture states of gluons and valence quarks are called Hybrids. These states are predicted theoretically but have to be confirmed experimentally. As they are combined by gluons and quarks, they can embrace quantum numbers, which are forbidden for conventional hadrons ($q\bar{q}$, qqq).

States, which only consist of gluons are called glueballs. They are expected to be flavour blind and decay into states including large glue components or large $SU(3)$ singlet components like the η or the η' . Famous candidates for exotics have been seen in $\pi\eta$ and $\pi\eta'$ final states, with the forbidden quantum number $J^{PC} = 1^{-+}$ [11]. The experimental key to the investigation of such states provides the diffractive dissociation and central production of mesons, which will be described in section 2.3.

2.2 Results from Previous Experiments for $\pi^-p \rightarrow \pi^- \eta' p$

The search for exotics makes the final state $\pi^-p \rightarrow \pi^- \eta' p$ very interesting. The analysis of this channel contribute to discussions about the existence of an exotic resonance at 1600 MeV ($\pi_1(1600)$).

The Brookhaven National Laboratory experiment E852 at the AGS (Alternating Gradient Synchrotron) studied the final state $\pi^-p \rightarrow \pi^- \eta' p$ at an energy of $18 \frac{GeV}{c}$ with a sample of ~ 6000 events. Fig. 6 on the left (a.) shows the $\pi^+\pi^-\eta$ effective mass distribution, seen by the E852 collaboration in 2001. The inset shows the $\gamma\gamma$ effective mass distribution in $0.01 \frac{GeV}{c^2}$ bins. On the right side (b.) (in fig. 6) you can see the $\pi^- \eta'$ effective mass distribution. The smooth curve in (b.) shows the true mass acceptance. The shown results and descriptions are taken from [5].

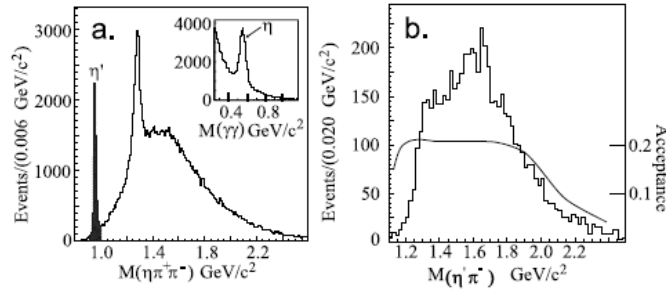


Figure 6: (a.): The $\pi^+\pi^-\eta$ effective mass distribution. (b.): $\pi_1(1600) \rightarrow \pi^- \eta'$ seen by E852 (2001) in $\pi^-p \rightarrow \pi^- \eta' p$ at 1600 MeV [5].

The plots show an $a_2(1320)$ peak and a broad enhancement at $1600 \frac{GeV}{c^2}$. The results of the analysis of this channel have confirmed the existence of an exotic $J^{PC} = 1^{-+}$ resonance at $1600 \frac{GeV}{c^2}$. [5] The $a_2(1320)$ and $\pi_1(1600)$ were also seen by the VES experiment in $\pi^-N \rightarrow \pi^- \eta' N$ at $37 \frac{GeV}{c}$ (see the following fig. 7) in 1993. For a more detailed description I refer to [6].

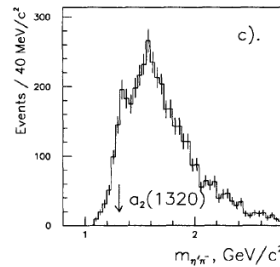


Figure 7: $a_2(1320)$, $\pi_1(1600)$ seen in $\pi^-N \rightarrow \pi^- \eta' N$ at $37 \frac{GeV}{c}$ by VES [6].

2.3 Diffractive Dissociation and Central Production

Diffractive scattering and central production are studied in parallel at Compass using pion, proton and kaon projectiles and can be used for the production of exotic particles. The decay products of the resonances can be analyzed with the help of the spectrometer.

2.3.1 Diffractive Dissociation of Mesons

In a diffractive scattering process a direct excitation of the beam particle occurs by the exchange of a reggeon to a resonance. Figure 8 shows the single diffractive excitation. At the excitation a momentum t is transferred to the target proton. Mesons are mainly produced in diffractive processes. The meson production from pion dissociation is a method to produce hadrons with the same internal quantum numbers as a pion. Hybrids can also be produced, like the pseudovector mesons with the exotic quantum number $J^{PC} = 1^{-+}$. Three of these resonances were observed by the VES and E852 experiment: $\pi_1(1400)$, $\pi_1(1600)$ and $\pi_1(2000)$.

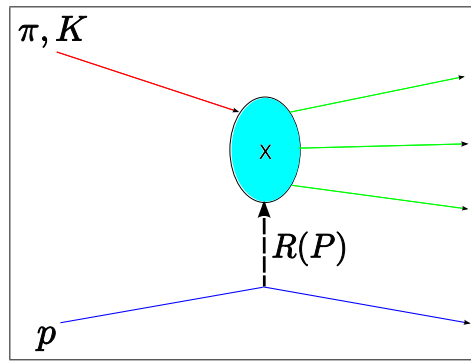


Figure 8: Single diffractive excitation.

The interaction is assumed to proceed via an effective reggeon exchange. At elastic vertices, a particular reggeon plays a dominant role, the so called pomeron (P). The real nature of the pomeron is not yet known but experiments and theoretical predictions have shown that it should be a gluonic object as only momentum and angular momentum is exchanged [21].

The squared four-momentum transfer t of a diffractive reaction can be assigned by measuring the momenta of the involved particles:

$$t = q^2 = (p_\pi - p_X)^2 = (E_\pi - E_X)^2 - (\vec{p}_\pi - \vec{p}_X)^2 \quad (2)$$

The four-momentum-vectors of the incoming particle (π) and the produced particle or resonance (X), are described by $p_{\pi,X}$. The energy of π and X are defined by $E_{\pi,X}$. $\vec{p}_{\pi,X}$ stands for the

three-momentum-vectors of the incoming particle and the produced particle or resonance. The recoiling nucleus remains intact, while the incoming particle is excited. [11]

The resonance or particle X which is produced in this reaction, subsequently decays into lighter particles and can be reconstructed from its decay products.

2.3.2 Central Production of Mesons

A particular mechanism of the central production is shown in fig. 9. There is no excitation of the beam particle in central production processes. Instead of that, it is a direct production of a neutral resonance, while two reggeons interact and form a neutral resonance (X). This resonance decays into lighter particles (pions and kaons). The target proton remains intact and can be detected as a recoil proton (like in diffractive scattering processes). In the central production process, in figure 9 two reggeons are exchanged but it must not necessarily be a double-pomeron exchange. The main interest lies in the double-pomeron process.

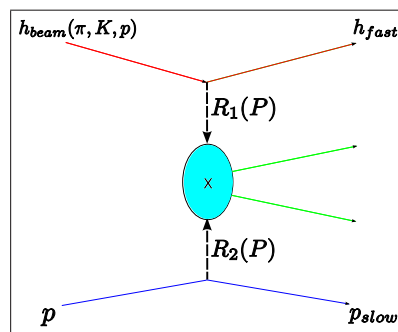


Figure 9: Central production mechanism.

3 The COMPASS Experiment

3.1 Physics Objectives

One of the main goals of the COMPASS experiment (located at SPS at CERN: see figure 10) is the study of meson spectroscopy in the gluon-rich proton-proton central production and in diffractive pion and kaon scattering. COMPASS incorporates a large and small angle spectrometer (30 mrad to 180 mrad), which enable the investigation of various physics topics.

The good momentum resolution is the advantage of such a two stage spectrometer technique. The aim of the muon programme is to study structure functions, helicity distributions of quarks, measurements on gluon polarisations and transverse quark distributions. One main goal of the hadron programme is the identification of glueballs and hybrid states.



Figure 10: Location of the COMPASS experiment at CERN.

The COMPASS spectrometer was assembled in 1999-2000 and commissioned during a technical run in 2001 [8]. The first data taking period started in summer 2002 and ended in fall 2004. The experiment had its first shut-down in 2005 for repairs, re-fittings and new installations. The years 2006 and 2007 were dedicated to the muon run, 2008 and 2009 to the hadron programme. In 2010 a polarised proton will be used again to study structure functions [8].

3.2 The M2 Beam Line

Protons, at an energy of about 400 GeV are extracted from the SPS accelerator. The duration of a spill is 5.1 s and $\sim 10^{13}$ protons are extracted per SPS cycle (the SPS cycle lasts 16.8 s). When striking on the target (T6) pions and kaons are produced which are later selected by their momenta. These particles pass through a 700 m long stretch where 6% of them decay into muons and muon-neutrinos:



The beam is threaded through deflection magnets (red marked triangles in figure 11) over the M2 extraction line (see figure 11), then the beam reaches the COMPASS target.

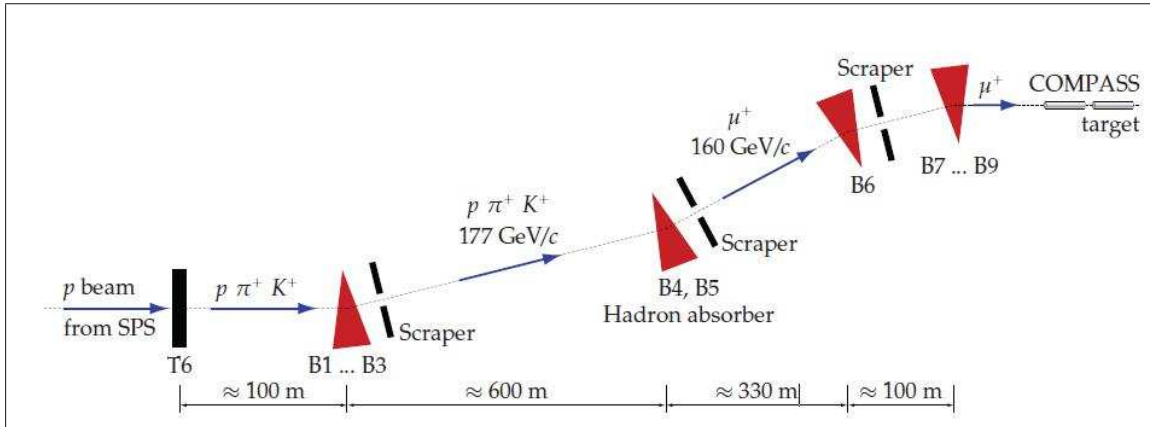


Figure 11: The M2 Beam Line for the Muon Programme [14].

The SPS beam line M2 can be used to get high-intensity positive muon beams up to $200 \frac{GeV}{c}$ or high-intensity hadron beams up to $300 \frac{GeV}{c}$. The hadron beams mainly consist of protons or negative and positive pions.

The provision of negative muon beams with low energies is feasible. It is possible to provide also an electron beam for the requirements of a calibration of the electromagnetic calorimeters or test measurements. The change of the beam is done with the help of a fast-responding computer system.

3.3 Experimental Setup

3.3.1 Design Overview

Figure 12 shows the experimental setup of the COMPASS experiment in 2008. The following section provides an overview of the technical components of the spectrometer and explains their working principle.

The successive description of the spectrometer components and their working principles are mainly based on [17].

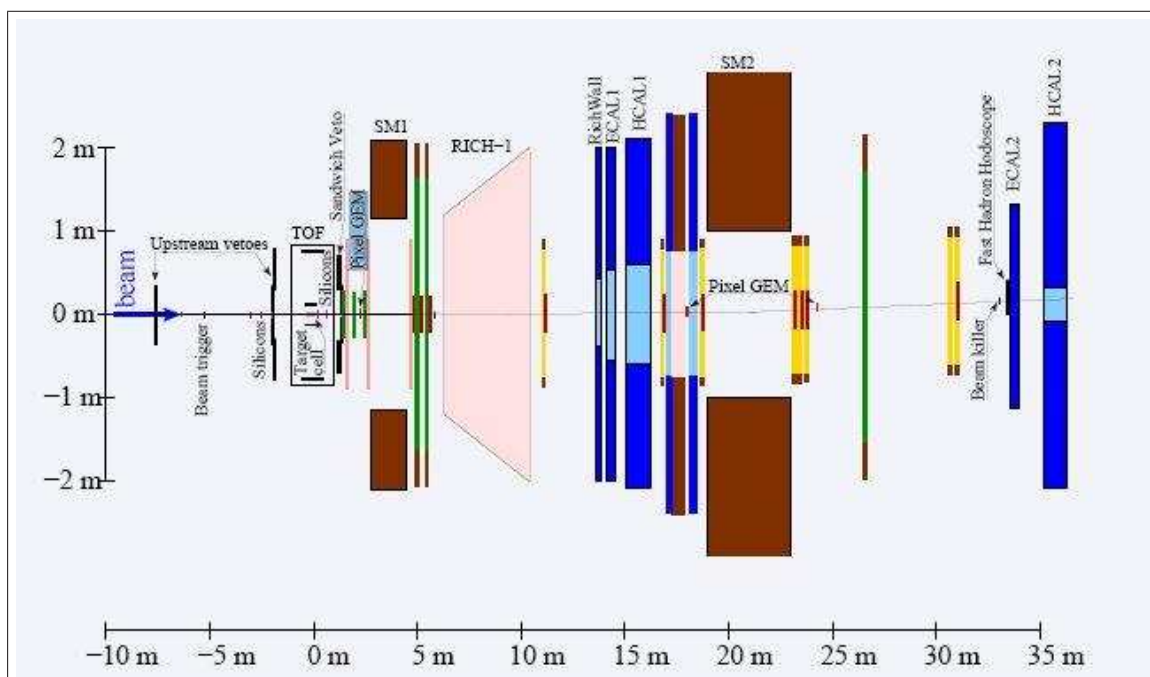


Figure 12: The COMPASS Layout [19].

3.3.2 Target Region

For the different requirements of specific experiments, the COMPASS target has to fulfill different conditions. For a highly longitudinal polarized muon beam with energies from 90 to 200 GeV, a muon intensity of $2 \cdot 10^8$ muons per spill is required. The momentum of each incoming muon is measured with "beam momentum stations" (BMS) (only used in the muon programme). The hadron beam consists of different particles: The beam, which was used for this thesis consists of pions with some kaons and antiproton contaminations (= negative hadron beam). Fast Cherenkov counters (= system of CEDAR's, see figure 13) are used to identify the particles in such a mixed beam.

Depending on the individual experimental requirements a liquid hydrogen or lead target can be used. The target is surrounded by a "recoil proton detector" (RPD), shown in figure 14, which comprises two rings that are made of scintillating material. Two stations of silicon microstrip detectors in front of and behind the target, with a high spatial resolution and a good resistance against high fluxes, are used to measure the angle between the incoming and outgoing beam.



Figure 13: CEDAR's for pion and kaon tagging.



Figure 14: Front view of the RPD detector.

3.3.3 Tracking Detectors

Tracking detectors measure the three-dimensional positions of charged particles as they travel through it, usually in a magnetic field, accordingly to allow measurement of their momentum [7]. The tracking system at COMPASS is used to correlate the expected particle flux in the different positions along the whole spectrometer.

Along the beam and very close to the target the used detectors must unify two important factors. A high particle rate capability (up to a few MHz per channel) is needed as well as a very good space resolution (100 μm and better) [17]. The beam path itself is surrounded only by some material to diminish secondary interactions with beam particles and to minimize "multiple scattering effects" ([17]). Many tracking stations are arranged alongside the spectrometer. Each station consists of a set of detectors of the same type at approximately the same z-coordinate along the beam. According to their different requirements these stations are installed at various locations of the spectrometer:

VSAT (Very Small Area Tracking)

With the help of the BMS it is possible to determine the momentum of the incoming particles on an event-by-event basis. At a radial distance of 2.5-3 cm, the beam region is covered by eight scintillating fiber hodoscopes (SciFi's) which ensure the tracking of incoming and scattered beam particles as well as the detection of all other reaction products arising near the beam. The COMPASS silicon microstrip detectors are situated upstream of the target and used to detect incoming muons in the muon programme and for track and vertex reconstructions of hadron

particles. The beam divergence is taken into account by using various sizes of these microstrip detectors.

SAT (Small Area Tracking)

For distances larger than 3 cm from the beam, 12 Micromegas detectors (Micromesh Gaseous Structure), assembled in 3 stations and 11 GEMs (**G**as **E**lectron **M**ultipliers) cover the region from the downstream side of the SM1 magnet (see fig. 15) to the end of the spectrometer. The detector has a two parallel electrode structure and a set of microstrips for readout at the bottom. When a particle passes through the conversion area it comes to an ionisation. The produced primary electrons drift into a moderate field. An avalanche is then produced in the amplification gap. The resulting electron/ion pairs can now be detected by the strips. The mesh is used to separate the two gaps and to avoid the reflux of produced ions to the conversion gap. GEM detectors are build of 3 copper plated foils instead of one mash. These detectors ensure a high space resolution ($< 100 \mu\text{m}$) with a low radiation length in the small area region.

LAT (Large Area Tracking)

The large angle tracking system consists of planar drift and straw tube chambers. These are gas detectors with anode wires of different types. The MWPC's (Multiwire Proportional Counters) are installed along the entire spectrometer. These counters are able to amplify single photoelectrons and detect them.

3.3.4 Detectors for Particle Identification

A variety of detectors are used for particle identification at COMPASS. The different detectors are installed in the Large and Small Angle Spectrometers (LAS and SAS). An artistic overview of these elements are shown in fig. 15. The next section presents these detectors and gives a short overview of their working principle, based on CERN-PH-EP [17]. For more details I also refer to CERN-PH-EP [17].

RICH: The RICH Detector, located in the first spectrometer (RICH-1), is needed for hadron identification. It separates hadrons into kaons, pions and protons, according to their momenta. The RICH-1 is a large-size Cherenkov Counter and works in the domain of $5 \frac{\text{GeV}}{c}$ to $80 \frac{\text{GeV}}{c}$. Therefore, it covers the whole angular acceptance of COMPASS LAS. The working principle is based on the emission of Cherenkov photons in C_4F_{10} radiator gas and their subsequent reflection by two spherical mirrors. These photons are dissipated to electrons by the CsI photocathodes of 8 MWPCs and finally detected by the latter.

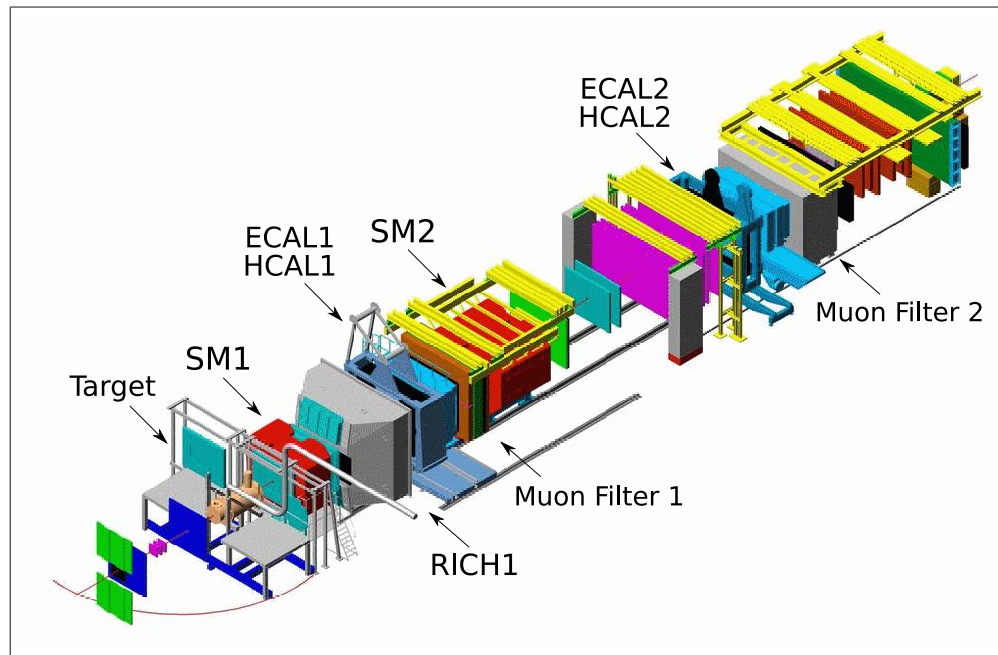


Figure 15: Artistic view of the 60 m long COMPASS two-stage spectrometer [19].

Hadron Calorimeters: The two Hadron Calorimeters HCAL1/2 are able to detect neutrons from their decays of charmed baryons. They measure the energy of hadrons and provide an aligned trigger signal.

Electromagnetic Calorimeters: An electromagnetic calorimeter is a detector which determines the energy of electrons, positrons and photons. The COMPASS spectrometer contains two electromagnetic calorimeters ECAL1 and ECAL2. ECAL1 is directly installed in front of HCAL1, ECAL2 in front of HCAL2. Hadrons only lose a small amount of their energy due to electromagnetic interactions. Therefore, hadrons are likely to be detected in the proximate HCALs. Electromagnetic Calorimeters with good performances are needed for the COMPASS hadron program and for the studies of GPDs. The ECALs will be discussed in detail in the next chapter.

Muon Walls: The Muon Walls consist of muon filters, which are able to detect muons from semileptonic decays. The two Muon Walls (MW1, MW2) are made of medium resolution tracking detectors joint with hadron absorbers [17]. They are situated at the end of each spectrometer stage.

3.3.5 Trigger

In general the responsibility of a trigger is to preselect events in an experiment and to induce the readout of the detectors. An ideal trigger system only selects events from reactions we are interested in, but in reality we receive data from different reactions as well. The trigger signal is initiated when the threshold of the detectors is exceeded and logical conditions are satisfied. This causes the readout of all detectors at a certain time, dependent on the latency due to the time of flight of the particles (= event) [11].

The trigger system gets its information from scintillating hodoscope detectors, calorimeters and veto systems. The particle tracks and the scattered particle itself are verified by scintillating hodoscopes. The energy deposition of particles can be determined with the help of the calorimeters and the veto detectors are used for suppression of events coming from halo particles. [15]

4 The Electromagnetic Calorimeters at COMPASS

4.1 General Remarks on the Operating Mode of Electromagnetic Calorimeters

4.1.1 Interaction of Photons and Electrons with Matter

Charged particles lose their energy in matter primarily by atomic excitations and ionizations. The mean rate of energy loss is given by the Bethe-Bloch equation [18]

$$-\frac{dE}{dx} = Kz^2 \frac{Z}{A} \frac{1}{\beta^2} \left[\frac{1}{2} \ln \frac{2m_e c^2 \beta^2 \gamma^2 T_{\max}}{I^2} - \beta^2 - \frac{\delta}{2} \right], \quad (4)$$

where E (MeV) is the energy of the incident particle, $\frac{K}{A} = 4\pi N_A r_e^2 m_e c^2 \cdot \frac{1}{A}$ with Avogadro's number $N_A (6.022 \cdot 10^{23} \text{ mol}^{-1})$, Z is the atomic number of the absorber, the particle passes, z indicates the number of charge of the incident particle, $m_e c^2$ is the electron mass $\times c^2$, T_{\max} (MeV) gives the maximum kinetic energy, I (eV) is the mean excitation energy and δ the density effect correction to ionization energy loss factor. With K defined previously and A given in $\frac{\text{g}}{\text{mol}}$: dE is measured in MeV and dx in $\frac{\text{g}}{\text{cm}^2}$.

The Bethe-Bloch equation gives the energy loss in $\frac{\text{g}}{\text{cm}^2}$, fast charged particles (protons, α -particles and atomic ions) suffer, by travelling through matter. For electrons (and positrons), the energy loss is slightly different because of their low mass and indistinguishability. Ionisation and bremsstrahlung processes are the dominant interactions of electrons with matter.

Bremsstrahlung, "deceleration radiation", is the electromagnetic radiation which occurs by the acceleration of a charged particle, when it is deflected by another charged particle like an atomic nucleus. Ionization means the dislodge from one or more electrons from an atom. As shown in figure 16, for electrons the energy loss by ionization in lead is dominant up to 10 MeV. For higher energies bremsstrahlung is the dominant process. The energy loss due to bremsstrahlung grows proportionally to the electron energy, while the loss by ionization proceeds logarithmically [12]. The point at which the energy loss rate by bremsstrahlung and ionisation are equal, is called critical energy E_c . The critical energy for solids and liquids is [18]

$$E_c = \frac{610 \text{ MeV}}{Z + 1.24}, \quad (5)$$

for gases

$$E_c = \frac{710\text{MeV}}{Z + 0.92}. \quad (6)$$

For atomic numbers $Z > 13$ the critical energy can be approximated as:

$$E_c = \frac{550\text{MeV}}{Z}. \quad (7)$$

The approximation formulae are reproduced from [18]. Photons also cause a variety of effects when interacting with matter: for low energies (1 eV bis 100 keV) the photoelectric effect occurs. For energies in the domain of 100 keV to 6 MeV photons induce the Compton and pair production process. High energetic photons (up to 16 MeV) are able to cause a nuclear photoelectric effect or a photodesintegration. Figure 16 shows that the photoeffect is the dominant process in lead for an energy up to 1 MeV while the Compton effect is dominant up to 10 MeV. Energy loss of photons of higher energies is dominated by pair production. The numerical value of these energies depend on the medium.

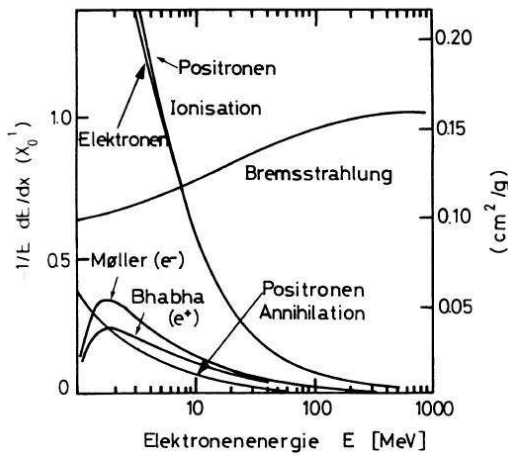


Figure 16: Energy loss mechanism of electrons in lead as a function of the electron energy [12].

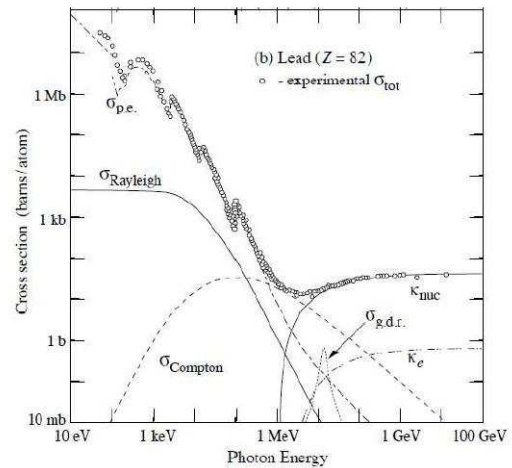


Figure 17: Cross section of photons in lead as a function of the photon energy. $\sigma_{p.e.}$ defines the cross sections of the photoelectric effect etc. [12].

4.1.2 Radiation Length

Electromagnetic calorimeters are designed to detect high-energy electrons, positrons and photons in the GeV range. Electrons lose energy by bremsstrahlung, and photons by pair production

processes. The characteristic amount of matter crossed for these interactions is called radiation length X_0 , measured in gcm^{-2} , when A is again defined in $\frac{\text{g}}{\text{mol}}$. "It is the mean distance over which a highly-energetic electron loses all but $\frac{1}{e}$ of its energy for bremsstrahlung" [18]. The following equation gives an approximation for the calculation of X_0 [18]:

$$\frac{1}{X_0} = 4\alpha r_e^2 \frac{N_A}{A} \left(Z(Z+1) \ln \frac{287}{\sqrt{Z}} \right). \quad (8)$$

4.1.3 Electromagnetic Shower

An electromagnetic shower describes the cascading of high energetic photons. If a photon has an energy of at least twice the electron rest mass, it is able to produce an electron positron pair, while the resulting electrons and positrons in turn can re-emit bremsstrahlung photons. If the energy of these photons is still large enough, they can again produce pairs of electrons and positrons. The particle energy gets reduced until the critical energy is reached where no renewed shower occurs. Electromagnetic showers can be detected by the two electromagnetic calorimeters as it is shown in fig. 18.

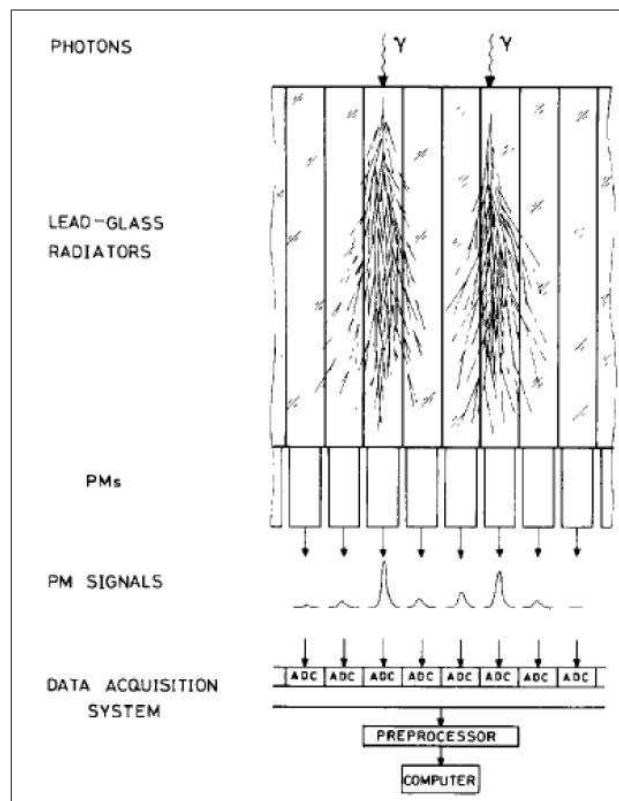


Figure 18: Electromagnetic Shower [12].

The incoming photon (here: from the top) induces an electromagnetic shower in a lead-glass module of an electromagnetic calorimeter. Based on the Cherenkov effect, the e^+e^- of the shower produce light which are converted into electrical signals by photomultipliers (PMs) and finally passed to a DAQ system for readout.

Cherenkov radiation is emitted when a charged particle passes through matter at a constant velocity greater than the speed of light (in that medium). The Cherenkov effect arises when a charged particle passes through matter and produces an asymmetric dipole field (only if the velocity of the particle is $v_{\text{particle}} > \frac{c}{n}$), the emitted dipole radiation is the Cherenkov light.

In connexion with the analysis, we have π^0 s which immediately decay into two photons, whose opening angle depends on its energy. With increasing energy, the two photons are closer together (Lorentz boost) and might not be distinguished from a single photon, which does not come from a π^0 -decay.

Photons are identified by their electromagnetic showers. For very high energies the two photons may lie so close to each other that their showers can't be distinguished. The longitudinal propagation of the shower contains most of the energy. The so called Molière radius R_M gives the scale of the transverse dimension of the electromagnetic shower, given by

$$R_M = \frac{X_0 E_S}{E_c}, \quad (9)$$

with E_S as the scale energy $\sqrt{\frac{4\pi}{\alpha}} m_e c^2 = 21.2 \text{ MeV}$ [18].

4.2 Detection of Photons in Lead Glass

The electromagnetic calorimeters of COMPASS consist of scintillating and lead glass modules. In the following, it will be explained how photons are detected in lead glass.

As mentioned above, the Cherenkov effect produces photons which can be detected by a photomultiplier. The reason why we can't directly detect the incoming photons from a decaying particle, is that the energy of these particles are much too high. A photomultiplier can only detect photons in the visible range. Therefore we use lead-glass with a well defined refraction index. With an injection energy of $E = 10 \text{ MeV}$ electrons lose their energy mainly by bremsstrahlung and photons by pair production processes. The resulting total track length T is the sum over all single tracks and is dependent on the injection energy E and the critical energy E_c [12]:

$$T \propto \frac{E}{E_c} \quad (10)$$

The number of emitted photons can be determined as follows (in $\text{eV}^{-1}\text{cm}^{-1}$) [12]:

$$\frac{d^2N}{dE dx} \approx 370 \cdot \sin^2 \theta_c \quad (11)$$

The probability that an electron produces Cherenkov light at a fixed injection energy depends on the refractive index of the lead glass, according to

$$v > \frac{c}{n} \quad (12)$$

$$\beta > \frac{1}{n}. \quad (13)$$

In order to guarantee that an electron produces Cherenkov light, a certain (not too high) value of the refractive index is needed. The radiation of the Cherenkov light occurs at a fixed angle θ to the direction of flight of the particle. With the angle we are able to calculate the velocity of the incident particle from (see fig. 19)

$$\cos \theta = \frac{1}{\beta n}. \quad (14)$$

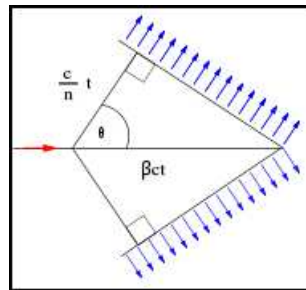


Figure 19: Cherenkov Effect [13].

The number of generated Cherenkov photons ($N_{\text{Cherenkov}}$) and therefore the track length of all electrons and positrons, is proportional to the energy of the primary particle (E_0):

$$N_{\text{Cherenkov}} \sim E_0 \quad (15)$$

Ideally, this correlation is linear but in reality two main problems cause a deviation from linearity: On the one hand photons are absorbed to different degrees. The depth of the shower maximum depends on the initial energy of the incident particle. It means that the maximum of

the shower of high energetic particles is located closer to the photomultiplier. Therefore, the particles have to cover a shorter distance to the detector than low energetics. On the other hand the "leakage-effect" provokes the escape of some particles into the opposite direction of the detector. In summary, these effects provoke a non-linearity which needs to be taken into account in calculations.

4.3 Setup of the Electromagnetic Calorimeters at COMPASS

The COMPASS spectrometer is equipped with ECAL1, located 11.1 m (distance from the target center to the front of ECAL) downstream of the target (commissioned in 2006) and ECAL2 at 33.2 m downstream of the target (commissioned in 2004). ECAL1 is a large angular acceptance calorimeter while ECAL2 is used for small angles. Both calorimeters are mounted on a mobile support in order to move them in the horizontal and vertical direction in the vertical plane, perpendicular to the beam, for calibration purposes.

Fig. 20 shows the schematic view of ECAL1 with a size of $3.97 \times 2.86 \text{ m}^2$ and a central hole of $1.07 \times 0.61 \text{ m}^2$. It has in total 1500 channels. Each channel corresponds to a PM attached to a lead glass module of one of the following types, explained in the following section. The central part is made of 608 GAMS lead glass modules, the rest consists of 572 MAINZ modules and 320 OLGA modules [16]. The beam comes from the front and passes to the hole of the calorimeter.

Fig. 21 gives a schematic view of ECAL2 with a size of $2.44 \times 1.83 \text{ m}^2$ and a central hole of $0.08 \times 0.08 \text{ m}^2$ (for hadron beams) which can be enlarged to $0.38 \times 0.38 \text{ m}^2$ when using a muon beam [16]. ECAL2 is made of 2168 GAMS lead glass blocks with a transverse size of $3.8 \times 3.8 \text{ cm}^2$ each [16]. The central part of ECAL2 is equipped with 900 SHASHLIK modules of the same size. Radiation hard SHASHLIK blocks are used during the hadron run, because of the very high integrated radiation dose.

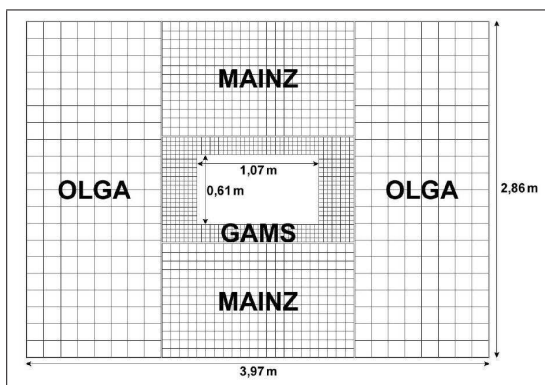


Figure 20: Structure of ECAL1, made of GAMS, OLGA and MAINZ Modules [12].

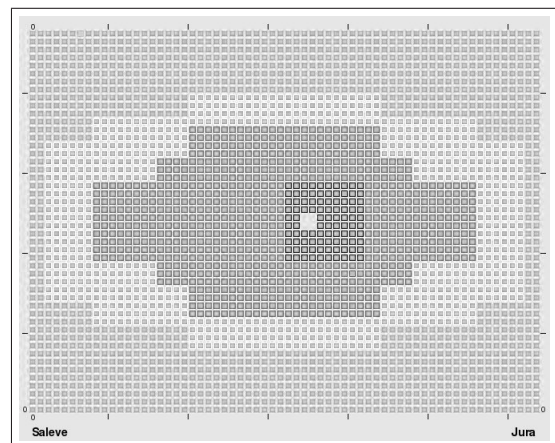


Figure 21: Structure of ECAL2, made of GAMS and SHASHLIK Modules (inner dark grey part).

A detailed description of the location of the GAMS and SHASHLIK modules in ECAL2 can be found in Appendix A.

4.4 ECAL1 and ECAL2 Modules

As already mentioned, there are 3 different lead glass types used in ECAL1 and ECAL2 (GAMS, OLGA and MAINZ), a picture of them is shown in fig. 22. SHASHLIK modules (one is shown also in fig. 22) are no lead glass modules and have a different assembling, which will be explained in the next paragraph.

For ECAL1 it would be desirable to only use one type of modules. Yet, the high material costs of lead glass does not allow it. Therefore, different lead glass blocks from previous experiments are used.

Because of a high radiation dose in the inner part of ECAL2, it needs radiation hard types (SHASHLIK), the outer part is equipped with GAMS modules.



Figure 22: Different lead glass types for ECAL1 and ECAL2: upper and lower module. The central one is a SHASHLIK module [19].

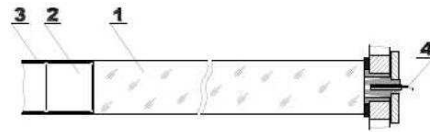


Figure 23: Schematic view of a lead-glass module (GAMS, OLGA, MAINZ) with a lead glass barrel (1) where a photomultiplier (2) is attached, a screening at the top (3) and a fiber plug-in (4) [12].

Each module consists of a lead glass barrel (1) where a photomultiplier (2) is attached with a screening at the top (3) (see fig. 23). For a permanent monitoring a LED or laser fiber (4) can be plugged in. These components form a module. The individual modules vary in different parameters, which are summarized in the following table (3):

	GAMS	OLGA	MAINZ
Type of Lead Glass	TF1	SF5	SF57
PbO-Concentration	50 %	55 %	57 %
Density $\frac{g}{cm^3}$	3.86	4.08	5.51
X_0 [cm]	2.74	2.54	1.55
Molière-Radius [cm]	4.7	4.3	2.61
Refractive Index	1.65	1.67	1.89
Cross-Section [cm ²]	3.82 x 3.82	14 x 14	7.5 x 7.5
Length [cm]	45	47	36
Length [X_0]	16.42	18.5	23.3
Photomultiplier Type	FEU-84-3	XP 2050	EMI 9236 KB
Energy Resolution	$\frac{\sigma}{E} = \frac{0.1}{\sqrt{E[GeV]}} + 0.015$	$\frac{\sigma}{E} = \frac{0.15}{\sqrt{E[GeV]}} + 0.08$	$\frac{\sigma}{E} = \frac{0.07}{\sqrt{E[GeV]}} + 0.02$

Table 3: Properties of the various lead glass modules [12].

The lead glasses consist of a compound of lead oxide (PbO) and silicon oxide (SiO₂) and vary in the percentage share of the two compounds. The modules have different dimensions and lengths. Each module is surrounded by a mylar foil to separate the modules from each other, ensuring that no light is transmitted from one module to another. The mylar foil has a special coating on the inside, to prevent lead from the outside entering the module and destroy its surface.

MAINZ modules are the shortest and most lead-containing modules, while OLGA modules are the biggest and most radiation hard modules. The GAMS modules are very radiation hard due to the blending of Cer to TF1 (TF01). At smaller angles relative to the beam, the electromagnetic shower occurs usually only in one module. This applies only for ECAL1 modules and also not for electromagnetic showers, occurring at large angles of a module. SHASHLIK modules are also very radiation hard and therefore used for the inner part of ECAL2, as already mentioned above.

SHASHLIK Modules

SHASHLIK modules are installed at the inner part of ECAL2. The following figure (fig. 24) shows the schematic view of a SHASHLIK module:

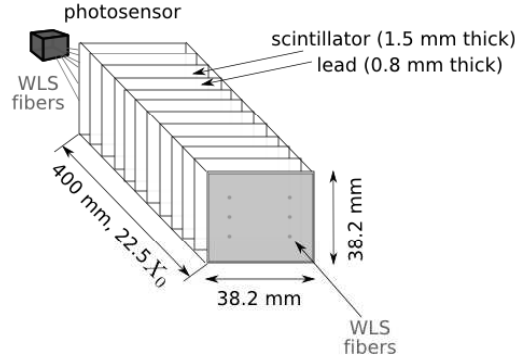


Figure 24: Schematic view of a SHASHLIK module.

A SHASHLIK module, which is used in the electromagnetic calorimeter of COMPASS has a length of 400 mm. One module consists of ≈ 20 alternating lead and scintillator layers (lead/scintillator sandwich). The lead layers have a thickness of 0.8 mm each, while the scintillator layers have a thickness of 1.5 mm. Each plate of the module has a number of holes in it, where WLS (wavelength shifting) fibers are inserted, perpendicularly to the plates. The particles (photons) entering each module from the front. The lead induces electromagnetic showers.

All WLS fibers have a mirror at the "end". This is an aluminium mirror with an additional layer of MgF_2 (magnesium fluoride). These mirrors have an average reflection factor near 80% and are used to prevent that the produced light passes back outwards. The small dots in fig. 24 are the front ends of the WLS fibers. These fibers penetrate the lead/scintillator stacks through holes and transport the produced light to the PM. The fiber ends are collected in one bunch and are viewed directly by a photomultiplier. The following table (4) gives an overview of the SHASHLIK properties:

Dimensions	$38.2 \times 38.2 \text{ mm}^2$
Length	400 mm
Radiation Length [X_0]	17.5 mm
Radiation Thickness	$22.5 X_0$
Scintillator Thickness	1.5 mm
Lead Thickness	0.8 mm
Radiation Hardness	0.5 Mrd
Energy Resolution per 1 GeV Electrons	6%
Lateral Uniformity of Response for Electrons	2%

Table 4: Parameters of the SHASHLIK modules.

The scintillator layers, which were used in SHASHLIK modules, were irradiated by a γ radioactive source up to 500 krad. The light yield of scintillators were measured during this irradiation and a change of light yield was less than 2-3% (used for the definition of the radiation hardness).

4.5 Operation Mode of a Photomultiplier

The produced photons (Cherenkov effect) are now detected by a photomultiplier. These are very sensitive detectors, operating in visible, ultraviolet and near-infrared ranges. They multiply the single photoelectrons, produced by the incident photons by as much as 100 million times. Fig. 25 shows the setup of a common photomultiplier:

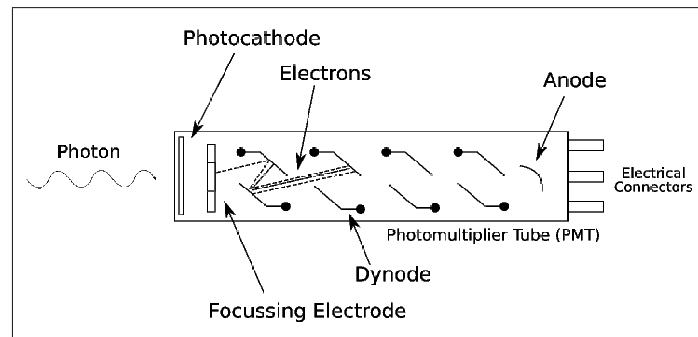


Figure 25: Schematic view of a common photomultiplier tube.

The incoming photons hit a photocathode and due to the photoelectric effect, electrons from the metal are struck out. These electrons hit an electrode, a so called dynode. An entire system of such dynodes is installed, where a high voltage is applied. By applying a high voltage to the dynodes, the electrons are getting accelerated in an electric field and strike on a second dynode, where more electrons are produced (secondary electrons). When the accelerated electrons impinge on the dynode, more electrons are extracted and further accelerated. Therefore, a multiplication of electrons takes place and it creates a cascade of electrons. The amplification factor grows exponentially with the number of dynodes. Typical photomultiplier tubes (PMTs) have about 10 dynodes. Finally, the electrons hit an anode and the resulting charge preponderance can be detected as a current. They produce a voltage drop over a resistor (R) which is the output signal.

As already mentioned, the light is produced by the Cherenkov effect in lead glasses. The γ s of a decaying pion induce electromagnetic showers in the lead glass. The produced charged particles produce light due to the Cherenkov effect. This Cherenkov light is directly detected by the PM. The number of secondary electrons produced is proportional to the number of incident photons, as long as a saturation threshold is not exceeded. Thus, the height of the pulses is proportional to the amount of light (except statistics). This is proportional to the incident photon number and therefore proportional to the intensity of light.

The photomultiplier is normally attached to a base. A base is a mechanical device and a resistive voltage divider network. It is primarily suited to technical instruments requiring single photon or fast timing counting.

4.6 Calibration Methods

The electromagnetic calorimeter has a variety of channels, which have to be calibrated individually. To achieve the most efficient calibration, different methods are used:

- Electron beam calibration
- LED and Laser calibration (online)
- Offline calibration
- π^0 calibration

For the electron beam calibration, electrons with a well-defined energy are taken from the SPS, to calibrate each cell of the electromagnetic calorimeter. In order that the electron beam hits each cell, the calorimeter can be mechanically moved. The scanning of the individual cells is done automatic by a calibration programme. In doing so, the calibration follows a fixed procedure: starting with the bottom left of the calorimeter, the individual cells are scanned in sequence (each row). Fig. 26 shows the calibration procedure for ECAL1 schematically:

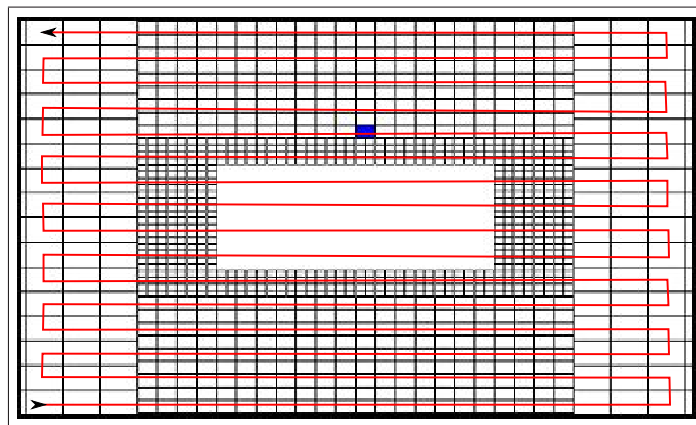


Figure 26: Calibration procedure by using an electron beam (blue marked cell: is currently calibrated); red line = sequence of calibration.

First, the electron beam with a well-defined energy is shot on a single cell and the resulting energy is measured (the energy of the electrons can be adjusted). Thus we get a measurement in between the cells ("inter-calibration"). During the adjacent "global calibration", the energy

deposition of the individual cells are summed up, including the neighboring cells (normally in a 3x3 or 5x5 array). For the analysis, the deposit energy is plotted against the energy of the electron beam. For each module, there is a maximum energy for the energy deposition: 60 GeV for GAMS, 30 GeV for MAINZ and 20 GeV for OLGA modules. One usually starts with a lower energy and then increases slowly up to the maximum value. The duration of such a calibration run is about 10 hours.

While the electron beam calibration proceeds before and between runs, a laser and LED calibration of the electromagnetic calorimeters provides a permanent monitoring and ensures a check of the time stability for reconstruction. The working principle of the laser calibration will be explained in the next section.

An additional software calibration feature ("joujou") is used, to cross check the e^- calibration along with the other calibration methods in an offline mode. Therefore, a special, for COMPASS designed programme is at work. The programme sets an initial energy value for the whole calorimeter (all detectors) and sets a common threshold to reduce the influence of noisy cells. The programme searches for clusters (area of adjacent cells), which fulfill the energy requirements the programme provides (shower reconstruction). The cluster with the maximum energy is chosen and the total energy of this cluster is utilized to calibrate the cells in this cluster by calculating "calibration coefficients". The following formula describes the coherence of the measured total energy E_{tot} of the cluster, the signal of each cell A_k and the calibration coefficient C_k (calculated as the mean weighted values of E_{tot}):

$$E_{\text{tot}} = \sum_{k=1}^n \frac{A_k}{C_k} \quad (16)$$

To cross check this method, LED signals are used to estimate the calibration coefficients (with the same weight correction of the coefficients). This calibration method is still in process and the plan is to check potential instabilities with and without these corrections. The here given explanations are based on [23] and therefore, for more details I refer to [23].

The analysis of final states with neutral mesons, which will be presented in section 7 of this thesis, have shown instabilities in the π^0 mass reconstruction (section 8). Therefore, a cross calibration with hadrons and muons could be a good possibility to supplement the other calibration methods. This procedure was not yet implemented in COMPASS, but is in ongoing.

5 The Laser Monitoring System for ECAL

An accurate calibration of the electromagnetic calorimeters is the most important requirement for reconstruction and analysis. As described above, one has reverted to different calibration methods. To guarantee a permanent, time stable monitoring for each ECAL channel, a laser calibration system is used.

Laser light with a well defined amount of energy is coupled into each calorimeter module. The read out of each channel then gives the possibility to check how much of the injected light passed the module, in dependence of the applied high voltage. The advantage of such a laser system is that we have a defined amount of energy deposited in the individual modules and the calibration can be done for each module.

The electromagnetic calorimeter ECAL1 already has a laser monitoring available. During the 2008 and 2009 run of COMPASS there was no laser monitoring system for ECAL2 implemented.

The reconstruction of 2008 data has shown some instabilities during runs. Analysis of final states with neutral mesons has shown, that time instabilities in the selected invariant π^0 mass are present (results are shown and discussed in section 8). For this reason it is essential to improve the calibration of the electromagnetic calorimeters and to implement a laser monitoring system for ECAL2. The next section will give a brief introduction into the laser calibration method of ECAL1. Therefore, the explanations of section 5.1 are based on the "ECAL1 Monitoring - laser safety manual" [24].

In addition, test measurements were done (described in the following section), that should pave the way for a laser monitoring system for ECAL2. The experimental setup for this will be explained and first results will be shown. The main goal of this investigation is to show that an implementation of a laser calibration for ECAL2 modules (GAMS and SHASHLIK) is possible.

5.1 Experimental Setup for ECAL1

As mentioned above a laser monitoring system for ECAL1 is already installed. Fig. 27 shows the experimental setup for the ECAL1 laser monitoring system:

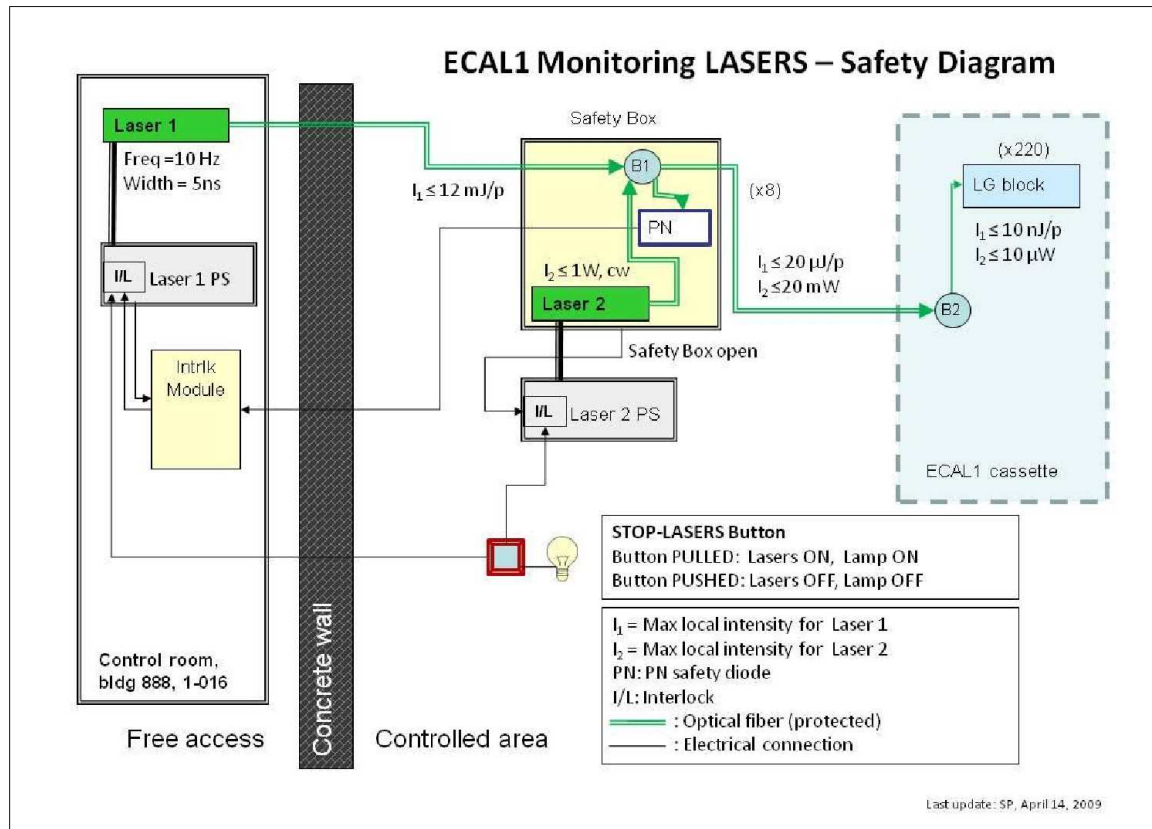


Figure 27: ECAL1 calibration system: schematic view [24].

For the laser monitoring system two different lasers are needed: The pulsed Continuum Minilite-1 laser (laser Type-1: see more technical details in the data sheet: Appendix B) is installed in the free access area of the COMPASS barrack, outside of the radiation controlled area (EHN423 control room). It is used for the permanent monitoring of the calorimeter modules of ECAL1. A second laser (Changchun New Industries MGL-H laser Typ-2) is required for fast discharge of the high voltage Cockroft-Walton system [24]. Laser-1 is always used during a data taking period, while laser-2 is fired only during high voltage settings [24]. Table 5 gives an overview of the main properties of the two lasers.

Characteristics	Laser-1	Laser-2
Product Name	Continuum Minilite-1	CNI MGH-L-512
Type	Pulsed	Continuous
Wavelength (nm)	512	512
Maximum Pulse Energy (mJ)	12	n/a
Operational Pulse Energy (mJ)	≈ 1	n/a
Pulse Width (ns)	5	n/a
Pulse Rate	1-15 Hz	n/a
Maximum Power Output (mW)	180	1000
Operational Power Output (mW)	≈ 10	1000
Operation during Data Taking	Continuously	On demand

Table 5: Characteristics of laser-1 and laser-2 for the ECAL1 calibration: nominal and operational values (as used in the COMPASS experiment) [24].

The primary transmission fiber is coupled to laser-1 via an attenuator and transmits the light directly to a safety box, which is located in the controlled area. This long transmission fiber transports the laser light from the free access area to the 1500 lead glass blocks of the electromagnetic calorimeter ECAL1.

The safety box (installed on top of ECAL1) contains an integrating sphere (B1), which dispenses the incoming laser light from the primary transmission fiber to 9 secondary fibers (the operating mode and further details on the integrating sphere are discussed in the next section).

8 of these fibers are connected to a second integrating sphere (B2), which distributes the light to 8 secondary fiber bundles, consisting of 309 fibers each.

The laser light of the remaining 9-th fiber is detected by a PN diode, which is read-out by a Front End Module (FEM), connected to a laser-1 interlock. For safety reasons, the interlock system is used to turn off the laser in case of potential fiber breakage or in case the safety box is opened while the laser is still switched on.

The 19 fibers from the bundle (309) are combined into one light output. This light output is connected to a PN monitoring diode. 190 fibers of each bundle (out of 290) are connected to the GAMS, MAINZ and OLGA lead glass modules. The remaining surplus fibers are covered with protection caps.

Between the SPS spills, the laser-1 emits light pulses to the lead glass modules (by the COMPASS DAQ) at a frequency of 10 Hz with a pulse width of 5 ns. If a pulse is detected by the FEM, the interlock module authorizes the laser to send the next pulse. If it is not detected (if the fibers are damaged, say), the laser won't send a new pulse. [24]

5.2 Test Measurements for a new ECAL2 Monitoring System

As already explained, a laser monitoring system for ECAL2 is needed. For the development of a new laser system first test measurements must be done. They should first of all show that it is possible to couple enough light into ECAL2 modules. As mentioned above, ECAL2 consists of GAMS and SHASHLIK modules, which have to be checked separately. It is important that we get a direct dependence of the registered signal height in the PMs on the height of the injected laser pulse. The light-coupling plays an important role. Also the spatial dependence of the in- and output and the various technical components (like fibers, optical devices etc.) play a crucial role and will be tested. Furthermore, an analysis is done on different modules of the same type.

5.2.1 Photomultiplier Test with LED

First of all it was checked whether the photomultiplier (PM) of the lead glass module is operational for test measurements. The detection of an electron signal is the first important test to prove whether the PM works. All later experiments were done using the same PM.

To check the functionality of the PM, it is sufficient to use pulsed LED light. We utilized blue ($\lambda = 420\text{-}490\text{ nm}$) or green ($\lambda = 490\text{-}575\text{ nm}$) LEDs, both wavelengths can be used for these tests. However, it is important that one uses light in the visible wavelength range, because our photomultiplier can only work in that range. Fig. 28 shows the experimental setup for the test:

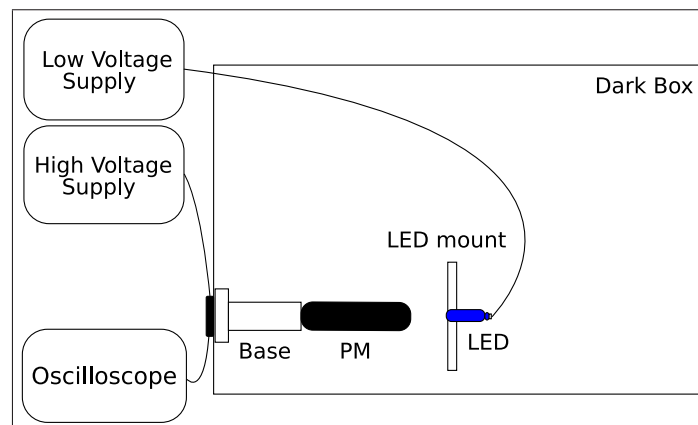


Figure 28: Setup for photomultiplier tests with a LED.

The electrons will be triggered by the incident light which a LED produces. Hence a LED is installed on a small wood mount at a small distance in front of the PM. The LED is supported by a low voltage supply ($\approx 2\text{V}$). The PM with the base and the LED are installed in a dark box to reduce disturbing light influential from the outside and to avoid damages of the PM.

First of all, the LED was put at a fixed distance in front of the PM and was fed with low voltage. The PM was powered with high voltage. After increasing the high voltage ($U(\text{HV}) \approx 2014 \text{ V}$) a first signal at the oscilloscope was seen (see fig. 29):

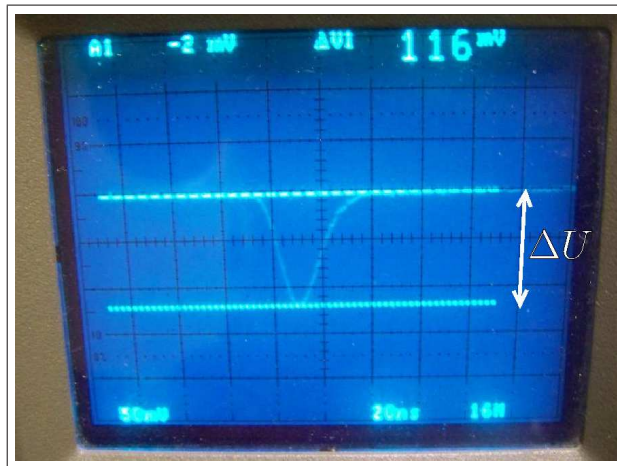


Figure 29: Oscilloscope view of the electron signal with ΔU = measured voltage drop (signal rate). [voltage base = 50 mV per div, time base = 20 ns per div].

The origin of the signal has been already explained in the section about the working principle of photomultipliers. The signal level is assigned by the voltage difference ΔU (as shown in fig. 29) and is provided by the oscilloscope. The following test measurements are based on the measurement of the voltage difference ΔU .

Starting with the measurements the high voltage was set to $U(\text{HV}) = 1000 \text{ V}$ and subsequently, slowly increased to 1800 V. A very clean signal was seen. When the LED was switched off, no signal was seen at the oscilloscope. The input of background effects was very small.

The experimental setup is indeed installed in a dark box and also protected by a black cloth, but it is almost impossible to shield it from all disturbing light. Moreover, there are always thermal electrons which could contribute to the signal. At this point, no quantitative conclusions are drawn. Seeing the signal only shows, that the PM works, when the LED is switched on and that there is no signal seen, when the LED is switched off.

5.2.2 GAMS Modules

After it was shown that the PM works, first PM tests with ECAL2 GAMS modules were done. The purpose is to test, whether it is possible to couple LED and laser light into a GAMS module.

PM testing (GAMS module)

For a start, LED light was coupled into a GAMS module. A GAMS module was therefore attached to the just tested PM, nothing else was changed in the previous experimental setup. The following figure 31 shows the setup of this measurement:

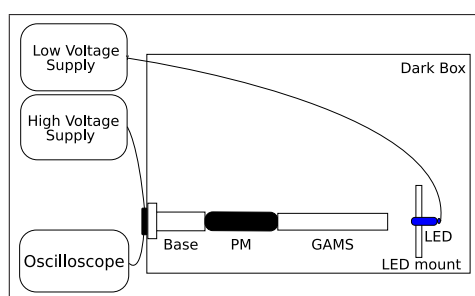


Figure 30: Experimental setup for LED test measurements with a GAMS module.

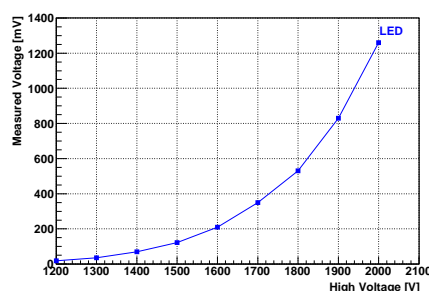


Figure 31: Gain curve of the voltage measurement for a GAMS Module with LED light.

The high voltage was subsequently, slowly decreased from $U[\text{HV}] = 2000 \text{ V}$ to $U[\text{HV}] = 1200 \text{ V}$ in 100 V steps. The following table shows the measured voltages ΔU and figure 31 represents the gain curve of the PM with the attached GAMS module by the use of a LED light input. The errors had so little value that they were not taken into account.

High Voltage [V]	ΔU [mV]
2000	1260
1900	830
1800	530
1700	350
1600	210
1500	120
1400	70
1300	40
1200	20

Table 6: Measured voltage ΔU [mV] for the PM with an attached GAMS module with LED light, in dependence of the high voltage HV [V].

The gain curve shows an exponential increase. At even larger voltages, a saturation should appear and the curve should end up in a straight curve. The reason why we don't see it here, is because the high voltage wasn't set to high enough values. So it can be shown, that in increments of the high voltage the output signal gets stronger. This is what we expected.

Collectively, we can say that the LED light at this wavelength can be coupled into the GAMS module, otherwise we would not have seen any signal. In the following, the same GAMS module was used to test, whether it is possible to couple laser light into it.

Experimental Setup for Laser Test Measurements

Figure 32 shows the experimental setup for the laser tests:

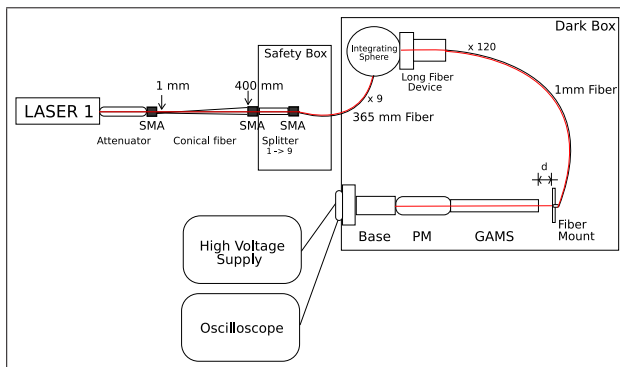


Figure 32: Experimental setup for test measurements with a GAMS module, using a laser.

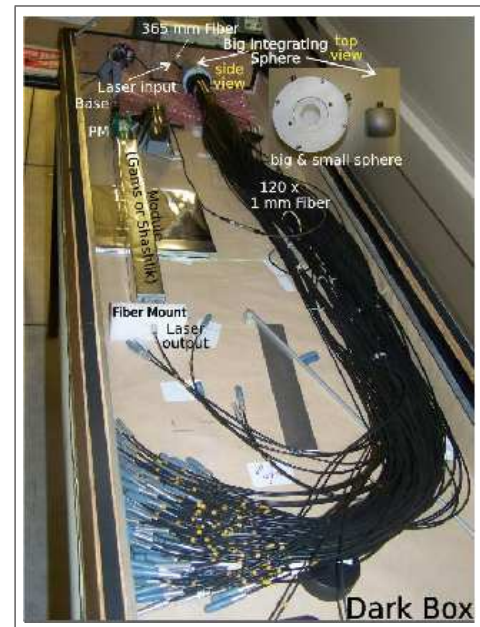


Figure 33: Inside view of the dark box for laser test measurements.

For this measurement laser-1, in the free access area of the COMPASS experimental hall, was used. The intensity of the laser is the same which is used for the laser calibration of ECAL1 and it was not changed during this test. The experimental setup was installed in the free access area.

Laser-1 (with an internal attenuator) is connected to a conical fiber (1 mm to 400 mm) via SMA connectors. The second SMA connector is plugged into a splitter, which splits the primary fiber to 9 fibers. One of these fibers is directly connected to an integrating sphere (will be explained in detail in the next paragraph).

The splitter, as well as the 9 fibers are installed in a safety box to avoid eye damages in case of

fiber breaks or careless handlings of the optical components. It was essential to switch off the laser in case of opening this safety box.

The output of the integrating sphere is connected to a fiber bundle of 120 fibers ($d = 1\text{mm}$). One of these fibers is installed in a wood mount and situated in front of the module. The integrating sphere, the fiber bundle, the wood mount and the module components including the base is installed in a dark box, to avoid induced light from the outside. See a photo of this dark box in figure 33. The dark box is also covered with a black cloth to diminish disturbing light from the lab.

Integrating Sphere

An integrating sphere, also called Ulbricht sphere, is a technical optical device for various purposes: It can produce diffuse light from aligned radiation or it can be used for the integration of radiation from divergent light sources. Fig. 34 illustrates the schematic view of an integrating sphere:

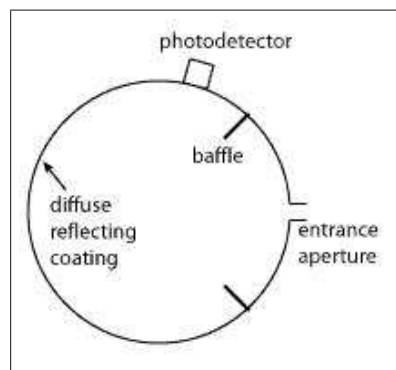


Figure 34: Schematic view of an integrating sphere [25].

On the one side (entrance aperture), light is coupled into the hollow sphere (in our case: by attaching a fiber) which is then reflected within the sphere, covered with a diffuse reflecting coating (like barium sulfate BaSO_4 or Polytetrafluoroethylene "Teflon") on the inside. The light leaves the sphere in a 90° angle of the input port. The output port can be attached directly to a detector or to an output fiber, like it was done in our measurements. The opening port always has a much smaller internal diameter than the sphere to guarantee the numerous reflections of light within the sphere. Thus in our case, we can achieve a high light power and can distribute this light to many fibers simultaneously.

There are different designs of spheres. The following picture (see fig. 35) shows the big sphere (left), and a small sphere (right) which were operated in the test measurements. The size of these spheres and their technical characteristics can be found in the data sheets (Appendix C). The sphere is installed in a hollow cylinder, where the ports are located on the top. The fiber bundle is connected to the large opening (see again fig. 33).

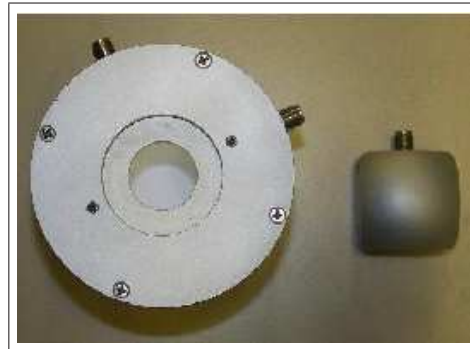


Figure 35: Two integrating spheres, installed in their protection mount (LMU test spheres).

Laser Tests (GAMS Module)

With the above-described setup, laser light was coupled into a GAMS module (GAMS Nr. 99). A high voltage of $U(\text{HV}) = 1200 \text{ V}$ was adjusted and the measured voltage at the PM was the following:

High Voltage [V]	ΔU [mV]
1200	3000

Table 7: Measured voltage ΔU [mV] for a GAMS module with a laser, in dependence of the high voltage HV [V].

As expected, it is possible to couple enough light into GAMS to see a clear signal at the PM. Here exactly the same laser settings (which was already described in the previous section) was used, as in ECAL1. The same ECAL1 high voltage was preset (which can be seen in the laser calibration table of ECAL1 GAMS modules in Appendix D).

Therefore, the here installed setup with the new integrating test sphere works for GAMS modules. In order to compare the laser and LED efficiency, an extrapolation of the measured ΔU of GAMS with the LED gain curve was made. Fig. 36 shows the two gain curves (logarithmical):

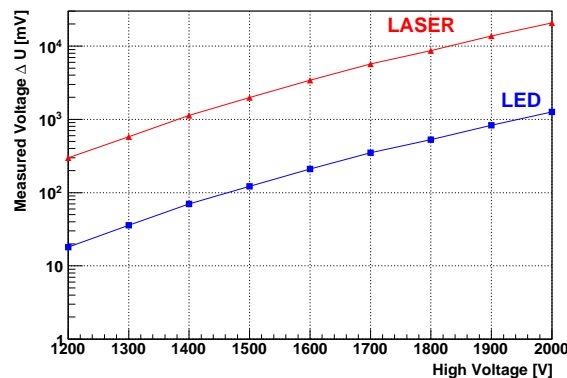


Figure 36: Comparison of the laser and LED gain curve (GAMS module).

Comparing the two curves, we can see that we get about a factor of 10 more light into the GAMS module by using a laser.

5.2.3 SHASHLIK Modules

Test of the Light Coupling

After it could be demonstrated that it is possible to couple sufficient light into a GAMS module with the new setup, we now have to check whether this works also for SHASHLIK modules.

The first main task was to see if the laser light intensity is high enough for a SHASHLIK module. Therefore we tested the light coupling into one module (Nr. 99). The distance of the fiber output and the SHASHLIK module was set to $d = 2.7$ cm, a low laser intensity was applied and was not changed during course of the first laser tests. Again, we used the same light intensities as used for ECAL1 monitoring in 2009 run. The measured voltages are shown below:

High Voltage [V]	ΔU [mV]
2000	270
1500	30

Table 8: Measured voltage ΔU [mV] with laser light (SHASHLIK module), in dependence of the high voltage HV [V].

A very good signal was seen. There is more or less a factor of 10 of voltage reduction by decreasing the high voltage by 500 V. From these results we conclude, that with the current setup we get enough light power to produce a sufficiently high signal at the PM by attaching a SHASHLIK module.

Laser Tests (SHASHLIK Module)

By applying different high voltages, we tested the PM with an attached SHASHLIK module by using laser light. Table 9 shows the results of this measurements by applying a high voltage of $U(\text{HV}) = 2000 \text{ V}$ at the PM and decreasing it to $U(\text{HV}) = 1200 \text{ V}$ in steps of 250-300 V:

High Voltage [V]	ΔU [mV]
2000	270
1750	98
1500	20
1200	3.9

Table 9: Measured voltages ΔU [mV] in dependence of the applied high voltage (SHASHLIK module).

Fig. 37 shows the gain curve of the PM (SHASHLIK module) logarithmical and additionally, the previously estimated gain curve of the PM (GAMS module):

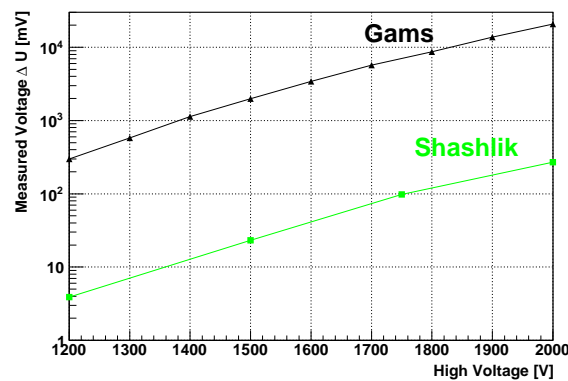


Figure 37: Comparison of the PM gain curves (SHASHLIK and GAMS).

If one increases the high voltage to much bigger values, one could possibly see a saturation. It was not done in these tests to avoid possible electronic damages in the PM. One can see from the plot, that it is possible to couple more laser light into a GAMS module than into a SHASHLIK module (**a factor of 10^2 more**).

If one compares that with the LED curve of the GAMS module (see 36), one can clearly see that it is impossible to use LED light for a SHASHLIK module (**a factor of $\sim 10^3$ too low**). This is based on the different light collection modes of the two modules (explained in section 4).

Therefore, we have to use laser light for the realisation of a permanent monitoring system for SHASHLIK modules. A higher laser intensity would also be benefiting for more light out-

put. Therefore, one may need two different lasers for both ECAL2 modules (lower intensity for GAMS modules).

Following the last measurement, the high voltage was reset to $U(\text{HV}) = 1750 \text{ V}$ and one has seen, that the originally voltage agreed with the previously measured. It proves that the results are reproducible, so we can conclude, that the setup is working and that the LMU test sphere has a good light coupling and can be used for SHASHLIK modules.

Modification of the distance between the Laser and SHASHLIK

In addition, the geometrical dependence of the laser light output and coupling was tested. For that purpose, the distance of the fiber mount and the SHASHLIK module was changed. Figure 38 shows the distance between the fiber and the module. It was only varied in the x direction (left, right), without any angular changes. We tested 3 different intervals: $d = 1 \text{ cm}$, $d = 5 \text{ cm}$ and $d = 10 \text{ cm}$. The voltage of the PM was measured for every distance. Fig. 39 shows the measured voltage ΔU in dependence of the distance d .

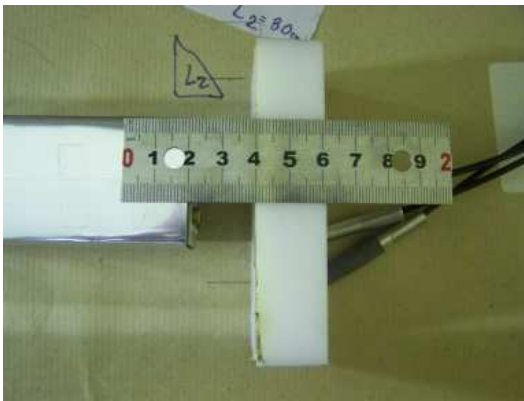


Figure 38: Distance of the fiber mount and the SHASHLIK module.

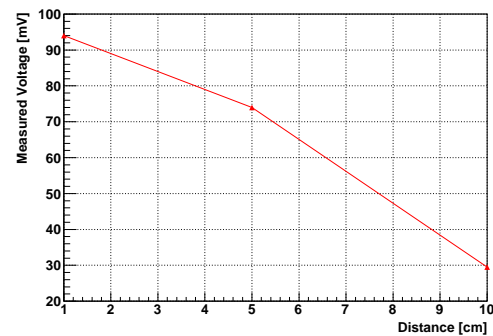


Figure 39: Measured voltages ΔU [mV].

As one can see, the signal strength (ΔU) decreases with growing distance. This demonstrates a direct spatial dependence on the distance between light output (fiber mount) and input into the SHASHLIK module. Even with changes in distance of $\Delta d = 4 \text{ cm}$, considerably less light is coupled into the module, a factor of about 20 mV less. This fact should be considered in a laser monitoring system. You can not place the fiber mount directly in front of the module (without any distance), because then it is not possible to illuminate all light guides of the module at the same time (see: assembling of a SHASHLIK module in the previous chapter).

Test with different Laser Intensities

The distance between the laser output and the SHASHLIK module was now set to $d = 2$ cm (distance from the first light coupling test) and was left at this fixed position. The originally measured voltage of $\Delta U = 99$ mV at a high voltage of $U(\text{HV}) = 1750$ V was reproducible. We therefore can presume, that our measurement is stable.

Subsequently, the laser intensity was increased (no exact intensity values of the laser could be determined) and the voltages were measured for two different high voltage presettings. The results are shown in the following table 10:

High voltage [V]	Voltage [mV] with original intensity	Voltage [mV] with higher intensity
1750	98	3000
1500	20	1000

Table 10: Measured voltage with the laser intensity from the ECAL1 adjustment and measured voltage with a higher laser intensity at two different HV settings.

By increasing the laser intensity, the voltages increase by a factor of 30-50. With an increased laser power, we can see very well that we are able to couple a significantly higher amount of light into SHASHLIK modules. However, it is not possible to arbitrarily increase the laser intensity, because the fibers could be damaged.

The deviations to the previous measurement appears to be due to a too short waiting time for stabilizing the laser. A response time of 30 minutes is recommended. For further tests, the laser intensity was set back to the original value (ECAL1 adjustment).

Tests with different SHASHLIK Modules

At a fixed distance of the laser output and using the same photomultiplier, 5 different SHASHLIK modules have been attached to the PM. The high voltage was set to $U(\text{HV}) = 1750$ V for all tests. The results are summarized in the following table 11:

Module Number	High voltage [V]	ΔU [mV]
99	1750	98
117	1750	40
121	1750	55.5
334	1750	85
337	1750	116

Table 11: Measured voltage ΔU for different SHASHLIK modules, at the same high voltage $U(\text{HV}) = 1750$ V.

ΔU nearly varies in the same range, but there are some voltage differences for the different module types. The reason is, that the light coupling is different for every module. The fiber is never on exactly the same position (angular dependency) as it was before (after exchanging every module by hand). However, we see that the laser coupling not only works for one module, but can be applied to different modules.

Usage of a small sphere instead of the splitter

The last laser test on SHASHLIK modules was done with a small sphere (as shown in fig. 35) instead of the splitter (see experimental setup in fig. 32), to see if one can use an integrating sphere instead of a splitter. A 1 mm fiber was used as a primary fiber instead of using the conical fiber, because the SMA connectors of the conical fiber did not fit to the small sphere. The high voltage was set to $U(\text{HV}) = 1750 \text{ V}$ and we measured a voltage of $\Delta U = 8 \text{ mV}$.

A clear signal was visible on the oscilloscope. For this reason, it was demonstrated that this sphere is usable as a splitter. A factor of 10 less to the original signal was seen. Therefore the laser intensity was increased and we received a higher signal. We came to the conclusion, that this sphere can be used instead of a conventional splitter. The disadvantage is however, that with this sphere, a higher laser intensity is required.

5.2.4 Conclusion and Outlook

To realize a future laser calibration system for ECAL2, tests with ECAL2 modules have to be done previously. Within the scope of this thesis, the following test measurements with GAMS and SHASHLIK modules were performed:

- Photomultiplier test with a LED
- LED test with an attached GAMS module
- Laser test with an attached SHASHLIK and GAMS module
- Light coupling test with a SHASHLIK module
- Distance dependencies of light output and module coupling
- Changing of laser intensity
- Tests with different SHASHLIK types
- Usage of a small integrating sphere instead of a splitter

These measurements do not have the claim to create a complete laser calibration but to show that it is possible to couple enough laser light into GAMS and especially SHASHLIK modules. The tests also show, what we must respect in the installation of the fibers (distance, angular dependencies etc.) and which laser settings are required for each module.

It could be shown, that it is not possible to use LED light for a SHASHLIK module, therefore we are not able to implement a LED monitoring system for ECAL2 (only works for GAMS modules and MAINZ and OLGA modules in ECAL1). One can see from the results, that it is possible to couple more laser light into a GAMS module than into a SHASHLIK module (a factor of 10^2). Because we are able to couple laser light into a SHASHLIK module, a laser monitoring system is realisable.

To implement a complete laser calibration for ECAL2, some things must be clarified. One must look at how many integrating spheres are required, to provide light for all ECAL channels and where exactly they have to be attached to the calorimeter. One integrating sphere provides light for approximately 120 fibers (as it was used in the test measurements), so one needs about 30 spheres for all modules. Furthermore, all fibers have to be checked, not only one (like it was done in the test). All channels and all fibers have to be tested directly at ECAL2. ECAL2 could need two lasers, because SHASHLIK modules require a higher laser intensity. One must also consider how the laser light can be split and which attenuators are needed.

Of time and hardware reasons, it was not possible to carry out these tests in the context of this diploma thesis. The shown tests pave the way for a future laser calibration for ECAL2, which is planned for 2011.

6 Data Reconstruction and Analysis at COMPASS

To analyze large amounts of data in experimental particle physics, a comprehensive software environment is required. The data pass through several selection and processing stages which are presented in the following.

The task is to interpret raw detector information gaining accessible physics information, such as vertex and track information. Raw data is first decoded using a Data Decoding library. Data from calibration and slow control measurements (time-dependent inputs) are stored in a MySQL data base [9].

6.1 The COMPASS Data Reconstruction Programme CORAL

With the help of the DAQ and MySQL data base the programme CORAL is able to reconstruct vertices and tracks for every processed event, while the reconstruction occurs in several steps. First of all, the data read-out of the hardware is digitized and transformed into time information and signal amplitudes. For that purpose abstract electronics identification numbers of all detector channels are mapped to real 3-dimensional coordinates [28]. These information shed light on particle trajectories, using magnets (SM1, SM2) and the RICH detector. Subsequently, the output is written into mDST (Mini Data Summary Tree) files which can be deconstruct by the analysis tool PHAST.

6.2 The Physics Analysis Software Tool PHAST

The produced mDST files can be read by PHAST, which provides access to reconstructed event information and allows the processing and filtering of event sub-samples [10]. Moreover, PHAST allows to use standardized selection routines for analysis purposes and gives the opportunity to create reduced mDST files (called μ DST) which contain preselected event samples.

6.3 The Data Analysis Framework ROOT

ROOT is an object-orientated analysis tool (written in C++) to analyze data in high energy physics. Root was developed in the context of the NA49 experiment (Large Acceptance Hadron Detector) [29]. The data is structured in branches and stored in trees on an event-by-event basis [29]. The results can be presented visually in order to analyze and evaluate it. This programme plays an essential role in the COMPASS analysis work. It provides an efficient way to archive

diverse data in a structured way (also high amounts of data). All our non-calibration data are stored in ROOT-files (raw, mDST).

7 Analysis of Final States with Neutral Mesons

7.1 Event Selection

The data selection of the reactions $\pi^- p \rightarrow \pi^- \pi^0(\eta)p$, $\pi^- p \rightarrow \pi^- \pi^0 \pi^0(\eta\eta)p$ and $\pi^- p \rightarrow \pi^- \eta' p$ with an incoming negative pion beam at $E_{\pi^-} = 190$ GeV will be described in the following chapter.

The description here is done on the basis of the Release COMPASS Note "Study of diffractively and centrally produced resonances in $\pi^- p \rightarrow \pi^- \pi^0(\eta)p$, $\pi^- p \rightarrow \pi^- \pi^0 \pi^0(\eta\eta)p$ at 190 GeV" by I. Uman, S.C. Dinter and E. Romero Adam for the Hadron Analysis Group [26].

For the analysis, which is presented in this diploma thesis, the principle of particle identification and reconstruction is based on the idea, that a neutral particle (like the π^0) decays into two photons which are detected. All particles that participate in this reaction are detected by various detectors.

A π^0 or η meson, in the final state $\pi^- p \rightarrow \pi^- \pi^0(\eta)p$ rapidly decays into two photons, whose energy and position are assigned by the electromagnetic calorimeters of the COMPASS experiment (figure 40). The data selection occurs in several steps, which will be described in the following: the trigger selection [1], the beam composition [2], vertex selection (within the target) [3], RPD criteria [4] and cluster selection in ECAL1 and ECAL2 calorimeters [5]. In addition, kinematic fitting routines were integrated into the data selection to improve the reconstruction [6] (see fig. 40), the numbers in fig. 40 refer to numbers given in the text.

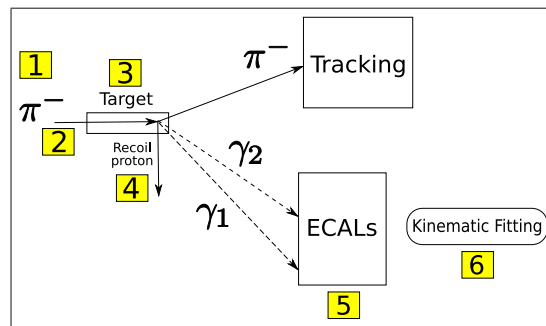


Figure 40: Selected event topology for the reaction $\pi^- p \rightarrow \pi^- \pi^0(\eta) p$ for data selection plus the numbers which refer to the given explanations in the text.

The selection of $\pi^- p \rightarrow \pi^- \pi^0(\eta) p$, $\pi^- p \rightarrow \pi^- \pi^0 \pi^0(\eta\eta) p$ and $\pi^- p \rightarrow \pi^- \eta' p$ works in almost the same way. The differences will be explicitly mentioned in the appropriate part. The results of the analysis will be shown in the following chapter.

The latest version of the 2008 COMPASS software tools were used to perform the selection which includes $\gamma\gamma$ shower separation from high energetic π^0 decays in the forward calorimeter [16]. The present analysis is performed on a part of 2008 data, which means a data taking period of nearly 2 weeks. The cuts which were used for the selection are described in the following.

In total $\sim 10^9$ events (for each channel) with an incoming π^- beam at $190 \frac{\text{GeV}}{c}$ were processed to select $\pi^- p \rightarrow \pi^- \gamma\gamma p$, $\pi^- p \rightarrow \gamma\gamma\gamma p$ and $\pi^- p \rightarrow \pi^- \pi^+ \pi^- \gamma\gamma p$. The precise statistics, like the total amount of processed events will be shown in section 7. There will also be summarized, how many events are lost after performing a cut and how many events are in the final sample.

1 Trigger

The preselection is done with the DT0 Trigger, therefore a smaller amount of the total events were recorded by the DT0 Trigger.

The DT0 is a hadron trigger which is used in 2008 data to select diffractive produced events [27]. The composition of the DT0 trigger is the following (used for minimum selection criteria):

- The Beam Trigger is used to trigger on events occurring in the target region. To respect the geometrical properties of the target, such as its round shape, this trigger is provided [27].
- A Proton Trigger is used to select recoiling protons emitted from the target. These protons are detected by the Recoil Proton Detector (RPD). They are selected by time-of-flight and energy loss measurements [27].
- The Veto system is used to detect secondary particles produced along the beamline (hadronic interactions), halo particles, non-interacting particles and interactions leading to particles going outside the angular acceptance of the spectrometer and to reject such events. [27].

2 The π^- Beam

The incoming beam from the M2 beam line is not a pure pion beam: It contains kaons (4.5%) and anti-protons (0.5%) [11]. To exclude negatively charged kaons of the incoming beam, a majority of hits in CEDAR 1 and CEDAR 2 less than 6 was claimed (Majority < 6 for CEDAR 1 and CEDAR 2). This cut reduces the small fraction of kaons. Figure 41 shows the hits, which occur in CEDAR 2 versus the hits arising in CEDAR 1. The events in the upper right corner are from kaons, pions produces hits in the lower left corner. After performing this cut (fig. 42), the kaons are almost excluded. Unfortunately, an exact percentage of the rejected kaons is unknown. One possible explanation for not knowing the exact value is that only $\frac{1}{3}$ of the beam is tagged by the CEDARs.

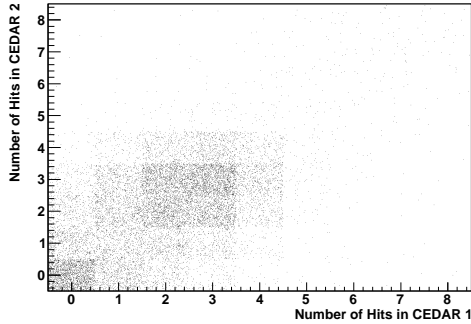


Figure 41: Number of hits in CEDAR 2 versus CEDAR 1 for pions (lower left corner) and kaons (upper right corner).

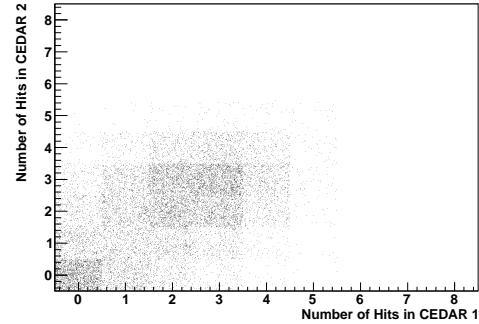


Figure 42: Number of hits in CEDAR 2 versus CEDAR 1 for pions (after cut).

3 Vertex Selection

For vertex selection we are asking for exactly one primary vertex. A primary vertex is an interaction point of the beam hitting the target (in a fixed target experiment). In collision experiments this interaction point is defined as the point where the particles collide. Due to pileup events, which often occur in the reconstruction, we lose a lot of statistics. "Pileup are background events which are added to the observed signal [30]. They originate in multiple events that appear in the same time window as the signal of interest. Pileup frequently occurs in high luminosity experiments, such as colliding experiments, where multiple collisions can happen during a single bunch crossing" (definitions are taken from [30]).

There is one outgoing negative charged track (π^-) per vertex in the reactions $\pi^-p \rightarrow \pi^-2\gamma p$ and $\pi^-p \rightarrow \pi^-4\gamma p$, while we expect 3 charged tracks in $\pi^-p \rightarrow \pi^-\pi^+\pi^-2\gamma p$ ($\pi^-\pi^+$ occurring from the decay of $\eta' \rightarrow \pi^-\pi^+\eta$ and one negative track from the beam (π^-). The incoming pion beam and the outgoing track(s), including the $\gamma\gamma$ s from the decaying π^0 and η form the primary vertex.

Each individual track can be defined by a Lorentz vector. With its help, we can get information about the energy of each track. In order to reduce the pileup events, we claim, that the energy of the track is less than 180 GeV. In the case of 3 outgoing particles, the sum over all energies is requested to be less than 180 GeV. Tracks with higher energies (~ 190 GeV) could be wrongly constructed as tracks with diffractive or centrally produced vertices and therefore, they are rejected. Only one good track is requested for the π^0 and η channels, for the η' final state 3 charged tracks per primary vertex are requested.

Additionally, the primary vertex must satisfy the following conditions. To ensure that only events are taken, whose vertices occur in the hydrogen target itself (interactions in the target), the subsequent requirements are used:

- The primary vertex is within $-69 \text{ cm} < z_{\text{vertex}} < 29 \text{ cm}$ (longitudinal dimension of the target).
- The primary vertex is at a distance of $r_{\text{vertex}} < 1.5 \text{ cm}$ from the beam axis (radial dimension of the target).

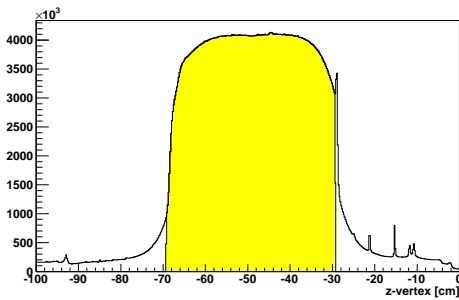


Figure 43: The primary vertex distribution along the z -axes for $\pi^-p \rightarrow \pi^-p + \text{neutrals}$. The primary vertex is chosen to be within the yellow shaded area.

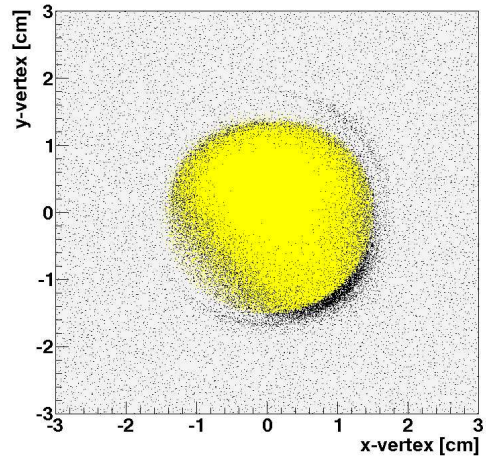


Figure 44: The primary vertex distribution along xy -axes for $\pi^-p \rightarrow \pi^-p + \text{neutrals}$. The primary vertex is chosen to be at a well defined distances ($r_{\text{vertex}} < 1.5\text{cm}$) from the beam (yellow shaded area). The visual contrast of the shown picture could deceive here.

4 RPD Criteria

For the azimuthal correlation between the direction of the flight of a recoiling track (proton in this case) in the RPD with the direction of the flight of the negatively charged pion and the $\pi^-4\gamma$ system, the azimuthal angle was required to be in the range of $-0.3 < \phi_{\pi^-4\gamma} - \phi_p < 0.3$ (see fig. 45) [26].

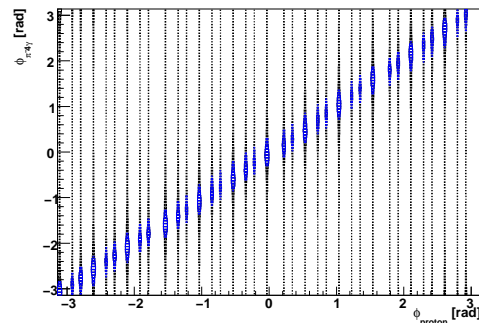


Figure 45: Azimuthal angle of the recoiling proton (track) in the RPD detector vs. the azimuthal angle of the $\pi^-4\gamma$ system.

5 Cluster Selection in ECAL1 and ECAL2

2 or 4 γ s result from the π and η decay, therefore exactly 2(4) clusters were selected in ECAL1 and ECAL2, in accordance with the following criteria (description taken from [26]):

- Each cluster, which is detected by the electromagnetic calorimeters, correlates to an electromagnetic shower in a group of neighbouring crystals. These clusters are not pointed by a charged track.
- To get a better signal to "background ratio", an additional condition was set: we selected the cell which had the highest energy deposit and divided this value by the total energy of the cluster. This ratio must be 92%: $\frac{E_{\text{cell}_{\text{max}}}}{E_{\text{cluster}}} < 0.92$. Figure 46 shows the ratio of the energy deposit with the cluster energy ($\pi^-p \rightarrow \pi^-4\gamma p$).

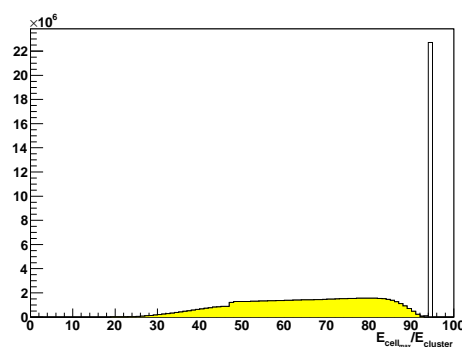


Figure 46: Ratio of energy deposits in cell with maximum energy with the cluster energy of GAMS (ECAL1) and MAINZ cells. Noisy channels are excluded demanding $\frac{E_{\text{cell}_{\text{max}}}}{E_{\text{cluster}}} < 0.92$ (yellow shaded area).

The explanation for that cut is the following: In a normal case the energy deposition would be evenly distributed over the entire space of the cell, with a maximum energy of cell_{max} .

Still, it could be shown that in most cases, the ratio cell_{max} energy with the cluster energy has a sharp peak above 0.92%. A possible cause would be that this can be associated to a single photon in an OLGA module, where one single block could contain all the shower energy. If this effect also appears in MAINZ and OLGA modules (MAINZ modules have a smaller size than OLGA modules), it is probably due to clusters produced by electronic noise.

- A minimum of energy deposition in the calorimeter cells is essential, therefore we use 1 GeV for ECAL1 clusters and 4 GeV for ECAL2.
- Since all of the clusters must be in time with the beam, an additional time cut was performed: The difference of the beam time and the cluster time must be within $t = -3$ ns and $t = 5$ ns. Figure 47 illustrates the performed cut.

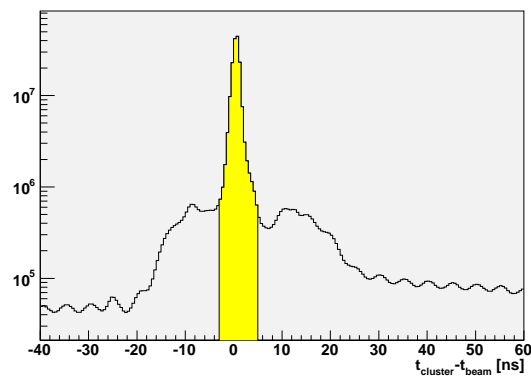


Figure 47: The time difference of the beam with the clusters are extract to be in the range of $t_{\text{low}} = -3$ ns and $t_{\text{high}} = 5$ ns. Clusters fulfilling this exigence are selected.

Photon Energy Correction

The reconstructed invariant mass of the π^0 shows a deviation of ≈ 3 MeV of the PDG mass. These results will be shown and explained in section 8. The possible reasons for this irregularity will also be discussed in section 8. For the analysis of $\pi^- p \rightarrow \pi^- \pi^0(\eta)p$ and $\pi^- p \rightarrow \pi^- \pi^0 \pi^0(\eta\eta)p$, an additional energy correction was applied to correct this problem. The principle of this correction is that it uses symmetric decays of $\pi^0 \rightarrow \gamma\gamma$.

This method is provided by I. Uman and the following explanations are taken from [26].

The angle ϕ between the 2 photons from the decaying π^0 is related to the energy of the 2 photons E_{γ_1} and E_{γ_2} :

$$\begin{aligned} m_{\pi^0}^2 &= 2E_{\gamma_1}E_{\gamma_2}(1 - \cos\phi) \\ &= 4E_{\gamma_1}E_{\gamma_2}\sin^2\left(\frac{\phi}{2}\right) \\ &= \frac{1}{2}E_{\pi^0}^2(1 - A^2)(1 - \cos\phi) \end{aligned} \quad (17)$$

where $E_{\pi^0} = E_{\gamma_1} + E_{\gamma_2}$ is defined as the pion energy and $A = \frac{|E_{\gamma_1} - E_{\gamma_2}|}{E_{\gamma_1} + E_{\gamma_2}}$ is the measure of asymmetry of the decay process. If we require that $E_{\gamma_1} \approx E_{\gamma_2} \approx E_\gamma$ and $A \approx 0$, we can come to the conclusion

$$m_{\pi^0}^2 \approx 4E_\gamma^2 \sin^2\left(\frac{\phi}{2}\right) \quad (18)$$

$$m_{\pi^0} \approx 2E_\gamma \sin\left(\frac{\phi}{2}\right). \quad (19)$$

With this method, the photon energy can be "scaled", by calculating $\sin(\frac{\phi}{2})$ for the measured energy and to de- or increase the energy by $\Delta E_\gamma = \frac{\Delta m_{\pi^0}}{2 \sin(\frac{\phi}{2})}$, accepting that $2 \sin(\frac{\phi}{2})$ is a constant (for the measured energy).

The photon energy correction method provides different photon energy correction functions for the individual cell types of ECAL1 and a correction for ECAL2. The parameters of these functions for ECAL1 cells are calculated by fitting the invariant masses of the π^0 with first and second order polynomial functions. For ECAL2 we assume a global correction function.

6 Kinematic Fitting

Experimental measurements of quantities like momentum, mass, timing, 4-vectors etc. are always fraught with errors. For this reason we need a procedure which is able to improve our measurements and to give optimal results.

A kinematic fitting routine is a mathematical process, that uses physical constraints to enhance the measurements. To check the performance of the fitting two distributions are used:

- Confidence level distribution
- Pull distribution

The confidence level distribution checks the amicability of a fit (data) to the hypothesized event, while the pull distribution estimates the quality of the error estimation. Kinematic fitting works as follows: Using a reliable hypothesis (π^0 , η mass) for an event, one can derive constraints which convert the measured values within their error to fulfill special requirements.

It is assumed that one has n independent measurements. Therefore, we get measured values y , which correspond to true values η that are affected by a measurement error ε . These errors follow the Gaussian law. The covariance matrix contains the resolution errors and correlation coefficients of the tracking parameters [31]. The coherence of the measured and the true value is the following

$$y = \eta + \varepsilon. \quad (20)$$

We have a set of n equations, which fulfill the following condition (constraints)

$$f(\eta) = 0. \quad (21)$$

We are now able to calculate the errors. Therefore, we have to minimize the least-squares form

$$\chi^2 = \varepsilon^T C^{-1} \varepsilon \quad (22)$$

and we have to fulfill the constraint equation,

$$f(y - \eta) = 0. \quad (23)$$

Then $\mathbf{y}-\eta$ can be seen as an enhanced measurement of η , that fullfills the constraint equation [31]. If the constraints are linear the solution can be directly calculated, if they are non-linear an iteration is needed to find the solution.

Confidence level

"The confidence level is the probability that a χ^2 , higher than the one observed would occur" [31]. The Confidence level can be defined as:

$$CL(\chi^2) = \int_{\chi^2}^{\infty} F(x, n) dz. \quad (24)$$

$F(x, n)$ ist the χ^2 probability distribution ($n = \text{degrees of freedom}$). After performing the fit we have to check the agreement between the data and the hypothesis by using the confidence level. With no background one would expect a flat distribution, which ranges from 0 to 1. Background events produce a sharp peak near to 0. These events do not satisfy the hypothetical constraint equation and can be removed. Loosing these events means a reduction of the background. Figure 48 and figure 49 show the confidence level for the reaction $\pi^- p \rightarrow \pi^- \pi^+ \pi^- \gamma \gamma p$ with a π^0 hypothesis (fig.48) and η hypothesis (fig. 49) (mass constraint).

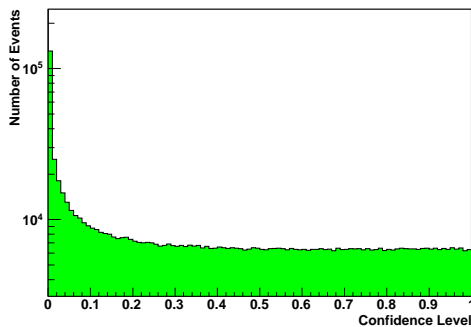


Figure 48: Confidence level for the reaction $\pi^- p \rightarrow \pi^- \pi^+ \pi^- \gamma \gamma p$ with a π^0 hypothesis (constraint).

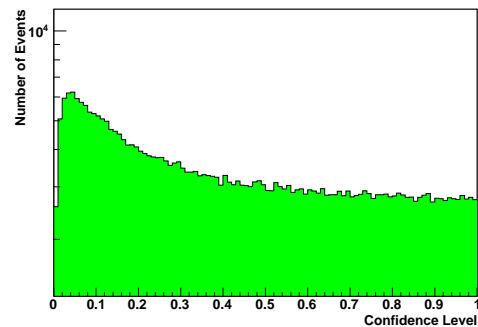


Figure 49: Confidence level for the reaction $\pi^- p \rightarrow \pi^- \pi^+ \pi^- \gamma \gamma p$ with an η hypothesis (constraint).

For high values of χ^2 we expect a low confidence level. χ^2 is a quantity parameter for the deviation of the measured values to the hypothesis.

Pull distribution

The second check to see how the measured values fit to the hypothetical assumption can be done by the use of so-called pull quantities. The pulls are defined as [31]

$$p_i = \frac{\varepsilon_i}{\sqrt{C_{ii} - C'_{ii}}}. \quad (25)$$

The C_{ii} and C'_{ii} define the diagonal elements of the covariance matrix before and after the fit. ε_i is the measurement error of the value. One would expect a gaussian distribution for every pulls p_i around 0.

Figure 50 shows the pulls for the π^0 from $\pi^-p \rightarrow \pi^-\pi^+\pi^-\gamma\gamma p$. The two images in the top row show the horizontal direction component of the upper and lower photons, the two pictures in the middle present the pull distribution of the vertical direction of the upper and lower photon. The third row shows the pulls of the energy.

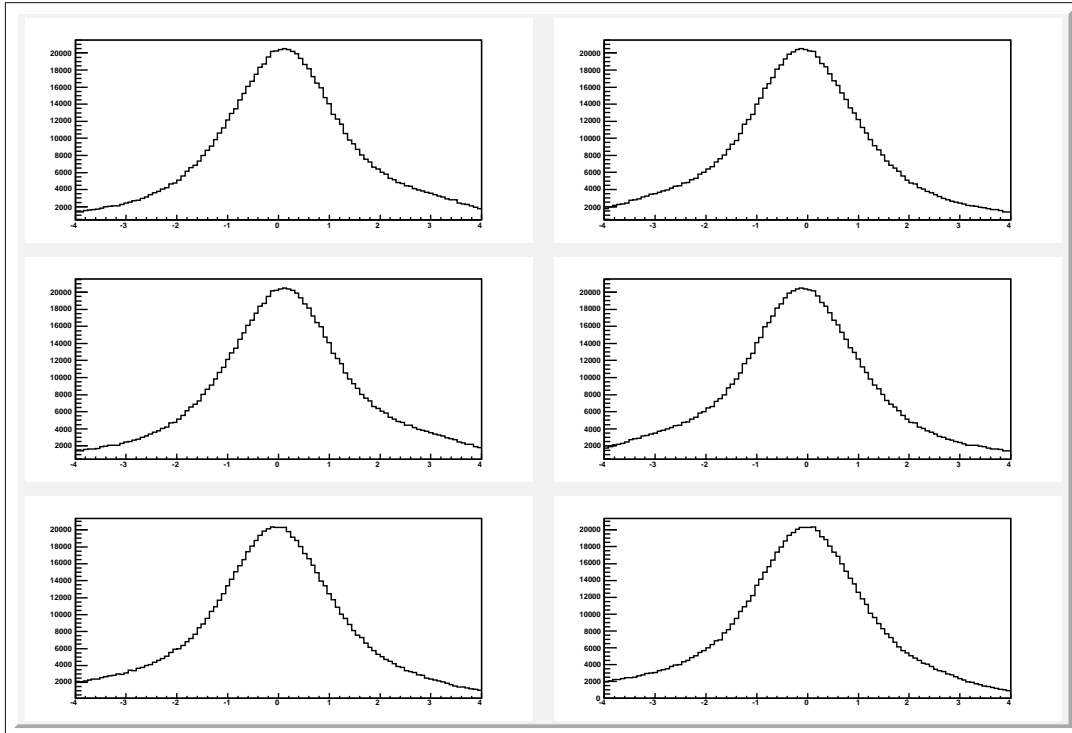


Figure 50: Pulls π^0 (from: $\pi^-p \rightarrow \pi^-\pi^+\pi^-\gamma\gamma p$): The images in the top row show the horizontal direction component of the upper and lower photons; The images in the middle present the pull distribution of the vertical direction of the upper and lower photon; The images in the third row show the pulls of the energy.

The pulls are distributed around zero, but one can recognize a deviation from the Gaussian shape. This phenomenon might be explained by a bad estimation of the errors of the measured data. The pulls are shifted to small energies what leads to a broadening of the pulls.

Figure 51 shows the pulls distribution for the η from $\pi^- p \rightarrow \pi^- \pi^+ \pi^- \gamma \gamma p$:

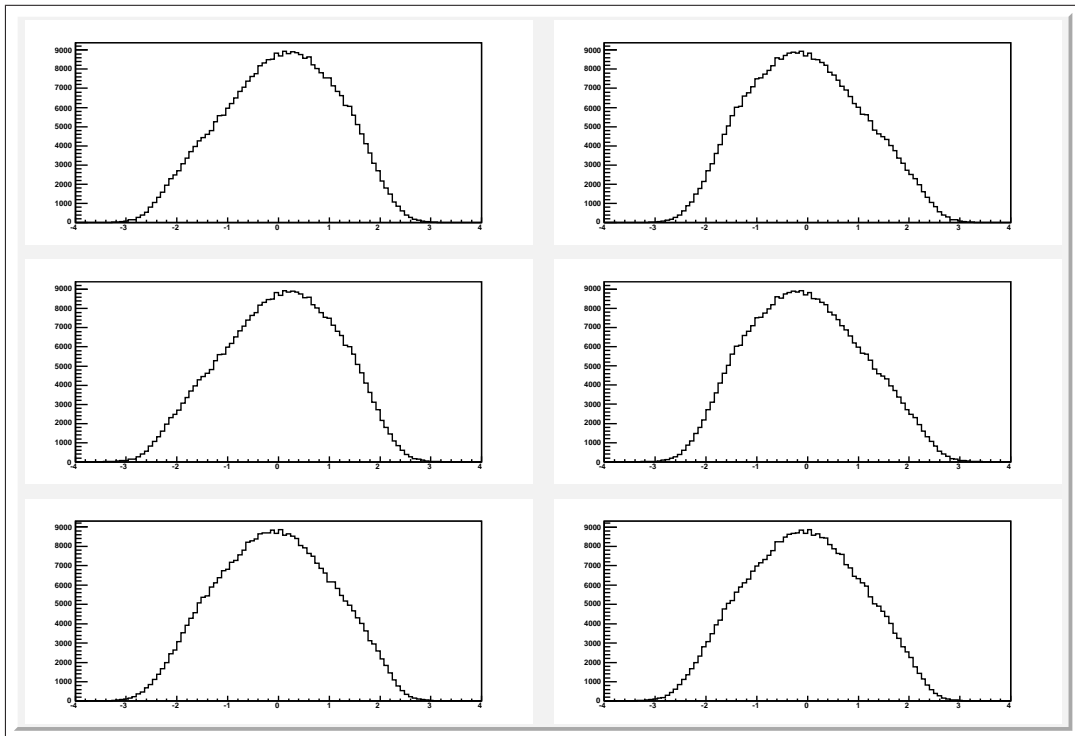


Figure 51: Pulls η (from $\pi^- p \rightarrow \pi^- \pi^+ \pi^- \gamma \gamma p$): The images in the top row show the horizontal direction component of the upper and lower photons; The images in the middle present the pull distribution of the vertical direction of the upper and lower photon; The images in the third row show the pulls of the energy.

The distribution shows also a deviation from the Gaussian shape and they are not exactly centered around zero, which can be explained by systematic overestimations or underestimations of the respective quantities (energy). The bottom pulls are contracted, owing to the fact that the energy has been overestimated.

Kinematic fitting was performed in this analysis for all 3 channels. The fitting was done on the π^0 and η invariant mass and some example results are shown in fig. 52 for the fitted π^0 in $\pi^-p \rightarrow \pi^- \pi^+ \pi^- 2\gamma (= \pi^0)p$ and in fig. 53 for the fitted η in the reaction $\pi^-p \rightarrow \pi^- \pi^+ \pi^- 2\gamma (= \eta)p$. One can clearly see that the width of the peaks is reduced by using the kinematic fitter and the signal gets much cleaner.

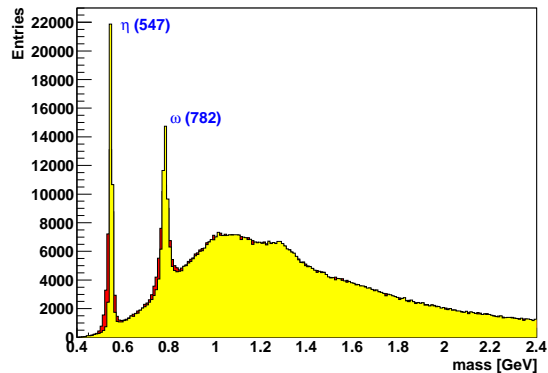


Figure 52: Invariant mass of the 3 body system $\pi^+ \pi^- \gamma \gamma (\pi^0)$ before (red shaded area) and after (yellow shaded area) the kinematic fit.

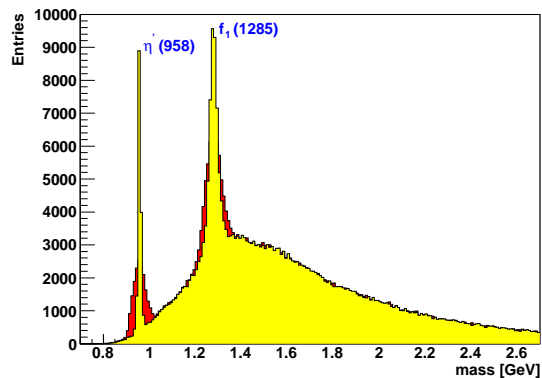


Figure 53: Invariant mass of the 3 body system $\pi^+ \pi^- \gamma \gamma (\eta)$ before (red shaded area) and after (yellow shaded area) the kinematic fit.

The fitting was only performed on the invariant mass of the particles (one constraint). A vertex fitting (energy, momenta of the particles as constraints) would improve the data quality and will be implemented in future data reconstruction and selection procedures at COMPASS.

7.2 Data Statistics and Invariant Mass Spectra

7.2.1 $\pi^- p \rightarrow \pi^- \gamma \gamma p$

The reaction $\pi^- p \rightarrow 2\gamma p$ with an incoming π^- beam of 190 GeV was studied to select $\pi^- p \rightarrow \pi^- \pi^0(\eta)p$. 70 runs of the week W37 of 2008 COMPASS data (≈ 2 weeks of data taking) were used to analyze the final state $\pi^- p \rightarrow \pi^- \pi^0(\eta)p$. In total, $8.2453 \cdot 10^8$ events were processed. Tab. 12 summarizes the performed cuts and shows the statistics for $\pi^- p \rightarrow \pi^- 2\gamma p$:

Period	≈ 70 runs of W37 (2008 data)
Number of processed events	$8.2453 \cdot 10^8$
DT0 Trigger	$6.142 \cdot 10^8$
Majority < 6 for CEDAR1 and CEDAR2	$6.061 \cdot 10^8$
Primary Vertex	$5.613 \cdot 10^8$
Target: $-69 \text{ cm} < z_{vertex} < -29 \text{ cm}$	$4.573 \cdot 10^8$
Target: $r_{vertex} < 1.5 \text{ cm}$	$4.452 \cdot 10^8$
1 negative track	$4.452 \cdot 10^8$
2 golden clusters	8969327
$-0.3 < \phi_{\pi-4\gamma} - \phi_p < 0.3$	2144789
Exclusivity ($180 < E_{\pi-4\gamma} < 200 \text{ GeV}$)	542467
$100 < \pi^0 < 170 \text{ MeV}$	235766
m_{π^0} 1 Constraint, CL > 10 % (π^0 mass)	129055
$450 < m_\eta < 650 \text{ MeV}$	91301
η 1 Constraint, CL > 10 % (η mass)	38945

Table 12: Statistics for $\pi^- p \rightarrow \pi^- 2\gamma p$ (≈ 70 runs of W37 2008 data).

This section will present the invariant mass plots of the π^0 , η , $\pi^- \pi^0$ and $\pi^- \eta$. Fig. 54 and fig. 55 show the invariant $\gamma\gamma$ mass around the π^0 mass (PDG mass $m_{\pi^0} = 134.9766 \pm 0.0006 \text{ MeV}$) and around the η mass (PDG mass $m_\eta = 547.75 \pm 0.12 \text{ MeV}$).

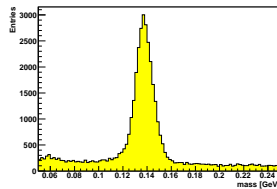


Figure 54: Invariant $\gamma\gamma$ mass around the π^0 mass from $\pi^- p \rightarrow \pi^- \gamma \gamma p$.

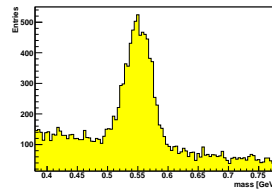


Figure 55: Invariant $\gamma\gamma$ mass around the η mass from $\pi^- p \rightarrow \pi^- \gamma \gamma p$.

Both peaks arise as a very clean signal, with less background. The mass of both particles differs by 3 MeV of the nominal mass without adding the photon energy correction. The reason for that will be explained in section 8, where the here selected π^0 s are used for performance checks of the electromagnetic calorimeters.

The selected π^0 and η from the final state $\pi^-p \rightarrow \pi^- \pi^0(\eta)p$ can be combined with the negatively charged π^- to form all possible resonances, which decay into $\pi^- \pi^0$ or $\pi^- \eta$ states. The following two figures will show the $\pi^- \pi^0$ and $\pi^- \eta$ invariant mass plot.

In the invariant mass plot of the $\pi^- \pi^0$ system (fig. 56) a very clean $\rho(770)$ at 0.7 GeV is seen. The $\rho(770)$ with a PDG mass of $m_\rho = 775.8 \pm 0.5$ MeV decays into 2 pions ($\frac{\Gamma_i}{\Gamma} \approx 100\%$). A small accumulation of events at an energy of ≈ 1.7 GeV is visible which may be due to $\rho_3(1690)$ ($\frac{\Gamma_i}{\Gamma} (\rho_3(1690) \rightarrow \pi\pi) = (23.6 \pm 1.3)\%$) or $\rho(1700)$. The decay of the $\rho_3(1690)$ occurs more frequently than the decay of the $\rho(1700)$, as demonstrated by the fact that the branching ratio for the $\rho_3(1690)$ decaying into 2 pions, is known very well. For this reason it is more likely that the small accumulation at 1.6-1.7 GeV is due to $\rho_3(1690)$. An amplitude analysis could clarify which particle we see in this plot.

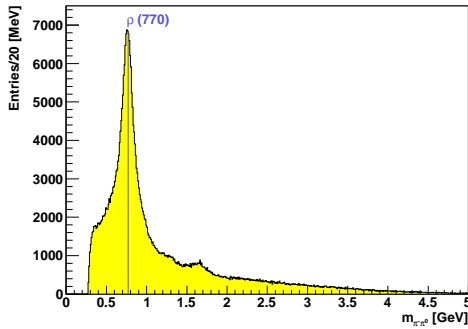


Figure 56: Invariant mass of the $\pi^- \pi^0$ system in the $\pi^- p \rightarrow \pi^- 2\gamma p$ channel. The position of the $\rho(770)$ is indicated.

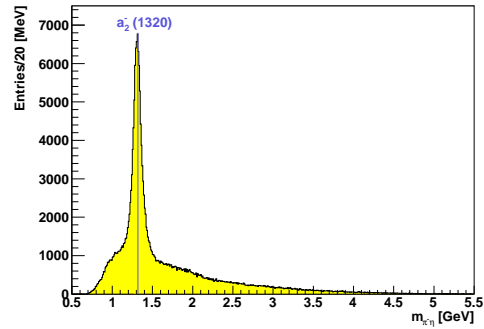


Figure 57: Invariant mass of the $\pi^- \eta$ system in the $\pi^- p \rightarrow \pi^- 2\gamma p$ channel. The position of the $a_2(1320)$ is indicated.

The invariant mass spectrum of the $\pi^- \eta$ system (fig. 57) presents a very nice peak of the $a_2(1320)$ at 1.3 GeV ($\frac{\Gamma_i}{\Gamma} (a_2(1320) \rightarrow \pi\eta) = (14.5 \pm 1.2)\%$). With the eyes, no other significant structure can be seen in this plot. A continuing analysis could clarify the question whether the controversial exotic state $\pi(1400) \rightarrow \pi^- \eta$ exists.

7.2.2 $\pi^- p \rightarrow \pi^- \gamma\gamma\gamma p$

The final state $\pi^- 4\gamma p$ at an incoming π^- beam of 190 GeV was analyzed to select $\pi^- p \rightarrow \pi^- \pi^0 \pi^0 p$ and $\pi^- p \rightarrow \pi^- \eta \eta p$. 76 runs of W37 of 2008 data were analyzed. In total, $1.379 \cdot 10^9$ events were processed. Tab. 13 summarizes the performed cuts and shows the statistics for $\pi^- p \rightarrow \pi^- 4\gamma p$:

Period	76 runs of W37 (2008 data)
Number of processed events	$1.397 \cdot 10^9$
DT0 Trigger	$1.030 \cdot 10^9$
Majority < 6 for CEDAR1 and CEDAR2	$1.014 \cdot 10^8$
Primary Vertex	$9.414 \cdot 10^8$
Target: $-69 \text{ cm} < z_{vertex} < -29 \text{ cm}$	$7.661 \cdot 10^8$
Target: $r_{vertex} < 1.5 \text{ cm}$	$7.451 \cdot 10^8$
1 negative track	$6.974 \cdot 10^9$
4 golden clusters	8573693
$-0.3 < \phi_{\pi^- 4\gamma} - \phi_p < 0.3$	2999774
Exclusivity ($180 < E_{\pi^- 4\gamma} < 200 \text{ GeV}$)	1337869
$\sqrt{(m_{\gamma_1\gamma_2} - m_{\pi^0})^2 + (m_{\gamma_3\gamma_4} - m_{\pi^0})^2} < 25 \text{ MeV}$	938192
2 π^0 2 Constraints, CL > 10 % (π^0 mass)	373664
$\sqrt{(m_{\gamma_1\gamma_2} - m_{\eta})^2 + (m_{\gamma_3\gamma_4} - m_{\eta})^2} < 25 \text{ MeV}$	2312
2 η 2 Constraints, CL > 10 % (η mass)	1829

Table 13: Statistics for $\pi^- p \rightarrow \pi^- 4\gamma p$ (76 runs of W37 2008 data).

The two π^0 s and two η s from $\pi^- p \rightarrow \pi^- \pi^0 \pi^0 (\eta\eta) p$ decay into 4 photons ($\pi^0 \rightarrow \gamma_1\gamma_2$ and $\pi^0 \rightarrow \gamma_3\gamma_4$). Thus, there are 3 possible combinations of the two-photon invariant mass.

Figure 58 shows the 2 dimensional, two-photon invariant mass plot for all 3 combinations around the π^0 mass. The accumulation of events in the lower left corner represents the π^0 . The 3 dimensional plot of the $\pi^0 \rightarrow \gamma_1\gamma_2$ and $\pi^0 \rightarrow \gamma_3\gamma_4$ invariant mass around the π^0 mass is displayed in fig. 59. This histogram is symmetric and hence six-fold. It is a very clean signal with less background.

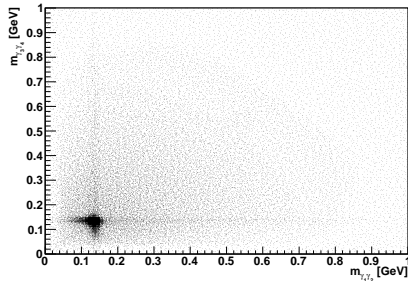


Figure 58: 2 dimensional invariant mass plot of the $\gamma\gamma$ mass versus the $\gamma\gamma$ mass from $\pi^-p \rightarrow \pi^-4\gamma p$.

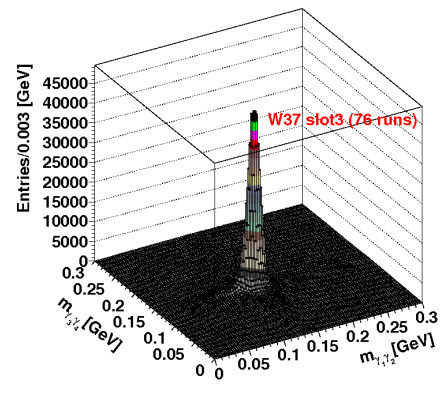


Figure 59: 3 dimensional lego plot of the $\pi^0\pi^0$ signal from $\pi^-p \rightarrow \pi^-4\gamma p$.

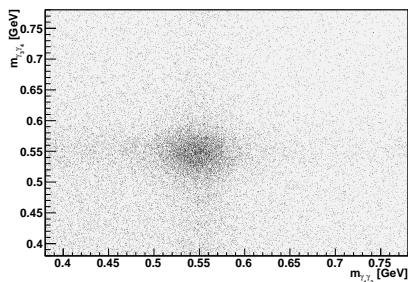


Figure 60: 2 dimensional invariant mass plot of the $\gamma\gamma$ mass versus the $\gamma\gamma$ mass from $\pi^-p \rightarrow \pi^-4\gamma p$.

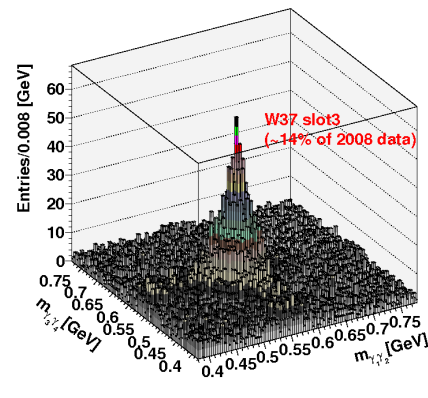


Figure 61: 3 dimensional lego plot of the $\eta\eta$ signal from $\pi^-p \rightarrow \pi^-4\gamma p$.

Due to combinatorial background, it is not possible to see the $\eta\eta$ mass in this plot (fig. 58). The combinatorial background probably comes from wrong combinations of the $\pi^0\pi^0$ signal. Therefore, an additional cut was performed, to reduce the combinatorial background: All events, which have at least one $\gamma\gamma$ invariant mass combination in $100 < m_{\pi^0} < 170$ MeV were discarded [26]. After performing this cut, an $\eta\eta$ signal, at a mass of $m_{\eta} = 547.75 \pm 0.12$ MeV is clearly seen, in the lower left corner of fig. 60. Figure 61 shows the 3 dimensional histogram of fig. 60, which is again symmetric and thus six-fold.

The following two pictures show the fitted invariant $\gamma\gamma$ mass plot around the π^0 mass (fig. 62) and around the η mass (fig. 63). These plots are the projection of the 2 dimensional plot. They

were fitted with a Gaussian function and second order polynomials.

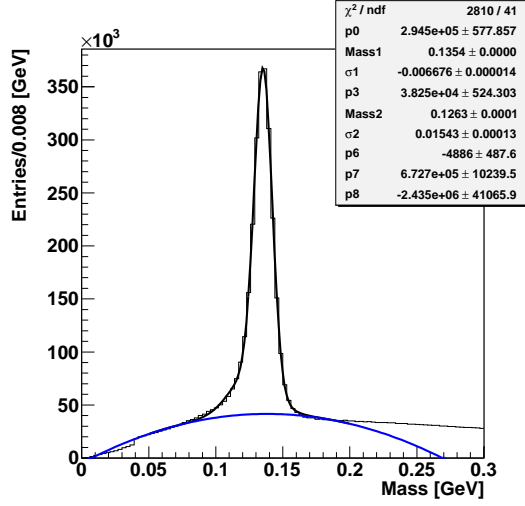


Figure 62: The 2 invariant mass plot (fitted) for the 3 possible $\gamma\gamma$ combinations (76 runs) around the π^0 mass in the reaction $\pi^- p \rightarrow \pi^- 4\gamma p$.

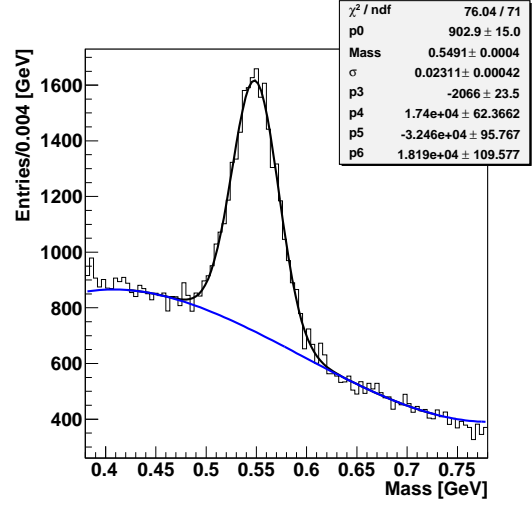


Figure 63: The 2 invariant mass plot (fitted) for the 3 possible $\gamma\gamma$ combinations (76 runs) around the η mass in the reaction $\pi^- p \rightarrow \pi^- 4\gamma p$.

The $\pi^0\pi^0$ and $\eta\eta$ can be combined with the π^- to form all possible resonances which can be observed in the diffractive $\pi^- p \rightarrow \pi^- 4\gamma p$ process. $\pi^- p \rightarrow \pi^- \pi^0\pi^0(\eta\eta)p$ are 3 body final states and therefore there are 3 possible ways to form resonant states: $\pi^- \pi^0$, $\pi^- \pi^0\pi^0$, $\pi^0\pi^0$ and $\pi^- \eta$, $\pi^- \eta\eta$, $\eta\eta$. Thus, we get 6 possible invariant mass plots for the neutral channel $\pi^- p \rightarrow \pi^- 4\gamma p$, which will be shown in the following.

Fig. 64 shows the invariant mass plot of the $\pi^- \pi^0$ system with a very prominent $\rho(770)$ peak. A small bump at 1.6 GeV can be seen, which could be the $\rho_3(1690)$. We saw a strong $\rho(770)$ peak already in the channel $\pi^- p \rightarrow \pi^- \pi^0(\eta)p$. The bump of the possible $\rho_3(1690)$ was more considerable. The signal is less clear in $\pi^- p \rightarrow \pi^- \pi^0\pi^0(\eta\eta)p$, which might come from the combinatorial background of the 4 γ . Fig. 65 shows the fitted $\pi^- \eta$ invariant mass with a clear peak at 0.98 GeV ($a_0(980)$) and a peak around 1.32 GeV (perhaps the $a_2(1320)$).

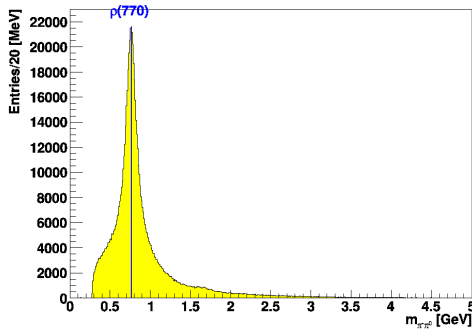


Figure 64: Invariant mass of the $\pi^- \pi^0$ system (in $\pi^- p \rightarrow \pi^- \pi^0 \pi^0 p$). The position of the $\rho(770)$ is indicated.

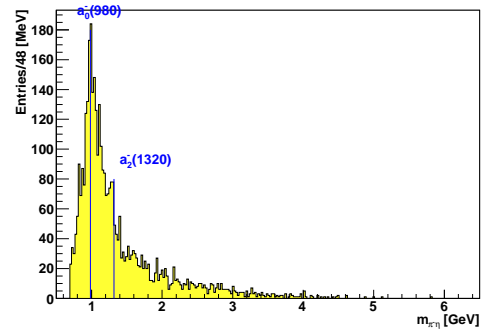


Figure 65: Invariant mass of the $\pi^- \eta$ system (in $\pi^- p \rightarrow \pi^- \eta \eta p$). The positions of the $a_0(980)$ and $a_2(1320)$ are indicated.

The following plots show the invariant mass of the $\pi^0 \pi^0$ (fig. 66) and the $\pi^- \pi^0 \pi^0$ system (see fig. 67). In fig. 66 one can observe most likely the $f_2(1270)$. Even a kaon could be suspected at an energy of 0.5 GeV. In fig. 66 one can clearly see a bump at 1.27 GeV which is due to the $f_0(1270)$ decaying into two pions with $\frac{\Gamma_i}{\Gamma} = (84.8 + 2.5 (-1.3)) \%$. In fig. 67 we see the $\pi^- \pi^0 \pi^0$ system and can clearly see the dominant peak at 1.3 GeV ($a_2(1320)$) and a small accumulation of events at 1.67 GeV, which is supposedly due to $\pi_2(1670)$.

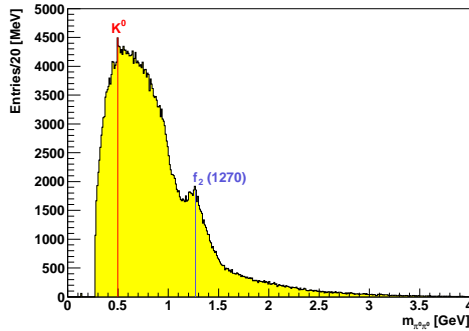


Figure 66: Invariant mass plot of the $\pi^0 \pi^0$ system with an indicated $f_2(1270)$. At 0.5 GeV a red line is indicated, which could be due to a kaon.

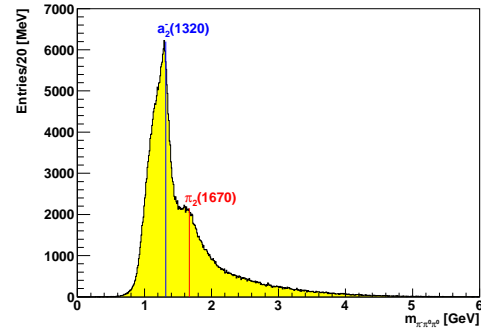


Figure 67: Invariant mass plot of the $\pi^- \pi^0 \pi^0$ system with an indicated $a_2(1320)$ at 1.3 GeV and the $\pi_2(1670)$ at 1.7 GeV.

The invariant mass plot of the $\eta\eta$ system (see fig. 68) shows the first sighting of the known $f_0(1500)$ at 1.5 GeV in COMPASS data. The invariant mass plot of the $\pi^-\eta\eta$ system (see fig. 69) shows a peak at an energy of ≈ 1.8 GeV, which may come from the $\pi(1800)$, decaying into $\pi^-\eta\eta$ (Γ_i is not yet known). No other resonances can be definitely assigned. The accumulation of entries in the right of the peak, probably stems from other effects, we do not understand yet.

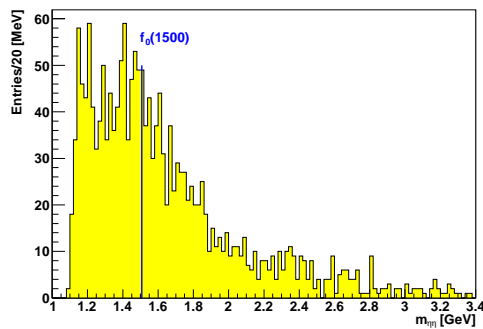


Figure 68: Invariant mass of the $\eta\eta$ system. The position of the possible $f_0(1500)$ is indicated.

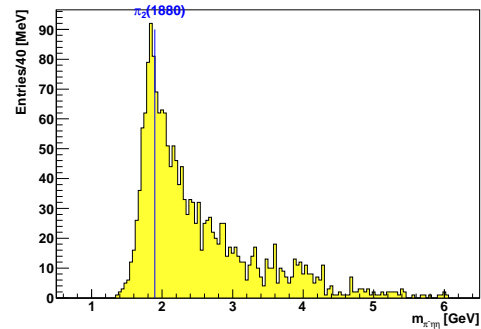


Figure 69: Invariant mass of the $\pi^-\eta\eta$ system. The position of the $\pi(1800)$ is indicated.

7.2.3 $\pi^- p \rightarrow \pi^- \pi^+ \pi^- \gamma \gamma p$

For the selection of the channel $\pi^- p \rightarrow \pi^- \pi^+ \pi^- 2\gamma p$ with $m(\gamma\gamma) = m(\pi^0)$ or $m(\eta)$, 79 runs of week W37 (slot3) of 2008 COMPASS data were processed. These runs are a fraction out of ≈ 300 runs. In total, we have $1.19 \cdot 10^9$ events with an incoming π^- beam at 190 GeV. Table 14 summarizes the performed cuts and the data statistics.

Period	79 runs of W37 (2008 data)
Number of processed events	$1.195 \cdot 10^9$
DT0 Trigger	$8.476 \cdot 10^8$
Majority < 6 for CEDAR1 and CEDAR2	$8.284 \cdot 10^8$
Primary Vertex	$7.602 \cdot 10^8$
Target: $-69 \text{ cm} < z_{vertex} < -29 \text{ cm}$	$6.334 \cdot 10^8$
Target: $r_{vertex} < 1.5 \text{ cm}$	$6.149 \cdot 10^8$
Number of events with ≥ 1 tracks ($\pi^- \pi^- \pi^+$)	$2.457 \cdot 10^8$
2 golden clusters	$1.126 \cdot 10^7$
$-0.3 < \phi_{\pi^- 4\gamma} - \phi_p < 0.3$	52981228
Exclusivity ($180 < E_{\pi^- 4\gamma} < 200 \text{ GeV}$)	2270613
$100 < \pi^0 < 170 \text{ MeV}$	82192
1 π_0 1 Constraint, CL > 10 % (π^0 mass)	34421
$450 < m_\eta < 650 \text{ MeV}$	64523
1 η 1 Constraint, CL > 10 % (η mass)	46757

Table 14: Statistics for $\pi^- p \rightarrow \pi^- \pi^+ \pi^- 2\gamma p$ (76 runs of W37 2008 data).

The following plots (fig. 70 and fig. 71) show the $\gamma\gamma$ invariant mass around the π_0 and the η mass.

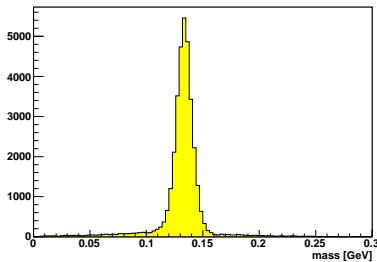


Figure 70: Invariant $\gamma\gamma$ mass around the π^0 mass from the reaction $\pi^- p \rightarrow \pi^- \pi^+ \pi^- 2\gamma p$

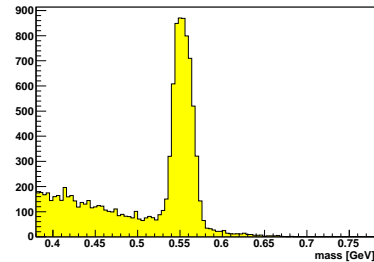


Figure 71: Invariant $\gamma\gamma$ mass around the η mass from the reaction $\pi^- p \rightarrow \pi^- \pi^+ \pi^- 2\gamma p$.

The reconstructed masses of the selected π_0 and η shows that the final selection has only a small amount of background with a reconstructed mass nicely centered at the PDG value. As a result

of the background, the mean value of the η mass is a bit smaller than the PDG value.

Fig. 72 shows the 2 dimensional plot of the $\pi^-\pi^+\gamma\gamma$ invariant mass versus the $\gamma\gamma$ invariant mass.

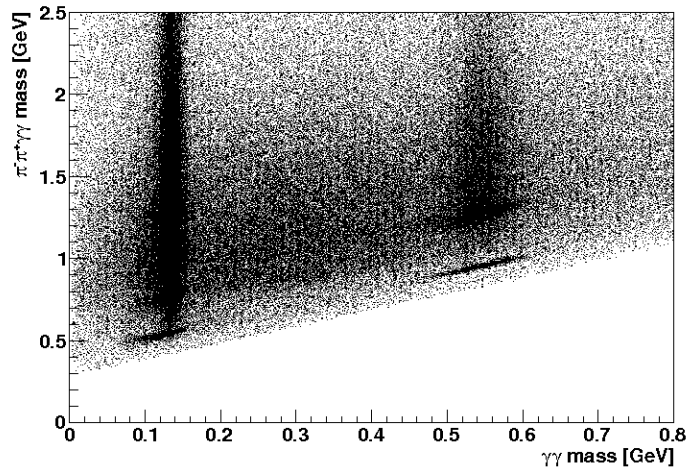


Figure 72: Invariant mass of $\pi^-\pi^+\gamma\gamma$ versus the $\gamma\gamma$ invariant mass.

We can clearly see the $\eta(547)$ and the $\omega(782)$ in the first band (π^0 mass). In the second band (η mass) the $\eta'(958)$ and $f_1(1285)$ are good visible. The diagonal structure arises from the experimental mass smearing, due to the resolution of the experiment.

Figure 73 and 74 displays the invariant mass of the 3 body system $\pi^-\pi^+\gamma\gamma(=\pi^0)$ and $\pi^-\pi^+\gamma\gamma(=\eta)$. The $\eta(547)$ decays into $\pi^-\pi^+\pi^0$ with a fraction of $\frac{\Gamma_i}{\Gamma} = (22.6 \pm 0.4)\%$ [18] and is therefore seen in this plot. It arises as a very sharp needle around the PDG value. The $\omega(782)$ also decays into $\pi^-\pi^+\pi^0$ with $\frac{\Gamma_i}{\Gamma} = (89.1 \pm 0.7)\%$ and is seen as a very clean signal.

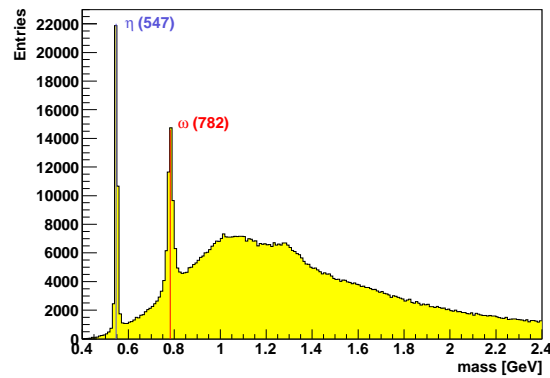


Figure 73: Invariant mass plot of the 3 body system $\pi^-\pi^+\gamma\gamma(=\pi^0)$.

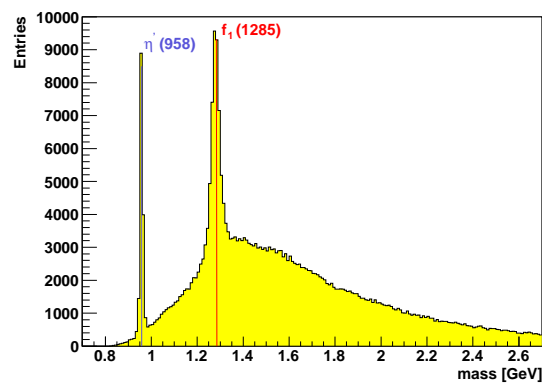


Figure 74: Invariant mass plot of the 3 body system $\pi^-\pi^+\gamma\gamma(=\eta)$.

The η' decays into $\pi^-\pi^+\eta$ ($\frac{\Gamma_i}{\Gamma} = (44.3 \pm 1.5)\%$). The clean η' signal appears as an extremely sharp needle around the PDG value. Those data show a clear $f_1(1285)$. There could be more signals seen in the bump, but they belong to processes, we do not yet understand.

The plot of the 4 body invariant mass $\pi^- \pi^- \pi^+ \gamma \gamma (= \pi^0)$ in fig. 75 shows a very prominent signal of the $a_2(1320)$ which was already seen in the previously mentioned final states.

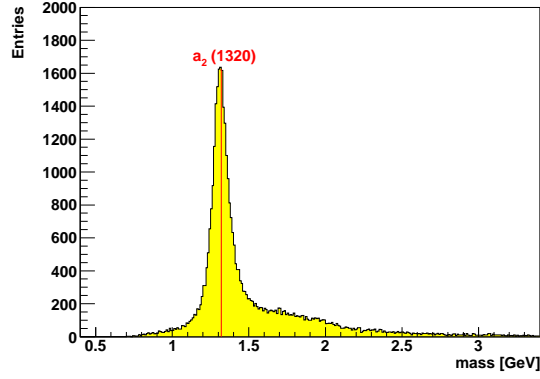


Figure 75: Invariant mass plot of the 4 body system $\pi^- \pi^- \pi^+ \gamma \gamma (\pi^0)$ with 3 body = η .

The 4 body invariant mass $\pi^- \pi^- \pi^+ \gamma \gamma (= \eta)$ plot (fig. 76) shows a peak at an energy of 1.6 GeV. This could be a hint for the occurrence of the controversial exotic $\pi_1(1600)$ which was already seen in the E852 and VES experiment. I used the same statistics (6903 events) that E852 was using. For comparison, I refer to the theory part of this thesis in section 2, where the E852 and VES results were already presented. The plots look very similar.

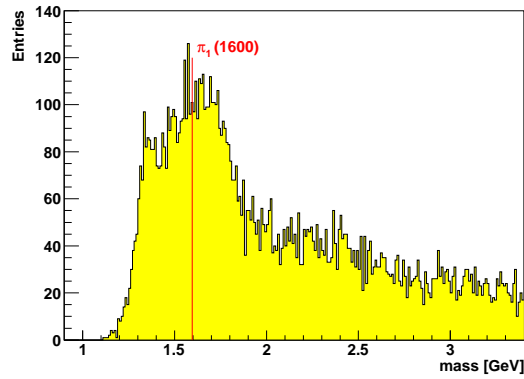


Figure 76: Invariant mass plot of the 4 body system $\pi^- \pi^- \pi^+ \gamma \gamma (\eta)$ with 3 body = η' (6903 events).

Further analysis is needed to clarify, if this is really the exotic $\pi_1(1600)$. Therefore, the 4-vectors of the channel $\pi^- p \rightarrow \pi^- \eta' p$ were already produced, so now we are ready to start with partial-wave-analysis, which will not be presented in this thesis.

7.3 Summary of the Mesons seen in $\pi^-p \rightarrow \pi^-2\gamma p$, $\pi^-p \rightarrow \pi^-4\gamma p$ and $\pi^-p \rightarrow \pi^-\pi^+\pi^-2\gamma p$

Table 15 summarizes the observed and presumably observed mesons/resonances of the previous presented analysis. The particles are presented by ascending mass. It shows the mass in MeV of every particle and the decay mode, in which we have seen them. Additional to that, the branching ratios and ($I^G(J^{PC})$) are given in the last column, taken from [18].

Meson	$I^G(J^{PC})$	M [MeV]	Seen in (Decay Mode)	Γ_i/Γ
π^0	$1^-(0^{-+})$	134.98 ± 0.0006	2γ	$(98.798 \pm 0.032)\%$
η	$0^+(0^{-+})$	547.75 ± 0.12	2γ	$(39.43 \pm 0.26)\%$
			$\pi^+\pi^-\pi^0$	$(22.6 \pm 0.4)\%$
$\rho(770)$	$1^+(0^{--})$	775.8 ± 0.5	$\pi\pi$	$\sim 100\%$
$\omega(782)$	$0^-(1^{--})$	782.59 ± 0.11	$\pi^+\pi^-\pi^0$	$(89.1 \pm 0.7)\%$
η'	$0^+(0^{-+})$	957.78 ± 0.14	$\pi^+\pi^-\eta$	$(44.3 \pm 1.5)\%$
$a_0(980)$	$1^-(0^{++})$	984.7 ± 1.2	$\pi\eta$	dominant
$f_2(1270)$ (?)	$0^+(2^{++})$	1274.4 ± 1.2	$\pi\pi$	$(84.8^{+2.5}_{-1.3})\%$
$f_1(1285)$	$0^+(1^{++})$	1281.8 ± 0.6	$\pi^+\pi^-\eta$	$(52 \pm 16)\%$
$a_2(1320)$	$1^-(2^{++})$	1318.3 ± 0.6	$\pi^-\eta$	$(14.5 \pm 1.2)\%$
			$\pi^-\eta'(958)$	$(5.3 \pm 0.9)10^{-3}$
$f_0(1500)$ (?)	$0^+(0^{++})$	1507 ± 5	$\eta\eta$	$(5.1 \pm 0.9)\%$
$\pi_1(1600)$ (??)	$1^-(1^{-+})$	1596^{+25}_{-14}	$\pi^-\eta'(958)$	seen
$\pi_2(1670)$ (?)	$1^-(2^{-+})$	1672.4 ± 3.2	3π	$(95.8 \pm 1.4)\%$

Table 15: Summary of the observed and presumably observed mesons, including $I^G(J^{PC})$, mass [MeV], seen in (Decay Mode) and the branching ratio (Γ_i/Γ). The cases marked with a (?) and a (??) are assumptions.

The mesons, which are marked with a (?) and a (??) in table 15 are assumptions, only a partial-wave-analysis can identify the observed bumps with these known resonances.

Collectively, we can say that COMPASS is able to study final states with neutral mesons. The use of the kinematic fitter and the energy correction functions showed an improvement of the quality of the selected data.

To come back to the electromagnetic calorimeters, the here selected data can not only be used for physics analysis, but to study the performance of the hardware components of the experiment. The selected π^0 s were used for performance checks of the ECALs to show possible instabilities in the data reconstruction or problems with the hardware. The next section will show the results of this analysis.

8 Performance Checks of the Electromagnetic Calorimeters

The 2 γ of a decaying π^0 are detected in the two electromagnetic calorimeters ECAL1 and ECAL2. Neutral pions are reconstructed from neutral clusters in the calorimeters, as it was described above. The reconstruction shows a very nice and clear π^0 , which was already presented in the previous section. Since the signal is very significant and stable with less background, we could use the reconstructed π^0 to check the performance of our calorimeters. A time stability check on a run-by-run basis of the reconstruction of the invariant mass of the π^0 gives the possibility, to verify how good the electromagnetic calorimeters work. Excellent working calorimeters should guarantee a time stable π^0 mass, which not deviates from the PDG mass.

To verify whether the reconstruction is constant in time, the π^0 mass was investigated over a period of 2 weeks of data taking (2008 data). In the last section it has been explained in detail how the pion has been selected from $\pi^-p \rightarrow \pi^- \pi^0(\eta)p$, $\pi^-p \rightarrow \pi^- \pi^0 \pi^0(\eta\eta)p$ and $\pi^-p \rightarrow \pi^- \eta' p$. For the time stability check, the π^0 s from the channel $\pi^-p \rightarrow \pi^- \pi^0 p$ are taken, because there is no combinatorial background like in $\pi^-p \rightarrow \pi^- \pi^0 \pi^0 p$ and the signal is very clean.

For each run during the time period of 2 weeks, the π^0 invariant mass was selected and fitted with a gaussian and a 2nd order polynomial function for the background. Figure 77 shows the fitted π^0 mass for run 70452.

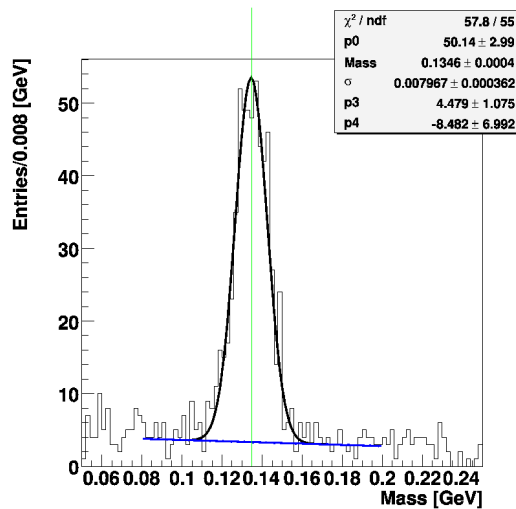


Figure 77: Fitting of the π^0 for run 70452 (2008 COMPASS data).

The red curve in fig. 78 shows the invariant mass of the π^0 (selected from $\pi^-p \rightarrow \pi^-\pi^0(\eta)p$) for every run of week 37 (2 weeks) without any energy corrections. The nominal PDG mass of the π^0 ($m_{\pi^0} = 134.9766 \pm 0.0006$ MeV) is marked with a green line.

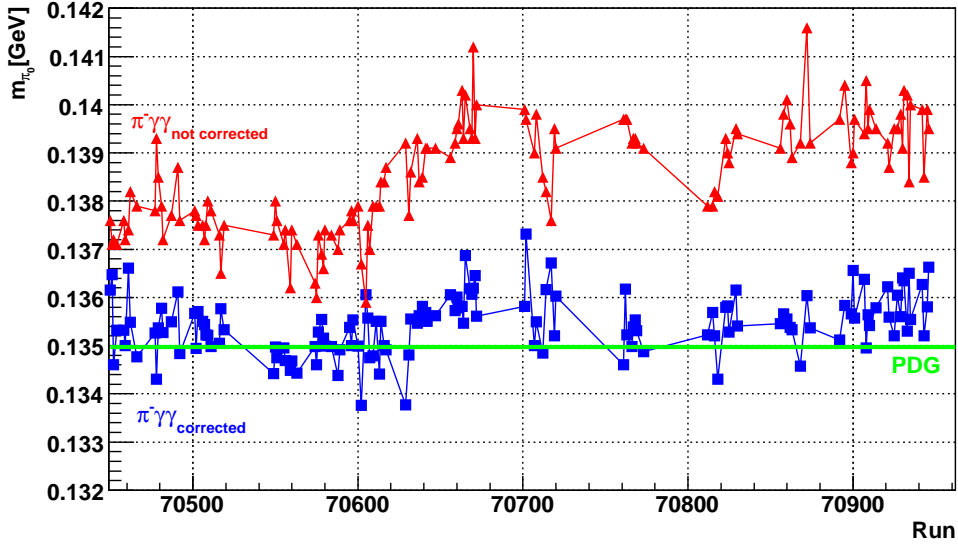


Figure 78: Fitted π^0 invariant mass from $\pi^-p \rightarrow \pi^-\pi^0p$ on a run-by-run basis of 2 weeks of data taking (2008 data). The red line shows the π^0 invariant mass without the energy correction (see text), while the blue line presents the fitted π^0 masses with the energy correction. The green line indicates the nominal PDG mass of the π^0 .

A mass shift of ~ 3 MeV to the nominal PDG mass of the π^0 is clearly visible, the fits give optima at ~ 138 MeV for the π^0 mass. Moreover, we can see a significant rise and an increase of the mass. The assigned values of the π^0 masses are about 3 MeV bigger than the PDG mass. From run-nr. 70605 on, an erratic jump is seen in the mass. It was first looked at whether differences of temperature or humidity in the experimental hall might cause these mass deviations. Namely, it must be considered that the COMPASS experiment is located above-ground and certainly an outer influence could cause effects in the hardware. Through moisture, an idle current can be produced in the photomultipliers. Actually we figured out, that it started raining at the time when we began with data taking for run-nr. 70605, where the rise occurs. One run is a data taking time of ~ 2 hours. Looking just at one day of data taking, it also shows day and night fluctuations (~ 4 runs in comparison). It is relatively unlikely that the temperature or humidity differences can be responsible, because a temperature or humidity change in the experimental hall can't happen so quickly. Based on such qualitative considerations, we can not say definitively that there is any correlation between the temperature or humidity change and the instability in the mass reconstruction of the π^0 .

Only it should be noted, that the selected π^0 from the final state $\pi^- p \rightarrow \pi^- \pi^0 \pi^0 p$ were also fitted and checked whether they show any time instabilities. We observed exactly the same fluctuations and an increase of the mass, therefore I conclude that the time instability is independent from different channels.

Additionally, we have seen, that the π^0 and η (selected from $\pi^- p \rightarrow \pi^- \pi^0(\eta) p$) invariant mass are dependent on the π^0 and η energy. This can be clearly seen in the following plots (fig. 79, 80 and 81, provided by I. Uman), where the π^0 mass was observed for a couple of runs in each ECAL1 module (GAMS, OLGA and MAINZ) in dependence of its energy. With increasing energy, the masses of the π^0 is getting higher for all modules. The fitted masses are all above the nominal PDG value.

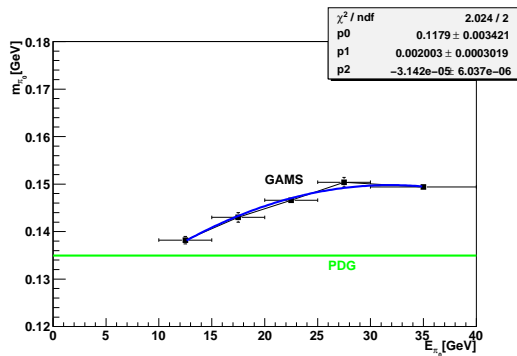


Figure 79: Measured $\pi^0 \rightarrow 2\gamma$ mass vs. $\pi^0 \rightarrow 2\gamma$ energy for GAMS ECAL1 cells [26].

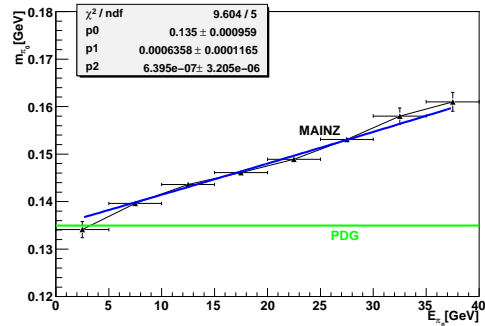


Figure 80: Measured $\pi^0 \rightarrow 2\gamma$ mass vs. $\pi^0 \rightarrow 2\gamma$ energy for MAINZ ECAL1 cells [26].

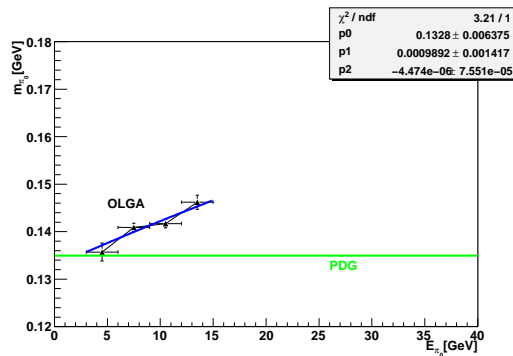


Figure 81: Measured $\pi^0 \rightarrow 2\gamma$ mass vs. $\pi^0 \rightarrow 2\gamma$ energy for OLGA ECAL1 cells [26].

For ECAL2 the η masses were also fitted for a couple of runs and plotted versus their energies. Fig. 82 shows the results. The reconstruction of the η is almost stable in time, but the values for the invariant mass (~ 553 MeV) lie above the PDG value ($m_\eta = 547.75 \pm 0.12$ MeV).

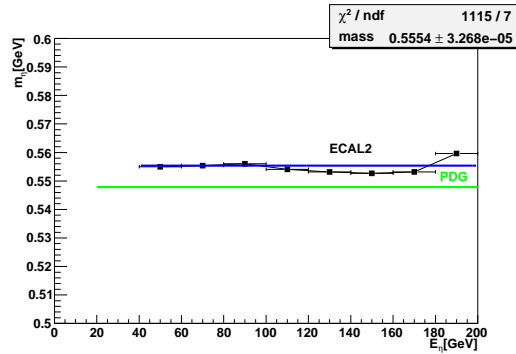


Figure 82: Measured $\eta \rightarrow 2\gamma$ mass vs. $\eta \rightarrow 2\gamma$ energy for ECAL2 cells [26].

There could be a few reasons, for causing these time instabilities. First of all, the hardware could be affected by aging problems or radiation damages. These effects could occur problems in the detection procedure. Secondly, for the electron beam calibration of the electromagnetic calorimeters (executed before the data taking period) we assume a defined energy for electrons. These assumed values do not needfully have to line with the actual values for the electron beam. Moreover, the shower profiles of electrons and photons look different and we expect more secondary showers for electrons. Therefore, it could have happened that the energy of the electrons was overestimated. Thus, it might be explain why we generally have a higher π^0 mass for every run (red line in fig. 78).

In general, we now need to proceed very strategically and have to implement a complete π^0 calibration on a run-by-run basis.

Because we are not yet having a complete π^0 calibration available, we introduced a temporary correction of the energies. This procedure was already explained in section 7. The effect of this correction procedure, which was implemented on a run-by-run basis (every run was corrected separately), can be nicely seen in fig. 78. The blue line in fig. 78 shows the corrected π^0 masses. We can see that the masses are now close to the PDG value. It shows, however, temporal fluctuations. These problems could probably be resolved with a π^0 calibration, which is planned to be implemented in 2010 reconstruction.

The next step will be to implement correction functions $f_{\text{ECAL}}(E_{\text{cluster}}, x, y, \text{run nr.})$ which take the x- and y-position of each cell into account. Then, we get the calibration constants on a cell by cell basis. The final goal is to perform the correction on a spill by spill basis $f_{\text{ECAL}}(E_{\text{cluster}}, x, y, \text{spill nr.})$.

9 Summary and Conclusion

In order to receive good physics results we need a good understanding of our experiment. The experiment provides the key for physics analysis and the more we understand it the more we can learn from it. Therefore, this diploma thesis deals with the technique and performance of the electromagnetic calorimeters as well as with the analysis of final states with neutral mesons in π^-p interactions for physical purposes.

Initially, the setup and operating mode of the two electromagnetic calorimeters of the COMPASS experiment were presented. In this context, the different calibration methods (e^- beam, laser/LED and π^0 calibration) were described. A brief overview of the existing ECAL1 laser calibration system was given. The main focus was on first test measurements for a new laser calibration system for ECAL2. In this regard, the two module types of ECAL2 were used for tests to clarify if a laser calibration system could be used for this electromagnetic calorimeter.

In the first instance, the light coupling into the different module types plays a major role. GAMS are pure lead glass modules and produce Cherenkov light which is directly detected by the photomultipliers. The inner part of ECAL2 is equipped with SHASHLIK modules, which consist of alternating scintillator and lead layers. For light guidance inside the module WLS fibers are installed. The measurements have shown, that it is not possible to use LED light for SHASHLIK modules, because the intensity is much too low (a factor of 10^3 too low). However, it could be shown that it is possible to couple sufficient light into the module by using laser light. In this context, the light coupling (distance and angular dependency) and different laser intensities have been tested. The comparison among these two module types has shown, that one gets a factor of 10^2 less light into a SHASHLIK module. The test measurements have shown, that it is nonetheless possible to implement a laser calibration system for ECAL2. The implementation of the laser monitoring system for ECAL2 is planned for 2011.

The software part of this diploma thesis deals with the analysis of final states in π^-p interactions at COMPASS. The thesis presents first results of the analysis on final states with neutral mesons (π^0 , η and η'). The reactions $\pi^-p \rightarrow \pi^-\pi^0p$, $\pi^-p \rightarrow \pi^-\eta p$, $\pi^-p \rightarrow \pi^-\pi^0\pi^0p$, $\pi^-p \rightarrow \pi^-\eta\eta p$ and $\pi^-p \rightarrow \pi^-\pi^+\pi^-\gamma\gamma$ with an incoming π^- beam of 190 GeV were studied. The analysis was performed on a part of 2008 data ($\sim 14\%$). For the analysis $\sim 10^9$ events were processed. The event selection (trigger, beam properties, cluster selection in the electromagnetic calorimeters and tracking) was explained in detail with the goal to select favoured events and minimize background events by applying cuts. Additionally, a kinematic fitting routine was implemented to improve the data selection. The fitting was done on the π^0 and η invariant mass and it could be shown, that the width of the peaks of $\eta \rightarrow \pi^+\pi^-\pi^0$ and $\eta' \rightarrow \pi^+\pi^-\eta$ is reduced by using the kinematic fitter, the signal got much cleaner and we obtained a better resolution. Furthermore, an additional correction of the cluster energies was implemented, which improved the data selection. The statistics and invariant mass plots were presented. The plots show extremely nice and clear peaks of various diffractively produced states, i.e. $\rho(770)$, $a_0(980)$, $a_2(1320)$, $\pi_2(1670)$

and $\rho_2(1700)$. A first evidence for the known $f_0(1500)$ is seen in the $\pi^-p \rightarrow \pi^- \eta \eta p$ channel at 1.5 GeV. This analysis confirms that COMPASS is able to study final states with neutral mesons.

Additionally, the thesis presents first results of the analysis of the reaction $\pi^-p \rightarrow \pi^- \pi^+ \pi^- \gamma \gamma p$. The $\eta(547)$ and $\omega(782)$ states in the 3 body system $\pi^- \pi^+ \gamma \gamma (= \pi^0)$ are well seen. The η' and f_1 (in the 3 body system $\pi^- \pi^+ \gamma \gamma (= \eta)$) are seen as very sharp needles, centered at the PDG mass. A first hint of the existence of the exotic state $\pi_1(1600)$ is seen at an energy of 1.6 GeV in the COMPASS data, which was already observed in the E852 and VES experiment. Further analysis will clarify if this is really the exotic state.

Coming back to the hardware, the invariant mass of the π^0 s from the final state $\pi^-p \rightarrow \pi^- \pi^0 p$ were used for performance checks of the electromagnetic calorimeters ECAL1 and ECAL2. The check was done on 2 weeks of data taking on a run-by-run basis (2008 data). The π^0 s were fitted with a gaussian and second order polynomial functions to get the exact value of the invariant mass. These masses were determined as a function of the run number (~ 2 hours of data taking). It could be shown that time instabilities occur, which can be explained by possible hardware reasons and wrong energy estimations during the electron beam calibration.

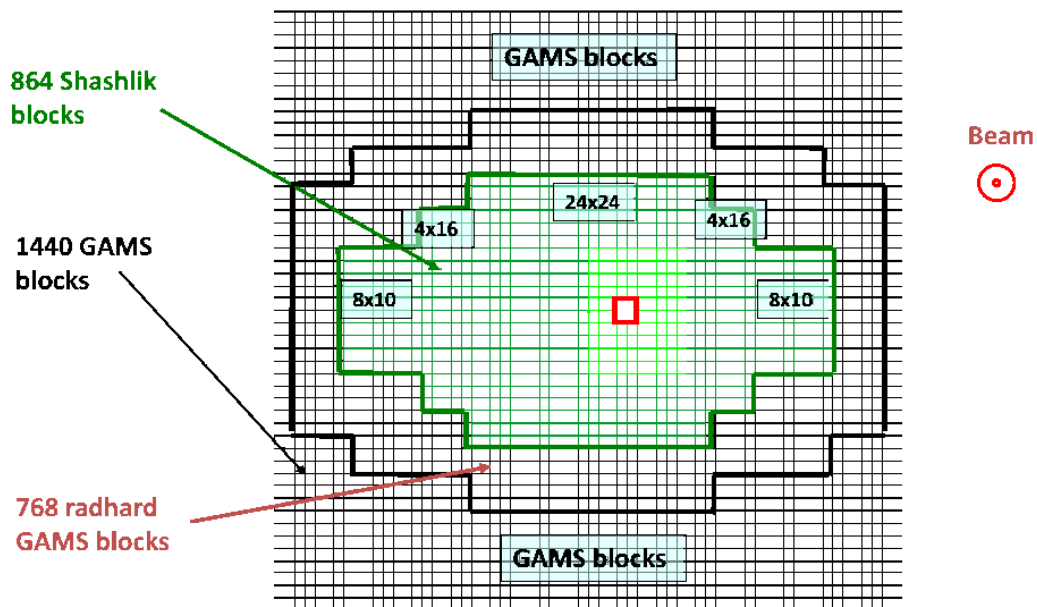
A preliminary calibration correction (photon energy correction function) $f_{\text{ECAL}}(E_{\text{cluster}}, \text{cell types})$ was implemented to improve the selection. It could be shown that it is effective. $f_{\text{ECAL}}(E_{\text{cluster}}, \text{cell types})$ was used on a run-by-run basis and it could be demonstrated that the corrections $f_{\text{ECAL}}(E_{\text{cluster}}, \text{cell type}, \text{run nr.})$ improve the data selection.

Appendix

A ECAL2 Counters Map Type (Run 2008)

(Figure provided by V. Polyakov of the COMPASS Collaboration)

ECAL2, Run 2008, 64x48 GAMS type blocks, 2x2 blocks central hole; Lead glass block: size - 38.2x38.2mm², length - 450mm; TF101 glass - radhard block; TF1 - non radhard block; Shashlik block - 155 layers (1 layer - 0.8mm lead + 1.5mm scintillator + 0.2mm paper); size - 38.2x38.2mm²



B Data Sheet of the Minilite Laser I and II

(Data sheet provided by R. Geyer of the COMPASS Collaboration)

Continuum[®]
An Excel Technology Company

Minilite™ The Entry Level Nd:YAG Laser System



MINILITE™ FEATURES & BENEFITS

Can be operated locally or remotely via TTL interface

No need for an external water hook-up, the system is completely self-contained

Easy flashlamp replacement without alignment of the laser oscillator

Invar resonator structure ensures long-term thermal and mechanical stability

Variable attenuator included

FLASHLAMP PUMPED Nd:YAG

MINILITE™ SPECIFICATIONS	DESCRIPTION	MINILITE™ I	MINILITE™ II
	Repetition Rate (Hz)		1-15
Energy (mJ)			
1064 nm		28	50
532 nm		12	25
355 nm		4	8
266 nm		2	4
Pulsewidth ¹ (nsec)			
1064 nm		5-7	5-7
532 nm		3-5	3-5
355 nm		3-5	3-5
266 nm		3-5	3-5
Linewidth (cm ⁻¹)		1	1
Divergence ² (mrad)		< 3	< 3
Rod Diameter (mm)		3	3
Jitter ³ (sns)		0.5	0.5
Energy Stability ⁴ (±%)			
1064 nm		2; 0.6	2; 0.6
532 nm		3; 1.0	3; 1.0
355 nm		4; 1.3	4; 1.3
266 nm		8; 2.6	8; 2.6
Polarization			
1064 nm		HORIZONTAL	HORIZONTAL
532 nm		VERTICAL	VERTICAL
355 nm		HORIZONTAL	HORIZONTAL
266 nm		HORIZONTAL	HORIZONTAL

Minilite™ - Continuum's entry level Q-switched Nd:YAG laser system

The Minilite™ series of pulsed Q-switched laser systems provides high levels of performance while maintaining a very reasonable price point. The Minilite™ is designed for new and existing users of pulsed lasers allowing easy operation, simple external control and compact size. Minilites are used for remote sensing, sample testing, mass spectroscopy, LIF and laser flash photolysis.

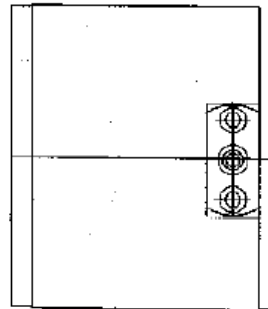
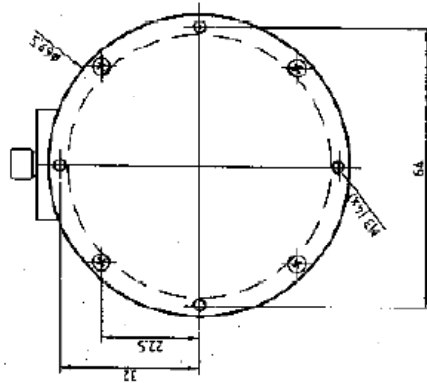
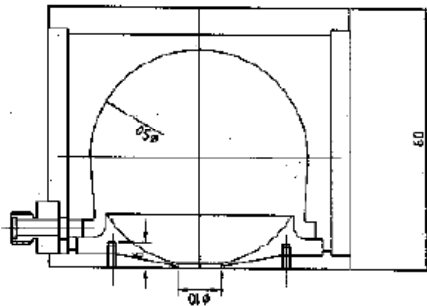
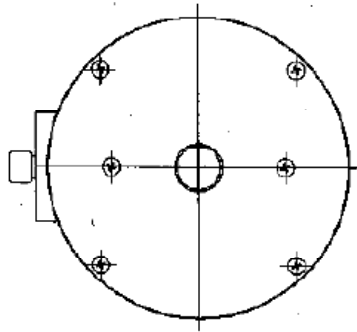
NOTES

1. Full width half max
2. Full angle for 86% (1/e²) of energy
3. With respect to external trigger
4. The first value represents shot-to-shot for 99.9% of pulses, the second value represents RMS.

All specifications at 1064 nm unless otherwise noted. As a part of our continuous improvement program, all specifications are subject to change without notice.

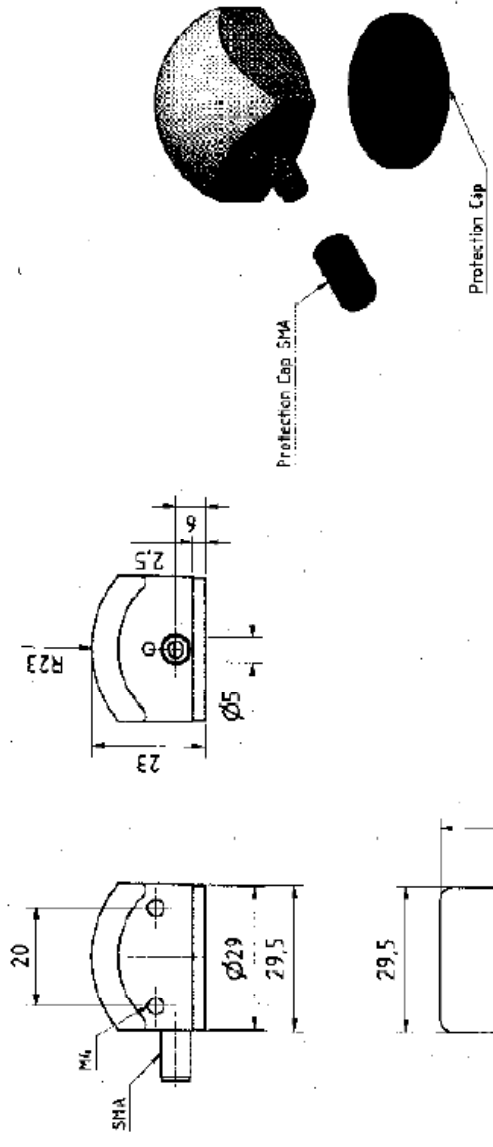
C Data Sheets of the Integrating Spheres

Data Sheet of Integrating Sphere 1 (big Ulbricht Sphere)



UPK-50-L-SHA
29.01.2003

Data Sheet of Integrating Sphere 2 (small Ulbricht Sphere)



		tolerance	material	rough sizes	surface
ISO-2768-mK					
	name	date			
	K	2013/06			
UPK-12.5-L-SMA					
Untertyp: 6-Strahlentrommel, Durchmesser: 29,5 mm, SMA-Bohrung			scale	1:1	AL
					page 1/1

D ECAL1 High Voltages for GAMS Modules (2009 run)

For the test measurements the same ECAL1 high voltage values were preset. The following table is an excerpt of the laser calibration settings/results for GAMS modules in ECAL1 (2009 run). The last column ("HvRf") is the reference in channels. The true HV is the channel value, multiplied by 2. So these values are around 1200-1500 Volts (the same like in the test measurements).

D	x	y	ADC	Ped	Led	RMS	Ref	Time	Factor	Elcal	Hvcl	HvRf
G	0	00-0-00	128.5	83	6	168	205.5	-2.01	220.1	656	600	
G	0	10-0-04	132.3	244	6.8	268	205.6	-1.1	231.6	722	713	
G	0	20-0-08	124.6	149	6.6	159	208.9	-1.07	244.2	759	745	
G	0	30-0-12	107.8	144	6.7	188	207.1	-1.31	327.4	695	656	
G	0	40-0-16	104.9	179	6.8	222	210	-1.24	236.9	768	756	
G	0	50-0-20	130.5	140	6.6	154	221.2	-1.1	233.7	656	647	
G	0	60-0-24	105.6	197	6.6	208	219.6	-1.06	288.1	708	682	
G	0	70-0-28	128.1	212	6.3	223	216.2	-1.05	222	648	643	
G	0	80-1-00	99.8	70	6.6	229	223.5	-3.28	442.8	781	600	
G	0	90-1-04	88	148	6.4	163	224.3	-1.1	339.4	724	680	
G	0	100-1-08	89.4	219	6.7	237	233	-1.08	211.9	677	677	
G	0	110-1-12	93.4	181	6.1	223	224.3	-1.23	275.5	649	624	
G	0	120-1-16	83.7	236	6.3	244	225.8	-1.03	232.3	688	680	
G	0	130-1-20	75.4	260	6.4	266	228.8	-1.02	244	624	614	
G	0	140-1-24	74.2	84	7.1	103	221.4	-1.22	222.5	784	779	
G	0	150-1-28	81.6	204	6.3	214	225.6	-1.05	236.9	695	685	
G	0	160-2-00	64.1	130	6.3	179	218	-1.38	299	738	706	
G	0	170-2-04	76.5	294	6.5	316	231.8	-1.08	212.8	670	670	
G	0	180-2-08	67	200	6.6	215	228.3	-1.08	234.7	698	687	
G	0	190-2-12	70.2	189	6.6	205	228.5	-1.08	223.4	688	682	
G	0	200-2-16	89.7	158	6	182	216.4	-1.15	267.3	711	690	
G	0	210-2-20	90.2	211	6.1	213	215.1	-1.01	243	797	783	
G	0	220-2-24	66.6	179	6.6	230	215.3	-1.28	335.1	745	706	
G	0	230-2-28	67.8	200	6.9	216	213.6	-1.08	211.3	763	763	
G	1	00-0-01	125.1	229	6.1	240	206.7	-1.05	236.2	631	621	
G	1	10-0-05	112.1	193	6.2	208	209.3	-1.07	271.2	660	637	
G	1	20-0-09	120.9	133	6.7	136	213.7	-1.02	254.1	687	671	
G	1	30-0-13	113	196	6.3	202	203.6	-1.03	269.5	739	718	
G	1	40-0-17	120	145	6.4	162	213.6	-1.11	277.6	726	703	
G	1	50-0-21	117.9	130	6.5	133	212.9	-1.02	261.5	719	702	
G	1	60-0-25	108.5	193	6.2	189	223.5	1.02	312.5	631	600	
G	1	70-0-29	117.1	185	6.7	207	220.8	-1.12	241.3	643	632	
G	1	80-1-01	84.2	106	6.6	109	229.6	-1.03	541.1	722	627	
G	1	90-1-05	81.9	231	6.4	246	226.5	-1.07	187.5	673	683	
G	1	100-1-09	103.6	351	6.7	345	218.5	1.02	344.9	838	789	
G	1	110-1-13	76.9	198	6.3	214	226.2	-1.08	274.8	754	729	
G	1	120-1-17	84	154	6.3	163	223.6	-1.05	278.6	700	675	
G	1	130-1-21	75.4	259	6.6	270	226.3	-1.04	261.3	778	761	
G	1	140-1-25	72.6	170	6.7	182	228.4	-1.07	282.7	679	653	
G	1	150-1-29	81.2	227	6.4	229	227.3	-1.01	559.1	724	630	
G	1	160-2-01	82.5	207	6.3	215	225.4	-1.04	308	659	628	
G	1	170-2-05	82.9	154	6.7	159	228.9	-1.03	287	739	706	
G	1	180-2-09	71.7	231	6.6	234	232.6	-1.02	279.1	669	645	
G	1	190-2-13	77	200	6.5	210	225.1	-1.05	265.7	715	692	
G	1	200-2-17	70.6	215	6.2	221	216.3	-1.03	257.7	735	716	
G	1	210-2-21	73.8	154	6.9	178	214.8	-1.16	326.3	727	689	
G	1	220-2-25	73.2	227	6.2	247	217.9	-1.09	264.4	725	705	
G	1	230-2-29	69.1	166	6.3	195	219.7	-1.18	250.2	629	613	
G	2	00-0-02	107.1	160	6.6	186	204.9	-1.16	310.4	728	692	
G	2	10-0-06	105.7	144	6.3	160	209.6	-1.11	256.4	658	641	

References

- [1] CERN (2008), "**The standard package**", Cern Article, Retrieved December 21, 2009 from: <http://public.web.cern.ch/public/en/Science/StandardModel-en.html>
- [2] Wikipedia (2010, February 7), "**Standard Model**", Wikipedia, Retrieved February 8, 2010 from: <http://en.wikipedia.org/wiki/StandardModel>
- [3] Guy Coughlan, James Dodd, "**Elementarteilchen: Eine Einführung für Naturwissenschaftler**", Braunschweig/Wiesbaden 1996 (Vieweg und Sohn Verlagsgesellschaft mbH)
- [4] Erich Lohrmann, "**Einführung in die Elementarteilchenphysik**", Stuttgart 1983 (Teubner Verlag)
- [5] Gary Adams for the E852 Collaboration, "**Experimental Evidence for Hadronproduction of Exotic Mesons**", International Conference on Quark Nuclear Physics, Adelaide (February 2000)
- [6] VES Collaboration, "**Study of π^-N and $\pi^-N \rightarrow \pi^- \eta' N$ reactions at $37 \frac{\text{GeV}}{c}$** ", Phys. Lett. B313(1993)276-282//IFVE-93-62
- [7] CERN (2007, December 25), "**World's Largest Silicon Tracking Detector Installed At CERN**", Science Daily Article, Retrieved December 15, 2009 from: <http://www.sciencedaily.com/releases/2007/12/071218115622.html>
- [8] CERN, "**COMPASS: Common Muon Proton Apparatus for Structure and Spectroscopy**", Retrieved December 2009 from: <http://wwwcompass.cern.ch/>
- [9] CERN, "**COMPASS OFFLINE**", Retrieved January 12, 2010 from: <http://wwwcompass.cern.ch/compass/software/offline/welcome.html#software>
- [10] CERN, "**PHysics Analysis Software Tools**", Retrieved January 12, 2010 from: <http://ges.home.cern.ch/ges/phast/index.html>
- [11] Stefanie Grabmüller, "**Studies of Diffractive Particle Production at COMPASS**", Garching 2005 (Diploma Thesis)
- [12] Domagoj-Marko Cotic, "**Determination of the linearity and energy resolution of lead glass modules in the electromagnetic calorimeter at the COMPASS experiment**", Mainz 2008 (Diploma Thesis)
- [13] Wikimedia (2008, April 11), "**Calorimeters for High-Energy Physics Part 2**", Wikimedia, Retrieved March 22, 2010 from: <http://upload.wikimedia.org/wikipedia/commons/thumb/6/6b/Cherenkov.svg/378px-Cherenkov.svg.png>

- [14] Boris Grube, "**A trigger control system for COMPASS and a measurement of the transverse polarization of Λ and Ξ hyperons from quasi-real photo-production**", Munich 2006 (PhD Thesis)
- [15] Christian Wuttke, "**Conceptional design of a multiplicity counter for the COMPASS experiment**", Mainz 2007 (Diploma Thesis)
- [16] V. Kolosov, O. Kouznetsov, A. Magnon, F. Nerling, "**Present performances of COMPASS electromagnetic calorimetry from data analysis**", Cern 2008 (COMPASS Note 2008-5)
- [17] CERN-PH-EP (2007, January 17), "**The COMPASS Experiment at CERN**", January 30, 2007
- [18] S. Eidelman, et al., "**Particle Physics Booklet**", Extracted from the Review of Particle Physics, 2004 (Teubner Verlag)
- [19] Martin Faessler, "**Hadron Spectroscopy at COMPASS**", APS Topical Group in Hadron Physics: April 29 - May 01 2009, Denver 12.08.2009
- [20] Kay Huettmann, "**Untersuchung der $\eta\pi$ -P-Welle in der Antiproton-Neutron-Annihilation in $\pi^-\pi^0\eta$** ", Garching 1997 (Diploma Thesis)
- [21] HD-THEP-03-63, O. Nachtmann, "**Pomeron Physics and QCD**", Contribution to the Ringberg Workshop on HERA physics 2003, Heidelberg 2003
- [22] C. Grupen, "**Teilchendetektoren**", BI-Wissenschaftsverlag, 1983
- [23] A. Lednev, "**Status of ECAL2**", Hadron-Meeting, 12.08.2009
- [24] Saclay Group, "**ECAL1 Monitoring - Laser Safety Manual**, 2009, provided by Stephane Platchkov
- [25] RP Photonics, "**Encyclopedia of Laser Physics and Technology**", Retrieved February 14, 2010 from: <http://www.rp-photonics.com/integratingspheres.html>
- [26] I. Uman, S.C. Dinter, E. Romero Adam for the Hadron Analysis Group: "**Study of diffractively and centrally produced resonances in $\pi^-p \rightarrow \pi^-\pi^0(\eta)p$ and $\pi^-p \rightarrow \pi^-\pi^0\pi^0(\eta\eta)p$** ", CERN, 2009
- [27] COMPASS internal Wikipedia page (COMPASS collaboration), "**Compass Trigger and Trigger Control System**", Retrieved February 12, 2010 from: <http://lxfsrcb6103.cern.ch/twiki/bin/view/Trigger/WebHome>
- [28] Quirin Weitzel, "**Precision Meson Spectroscopy: Diffractive Production at COMPASS and Development of a GEM-based TPC for PANDA**", September, 2008 (Dissertation)
- [29] Root (2009, December 11), "**Root: User's Guide v5.26**"

-
- [30] R.K. Bock and A. Vasilescu, "**The Particle Detector BriefBook**", (Springer Verlag)
- [31] T. Schlüter, "**A Code For Kinematic Fitting with Constraints from intermediate Particle Masses**", Memorandum (Compass Note 2007-10), September, 2007

List of Figures

1	The Standard Model of elementary particles	3
2	π^+, π^- decay [3].	5
3	π^0 decay and pair production [3].	5
4	Meson nonet: Pseudoscalar mesons with spin $S=0$	7
5	Meson nonet: Vector mesons with spin $S=1$	7
6	(a.): The $\pi^+\pi^-\eta$ effective mass distribution. (b.): $\pi_1(1600) \rightarrow \pi^-\eta'$ seen by E852 (2001) in $\pi^-p \rightarrow \pi^-\eta'p$ at 1600 MeV [5].	9
7	$a_2(1320), \pi_1(1600)$ seen in $\pi^-N \rightarrow \pi^-\eta'N$ at $37 \frac{GeV}{c}$ by VES [6].	9
8	Single diffractive excitation.	10
9	Central production mechanism.	11
10	Location of the COMPASS experiment at CERN.	13
11	The M2 Beam Line for the Muon Programme [14].	14
12	The COMPASS Layout [19].	15
13	CEDAR's for pion and kaon tagging.	16
14	Front view of the RPD detector.	16
15	Artistic view of the 60 m long COMPASS two-stage spectrometer [19].	18
16	Energy loss mechanism of electrons in lead as a function of the electron energy [12].	22
17	Cross section of photons in lead as a function of the photon energy. $\sigma_{p.e.}$ defines the cross sections of the photoelectric effect etc. [12].	22
18	Electromagnetic Shower [12].	23
19	Cherenkov Effect [13].	25
20	Structure of ECAL1, made of GAMS, OLGA and MAINZ Modules [12].	27
21	Structure of ECAL2, made of GAMS and SHASHLIK Modules (inner dark grey part).	27
22	Different lead glass types for ECAL1 and ECAL2: upper and lower module. The central one is a SHASHLIK module [19].	28

23	Schematic view of a lead-glass module (GAMS, OLGA, MAINZ) with a lead glass barrel (1) where a photomultiplier (2) is attached, a screening at the top (3) and a fiber plug-in (4) [12].	28
24	Schematic view of a SHASHLIK module.	30
25	Schematic view of a common photomultiplier tube.	31
26	Calibration procedure by using an electron beam (blue marked cell: is currently calibrated); red line = sequence of calibration.	32
27	ECAL1 calibration system: schematic view [24].	36
28	Setup for photomultiplier tests with a LED.	38
29	Oscilloscope view of the electron signal with ΔU = measured voltage drop (signal rate). [voltage base = 50 mV per div, time base = 20 ns per div].	39
30	Experimental setup for LED test measurements with a GAMS module.	40
31	Gain curve of the voltage measurement for a GAMS Module with LED light.	40
32	Experimental setup for test measurements with a GAMS module, using a laser.	41
33	Inside view of the dark box for laser test measurements.	41
34	Schematic view of an integrating sphere [25].	42
35	Two integrating spheres, installed in their protection mount (LMU test spheres).	43
36	Comparison of the laser and LED gain curve (GAMS module).	44
37	Comparison of the PM gain curves (SHASHLIK and GAMS).	45
38	Distance of the fiber mount and the SHASHLIK module.	46
39	Measured voltages ΔU [mV].	46
40	Selected event topology for the reaction $\pi^- p \rightarrow \pi^- \pi^0(\eta) p$ for data selection plus the numbers which refer to the given explanations in the text.	53
41	Number of hits in CEDAR 2 versus CEDAR 1 for pions (lower left corner) and kaons (upper right corner).	55
42	Number of hits in CEDAR 2 versus CEDAR 1 for pions (after cut).	55
43	The primary vertex distribution along the z-axes for $\pi^- p \rightarrow \pi^- p + \text{neutrals}$. The primary vertex is chosen to be within the yellow shaded area.	56
44	The primary vertex distribution along xy-axes for $\pi^- p \rightarrow \pi^- p + \text{neutrals}$. The primary vertex is chosen to be at a well defined distances ($r_{\text{vertex}} < 1.5\text{cm}$) from the beam (yellow shaded area). The visual contrast of the shown picture could deceive here.	56

45	Azimuthal angle of the recoiling proton (track) in the RPD detector vs. the azimuthal angle of the $\pi^-4\gamma$ system.	57
46	Ratio of energy deposits in cell with maximum energy with the cluster energy of GAMS (ECAL1) and MAINZ cells. Noisy channels are excluded demanding $\frac{E_{\text{cell}_{\text{max}}}}{E_{\text{cluster}}} < 0.92$ (yellow shaded area).	57
47	The time difference of the beam with the clusters are extract to be in the range of $t_{\text{low}} = -3\text{ns}$ and $t_{\text{high}} = 5\text{ns}$. Clusters fulfilling this exigence are selected.	58
48	Confidence level for the reaction $\pi^-p \rightarrow \pi^-\pi^+\pi^-\gamma\gamma p$ with a π^0 hypothesis (constraint).	61
49	Confidence level for the reaction $\pi^-p \rightarrow \pi^-\pi^+\pi^-\gamma\gamma p$ with an η hypothesis (constraint).	61
50	Pulls π^0 (from: $\pi^-p \rightarrow \pi^-\pi^+\pi^-\gamma\gamma p$): The images in the top row show the horizontal direction component of the upper and lower photons; The images in the middle present the pull distribution of the vertical direction of the upper and lower photon; The images in the third row show the pulls of the energy.	63
51	Pulls η (from $\pi^-p \rightarrow \pi^-\pi^+\pi^-\gamma\gamma p$): The images in the top row show the horizontal direction component of the upper and lower photons; The images in the middle present the pull distribution of the vertical direction of the upper and lower photon; The images in the third row show the pulls of the energy.	64
52	Invariant mass of the 3 body system $\pi^+\pi^-\gamma\gamma(\pi^0)$ before (red shaded area) and after (yellow shaded area) the kinematic fit.	65
53	Invariant mass of the 3 body system $\pi^+\pi^-\gamma\gamma(\eta)$ before (red shaded area) and after (yellow shaded area) the kinematic fit.	65
54	Invariant $\gamma\gamma$ mass around the π^0 mass from $\pi^-p \rightarrow \pi^-\gamma\gamma p$	66
55	Invariant $\gamma\gamma$ mass around the η masss from $\pi^-p \rightarrow \pi^-\gamma\gamma p$	66
56	Invariant mass of the $\pi^-\pi^0$ system in the $\pi^-p \rightarrow \pi^-2\gamma p$ channel. The position of the $\rho(770)$ is indicated.	67
57	Invariant mass of the $\pi^-\eta$ system in the $\pi^-p \rightarrow \pi^-2\gamma p$ channel. The position of the $a_2(1320)$ is indicated.	67
58	2 dimensional invariant mass plot of the $\gamma\gamma$ mass versus the $\gamma\gamma$ mass from $\pi^-p \rightarrow \pi^-4\gamma p$	69
59	3 dimensional lego plot of the $\pi^0\pi^0$ signal from $\pi^-p \rightarrow \pi^-4\gamma p$	69
60	2 dimensional invariant mass plot of the $\gamma\gamma$ mass versus the $\gamma\gamma$ mass from $\pi^-p \rightarrow \pi^-4\gamma p$	69
61	3 dimensional lego plot of the $\eta\eta$ signal from $\pi^-p \rightarrow \pi^-4\gamma p$	69

62	The 2 invariant mass plot (fitted) for the 3 possible $\gamma\gamma$ combinations (76 runs) around the π^0 mass in the reaction $\pi^-p \rightarrow \pi^-4\gamma p$	70
63	The 2 invariant mass plot (fitted) for the 3 possible $\gamma\gamma$ combinations (76 runs) around the η mass in the reaction $\pi^-p \rightarrow \pi^-4\gamma p$	70
64	Invariant mass of the $\pi^-\pi^0$ system (in $\pi^-p \rightarrow \pi^-\pi^0\pi^0p$). The position of the $\rho(770)$ is indicated.	71
65	Invariant mass of the $\pi^-\eta$ system (in $\pi^-p \rightarrow \pi^-\eta\eta p$). The positions of the $a_0(980)$ and $a_2(1320)$ are indicated.	71
66	Invariant mass plot of the $\pi^0\pi^0$ system with an indicated $f_2(1270)$. At 0.5 GeV a red line is indicated, which could be due to a kaon.	71
67	Invariant mass plot of the $\pi^-\pi^0\pi^0$ system with an indicated $a_2(1320)$ at 1.3 GeV and the $\pi_2(1670)$ at 1.7 GeV.	71
68	Invariant mass of the $\eta\eta$ system. The position of the possible $f_0(1500)$ is indicated.	72
69	Invariant mass of the $\pi^-\eta\eta$ system. The position of the $\pi(1800)$ is indicated. . .	72
70	Invariant $\gamma\gamma$ mass around the π^0 mass from the reaction $\pi^-p \rightarrow \pi^-\pi^+\pi^-2\gamma p$	73
71	Invariant $\gamma\gamma$ mass around the η mass from the reaction $\pi^-p \rightarrow \pi^-\pi^+\pi^-2\gamma p$	73
72	Invariant mass of $\pi^-\pi^+\gamma\gamma$ versus the $\gamma\gamma$ invariant mass.	74
73	Invariant mass plot of the 3 body system $\pi^-\pi^+\gamma\gamma(=\pi^0)$	75
74	Invariant mass plot of the 3 body system $\pi^-\pi^+\gamma\gamma(=\eta)$	75
75	Invariant mass plot of the 4 body system $\pi^-\pi^-\pi^+\gamma\gamma(\pi^0)$ with 3 body = η	76
76	Invariant mass plot of the 4 body system $\pi^-\pi^-\pi^+\gamma\gamma(\eta)$ with 3 body = η' (6903 events).	76
77	Fitting of the π^0 for run 70452 (2008 COMPASS data).	79
78	Fitted π^0 invariant mass from $\pi^-p \rightarrow \pi^-\pi^0p$ on a run-by-run basis of 2 weeks of data taking (2008 data). The red line shows the π^0 invariant mass without the energy correction (see text), while the blue line presents the fitted π^0 masses with the energy correction. The green line indicates the nominal PDG mass of the π^0 .	80
79	Measured $\pi^0 \rightarrow 2\gamma$ mass vs. $\pi^0 \rightarrow 2\gamma$ energy for GAMS ECAL1 cells [26].	81
80	Measured $\pi^0 \rightarrow 2\gamma$ mass vs. $\pi^0 \rightarrow 2\gamma$ energy for MAINZ ECAL1 cells [26].	81
81	Measured $\pi^0 \rightarrow 2\gamma$ mass vs. $\pi^0 \rightarrow 2\gamma$ energy for OLGA ECAL1 cells [26].	81
82	Measured $\eta \rightarrow 2\gamma$ mass vs. $\eta \rightarrow 2\gamma$ energy for ECAL2 cells [26].	82

List of Tables

1	Types of mesons and quantum numbers for the lowest lying states.	6
2	Pseudoscalar mesons from u/d- and s-quarks and their properties [4].	7
3	Properties of the various lead glass modules [12].	29
4	Parameters of the SHASHLIK modules.	30
5	Characteristics of laser-1 and laser-2 for the ECAL1 calibration: nominal and operational values (as used in the COMPASS experiment) [24].	37
6	Measured voltage ΔU [mV] for the PM with an attached GAMS module with LED light, in dependence of the high voltage HV [V].	40
7	Measured voltage ΔU [mV] for a GAMS module with a laser, in dependence of the high voltage HV [V].	43
8	Measured voltage ΔU [mV] with laser light (SHASHLIK module), in dependence of the high voltage HV [V].	44
9	Measured voltages ΔU [mV] in dependence of the applied high voltage (SHASHLIK module).	45
10	Measured voltage with the laser intensity from the ECAL1 adjustment and measured voltage with a higher laser intensity at two different HV settings.	47
11	Measured voltage ΔU for different SHASHLIK modules, at the same high voltage $U(\text{HV}) = 1750 \text{ V}$	47
12	Statistics for $\pi^- p \rightarrow \pi^- 2\gamma p$ (≈ 70 runs of W37 2008 data).	66
13	Statistics for $\pi^- p \rightarrow \pi^- 4\gamma p$ (76 runs of W37 2008 data).	68
14	Statistics for $\pi^- p \rightarrow \pi^- \pi^+ \pi^- 2\gamma p$ (76 runs of W37 2008 data).	73
15	Summary of the observed and presumably observed mesons, including $I^G(J^{PC})$, mass [MeV], seen in (Decay Mode) and the branching ratio (Γ_i/Γ). The cases marked with a (?) and a (??) are assumptions.	77

ACKNOWLEDGEMENT - DANKSAGUNG

An dieser Stelle möchte ich mich bei allen Personen bedanken, die mich bei der Erstellung dieser Arbeit unterstützt haben.

Mein besonderer Dank gilt Herrn Prof. Martin Faessler, der es mir ermöglicht hat meine Diplomarbeit in seiner Arbeitsgruppe anzufertigen und der mit viel Engagement, guten Ideen und Einsatz meine Diplomarbeit betreut hat. Ganz herzlich möchte ich mich für die Ermöglichung zahlreicher CERN Aufenthalte bedanken, die mir einen Einblick in das Experiment gaben und eigene Messungen erlaubten.

Deepest gratitude goes to Dr. Ismail Uman, who supervised my analysis work at CERN. Thanks for the helpful teaching lessons in programming and interesting physics discussions. Special thanks for all the support at CERN (taxi services etc.).

Ebenfalls bedanken möchte ich mich bei Herrn Prof. Wolfgang Dünneweber, für die interessanten Gespräche über Physik, Literatur und das Weltgeschehen. Diese waren hervorragende Hilfestellungen und Inspirationen für meine Diplomarbeit.

Recht herzlich bedanken möchte ich mich bei allen Mitarbeitern der Arbeitsgruppe, die mich während der gesamten Zeit unterstützt haben, besonders Jean-Francois Rajotte, Massimo Bettinelli, Tobias Schlüter, Hauke Wöhrmann und Meike Dlaboha, die mir immer mit Rat und Tat zur Seite standen und zum Gelingen dieser Diplomarbeit beigetragen haben.

Special thanks to Dr. Stephan Platchkov and Dr. Reiner Geyer for helping me with the hardware work at CERN. I also would like to thank Alexander Zvyagin for the computer support. Many thanks to the COMPASS collaboration for giving me the possibility to present my work at CERN.

Unendlicher Dank gebührt meinen Eltern, Christine und Matthias Dinter, die mich während meines Studiums zu jeder Stunde moralisch und finanziell unterstützt haben. Ohne Ihre Hilfe wäre ich nie so weit gekommen.

Mein grosser Dank gilt meinem Freund Toni, der mich während des letzten Jahres immer wieder motivieren konnte, stets ein offenes Ohr für mich hatte und immer an meiner Seite war. Danke für deine Liebe!

Erklärung

Ich erkläre hiermit, dass ich die vorliegende Diplomarbeit selbständig und nur unter Verwendung der angegebenen Literatur und Hilfsmittel angefertigt habe.

Ort und Datum:

.....
(Unterschrift der Studentin)